REPORT DOCUMENTATION PAGE

Form Approved
OMB No. 0704-0188

PLEASE DO NOT RETURN YOUR FORM TO THE ABOVE ADDRESS.

1. REPORT DATE *(DD-MM-YYYY)*	2. REPORT TYPE	3. DATES COVERED *(From - To)*
14-10-2009	Final Report	13-Apr-2006 to 31-May-2009

4. TITLE AND SUBTITLE

Characterization of the nonlinear viscoelastic and adhesive properties of polyurea and characterization of polyurea-clad metallic structures

5a. CONTRACT NUMBER

5b. GRANT NUMBER

N00014-06-1-0644

5c. PROGRAM ELEMENT NUMBER

6. AUTHOR(S)

K. Ravi-Chandar and K.M. Liechti

5d. PROJECT NUMBER

5e. TASK NUMBER

5f. WORK UNIT NUMBER

7. PERFORMING ORGANIZATION NAME(S) AND ADDRESS(ES)

The University of Texas at Austin
Office of Sponsored Projects,
P.O.Box. 7726
Austin, TX 78713-7726

8. PERFORMING ORGANIZATION REPORT NUMBER

9. SPONSORING/MONITORING AGENCY NAME(S) AND ADDRESS(ES)

Office of Naval Research
Program Officer: Dr. Roshdy G. Barsoum
875 North Randolph Street
Arlington, VA 22203-3521

10. SPONSOR/MONITOR'S ACRONYM(S)

ONR

11. SPONSOR/MONITOR'S REPORT NUMBER(S)

12. DISTRIBUTION/AVAILABILITY STATEMENT

Approved for Public Release; distribution is unlimited.

13. SUPPLEMENTARY NOTES

14. ABSTRACT

This report describes the an experimental effort to characterize the viscoelastic properties of polyurea and the failure of ductile materials at high strain rates. The viscoelastic properties of cast polyurea were determined under monotonic loading conditions, both in the confined compression and Arcan shear configurations. The nonlinear viscoelastic properties have been determined and validated by predicting the large deformation compression behavior. Expanding ring experiments were performed on Al 6061-O, Al 1100-H14 and Cu 102 in order to investigate the onset and growth of necking localization and eventual failure at strain rates of about 3000 - 15000 per second. The modification of the failure behavior of these rings when coated with a polyurea layer was also examined at the same strain rates. It was demonstrated that while the polyurea did not alter the onset of localization, it did contribute to energy dissipation in the metallic ring by delaying the propagation of unloading waves in the metal. Adhesion between polyurea and steel substrate was characterized by a direct measurement of the traction-separation law.

15. SUBJECT TERMS

16. SECURITY CLASSIFICATION OF:			17. LIMITATION OF ABSTRACT	18. NUMBER OF PAGES	19a. NAME OF RESPONSIBLE PERSON
a. REPORT	b. ABSTRACT	c. THIS PAGE		121	19b. TELEPHONE NUMBER *(Include area code)*

Final report to the
Office of Naval Research

on the

Characterization of Nonlinear Viscoelastic and Adhesive Properties of Elastomers and Characterization of Polyurea-clad Metallic Structures

under the

ONR Research Grant,

N00014-06-1-0644

to

The University of Texas at Austin

PI: K. Ravi-Chandar
Co-PI: K.M. Liechti
Program Officer: Dr. R.S. Barsoum, ONR 334

Center for Mechanics of Solids, Structures and Materials
The University of Texas at Austin
1 University Station, C0600
Austin, TX 78712-0235

1. Contract Information

Contract Number	N00014-06-1-0644
Title of Research	Characterization of Nonlinear Viscoelastic and Adhesive Properties of Elastomers and Characterization of Polyurea-clad Metallic Structures
Principal Investigator	K. Ravi-Chandar
Organization	The University of Texas at Austin

2. Technical Section

2.1. Technical Objectives

Recent discussions surrounding the high rate behavior of structural enhancements through polymer coatings have provided motivation for understanding fundamental aspects of the mechanical response of both the polymer and the metal at high pressures and high strain rates. Polymer-metal adhesion under quasi-static as well as dynamic loading conditions must also be determined through direct experiment. Thus, the three main technical objectives of the program are listed below.

1. To determine the nonlinear, pressure dependent relaxation characteristics of polyurea
2. To determine the efficacy of polyurea coating on metallic specimens in the inhibition or delay of necking and associated fragmentation using the expanding ring experiment
3. To determine the adhesive characteristics of polyurea coatings on metallic substrates.

This report documents the work accomplished over the period from April 13, 2006 to May 31, 2009. The work continues under a different grant number.

2.2. Technical Approach

2.2.1. Viscoelastic Characterization of Polyurea:

The pressure dependent relaxation behavior of polyurea is determined with the confined compression loading configuration. If the specimen is confined in a cylinder of different wall-thicknesses, and axially compressed, the specimen experiences a multiaxial compressive stress state, consisting of a pressure and superposed shear. The Arcan test is used in the direct characterization of nonlinear behavior of polyurea. These results are compared with the shear behavior interpreted from the confined compression tests described above.

2.2.2. Expanding Ring Experiment for Fragmentation Studies:

Expanding ring tests have been used frequently in the characterization of high strain rate material behavior. We have used this arrangement to examine the onset of necking and fragmentation in aluminum and copper alloys and specimens coated with polyurea. Details of the experimental arrangement and results pertaining to Al 6061-O have been published (Zhang and Ravi-Chandar, 2006). This method of generating high strain rate loading is used to examine the response of other materials, and of specimens with polyurea coating.

2.2.3. Adhesion of Polyurea to Steel Substrates:

The adhesion of the coatings to steel is examined under quasi static loading through a bend test configuration; dynamic loading device based on an exploding wire is being developed under a companion

DURIP program. The former is used to determine the toughness of the interface as a function of crack growth rate and environmental exposure. The latter is to be used to evaluate strain rate effects.

2.3. Technical Accomplishments

2.3.1. Viscoelastic Characterization of Polyurea:

In previous work, we have determined the nonlinear viscoelastic behavior of sprayed polyurea (TRI material). Its behavior was affected by porosity incurred during processing. The model of nonlinear viscoelastic behavior that was considered (Chakkarapani et al 2006, Chakkarapani, 2007) was based on the modified free volume approach that allows distortional as well as dilatational contributions to the free volume and the material time clock (Popelar and Liechti, 2003). During this project period we have characterized the nonlinear viscoelastic behavior of cast polyurea, which is being used in the expanding ring experiments with polyurea coatings.

The shear and bulk relaxation moduli (linear viscoelastic behavior) were obtained from confined compression experiments under step loading. The nonlinear model was based on separate tensile, confined compression, and shear experiments under ramp loadings at various strain rates and temperatures. In the present work we attempted to streamline the process by conducting confined compression experiments under ramp loading and extracting the linear and nonlinear behavior from the small strain and larger strain portions of the response. This involves using a Volterra integral equation approach to extract the linear and nonlinear behavior. However, sensitivity and error propagation analyses indicated that inverting the Volterra integral equation with noisy experimental data was highly unstable. Therefore, we have resorted to using the traditional "ten-times" rule to get long time data. With this approach, we have completed the nonlinear viscoelastic characterization of cast polyurea and verified this with comparison of the predictions with uniaxial tensile data obtained experimentally over a range of temperatures and low strain rates. An example of such comparison is shown in Figure 1. This work has been written up in a Master's thesis (Chevallard, 2009) and will be written up for archival publication in the near future. The highlights of this work is reproduced in Appendix A.

2.3.2. Expanding Ring Tests:

Significant accomplishments were made in the expanding ring experiment. This configuration has been used to explore the development of strain localization, which is a precursor to the onset of failure. In addition to the tests on bare metal rings, polyurea coated rings have also been tested. Three manuscripts dealing with this work have been published over the last two years. Rather than duplicate the material in this report, this manuscript is attached to this report as Appendices B, C and D. The main conclusion of the study indicates that polyurea coating does not prevent or delay the onset of localization; but effects associated with the propagation of unloading waves from fractures of the metal are influenced significantly by the polyurea. Therefore the metal is able to sustain significantly greater strains than without the coating. In a follow-on program, we are evaluating the effect of polyurea coatings on aluminum tubes.

2.3.3. Adhesion of Polyurea to Metals:

Adhesion of polyurea on metallic substrates has been studied quasi-statically. These were approached with a cohesive zone model; experiments were used to determine the traction-separation law for this adhesive interface (Zhu et al. 2009). The details are in the published manuscript, attached as Appendix E.

The role of adhesion between coating and substrate on the onset of necking in the substrate was also considered in expanding ring experiments with polyurea coating on aluminum and copper specimens. The modeling effort requires the adhesion between polyurea and aluminum to be determined over a range of loading rates. For lower loading rates, we follow the approach we developed in the previous reporting period for determining the traction-separation laws for polyurea/steel interfaces (Zhu et al 2009). For higher loading rates, we have developed an exploding wire test facility for scale model experiments that

mateh the pressure pulses experieneed in blasts; the development of this faeility is supported by a companion DURIP (ONR-00014-07-1-0914) grant and was eompleted in Deeember 2008. Initial experiments were performed on bare aluminum alloy speeimens. Additional experiments with polyurea eoated aluminum speeimens are eurrently being tested through the follow-on program.

References

V. Chakkarapani, 2007, *Viscoelastic characterization of Polyurea Based Polymers*, in *Aerospace Engineering and Engineering Mechanics*. University of Texas at Austin

V. Chakkarapani, K. Ravi-Chandar and K.M. Lieehti, 2006, Charaeterization of multiaxial eonstitutive properties of rubbery elastomers, *Journal of Engineering Materials and Technology*, Transaetions of the ASME, **128**, 489-494.

G. Chevallard, 2009, Charaeterization of the nonlinear viseoelastie behavior of polyurea, MS Thesis, The University of Texas at Austin.

C.F. Popelar and K.M. Lieehti, 2003, A distortion-modified free volume theory for nonlinear viseoelastie behavior, *Mechanics of Time Dependent Materials*, **7**, 89-141.

H. Zhang, and K. Ravi-Chandar, 2006, On the dynamies of neeking and fragmentation: I. Real-time and post-mortem observations in Al 6061-O, *International Journal of Fracture,* **142**, 183-217.

H. Zhang, and K. Ravi-Chandar, 2008, On the dynamies of neeking and fragmentation: II. Effeet of geometry and duetility, *International Journal of Fracture* **150**, 3-36.

H. Zhang, K.M. Lieehti and K. Ravi-Chandar, 2009, On the dynamies of neeking and fragmentation: III. Effeet of eladding with a polymer, *International Journal of Fracture,* **155**, 101-118.

H. Zhang and K. Ravi-Chandar, 2009, Dynamie fragmentation of duetile solids, *Journal of Physics D: Applied Physics*, aeeepted July 10, 2009.

Y. Zhu, K.M. Lieehti and K. Ravi-Chandar, 2009, Direet Extraetion of Rate-Dependent Traetion-Separation Laws for Polyurea/Steel Interfaees, *International Journal of Solids and Structures*, **46**, 31-51.

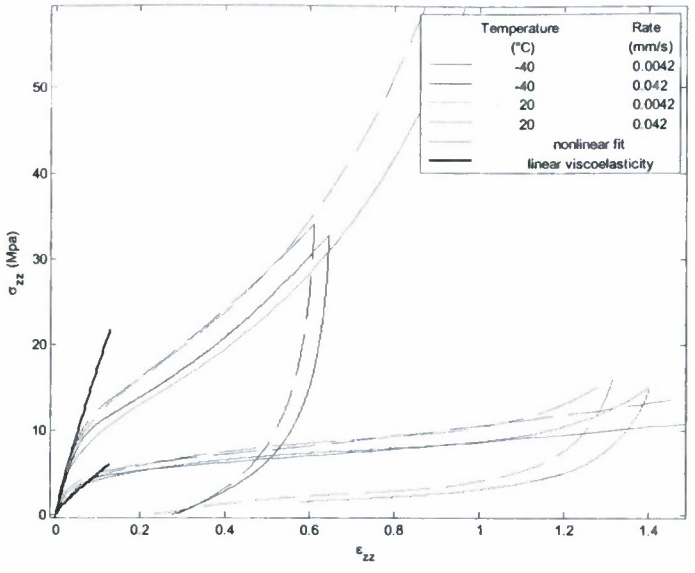

Figure 1. (a) Selected sequence of high speed images showing the onset of localization in an Al 6061-O specimen with a polyurea coating. Note that the onset of necking is clearly visible in the middle image.

APPENDIX A

Nonlinear viscoelastic characterization of cast polyurea

G. Chevallard, Kenneth M. Liechti, K. Ravi-Chandar

(under preparation for submission to a polymer journal).

Summary of results on viscoelastic characterization cast polyurea

The nonlinear viscoclastic response is modeled through an internal clock based model. In this model, the bulk and shear stresses are related to the dilatational and deviatoric strains as follows:

$$\sigma_{kk}(t) = 3\int_{-\infty}^{t} \kappa(t'-\xi')\frac{\partial \vartheta}{\partial \xi}d\xi \ , \ s_{ij}(t) = 2\int_{-\infty}^{t} \mu(t'-\xi')\frac{\partial e_{ij}}{\partial \xi}d\xi$$

where the reduced time is given by the equation:

$$t'-\xi' = \int_{\xi}^{t} \frac{1}{a_T\left[T(\tau), c(\tau), \vartheta(\tau)\right]}d\tau$$

and a_T is the shift factor that depends on the temperature, solvent concentration and the dilatational strain; it is this last dependence that brings in nonlinearity in isothermal, solvent-free conditions. The shift-factor is related to the free-volume through the following expression:

$$\log a_T = \frac{B_d}{2.303 f_d}\left(\frac{\alpha\Delta T + \beta\Delta c + \delta\vartheta}{f_d + \alpha\Delta T + \beta\Delta c + \delta\vartheta}\right) - \frac{B_s}{2.303 f_s}\left(\frac{\varepsilon_{eff}}{f_s + \varepsilon_{eff}}\right)$$

Where $\varepsilon_{eff} = \sqrt{2e_{ij}e_{ij}/3}$ is the effective strain, and B_d, B_s, f_d, f_s, α, β, and δ are material constants. In this model the free-volume is considered to be influenced both by the dilatational and distortional strains; this presumes that there is some unspecified microscale process that couples the free-volume and distortional strains. The shear relaxation modulus at small strains was measured using the Arcan shear test while the bulk relaxation modulus was measured using the confined compression apparatus. These measurements were repeated at temperatures in the range of -55 °C to 40 °C and the results were shifted to obtain the master relaxation curves shown in Figure A-1, with reduced time $t' = t/a_T$ along the abscissa. The corresponding shift factor dependence on temperature $a_T(T)$ is shown in Figure A-2. Interconversion of the bulk and shear relaxation moduli yield the uniaxial relaxation modulus and Poisson ratio variation with time as shown in Figure A-3; the interconverted uniaxial modulus is compared to direct measurements under uniaxial compression and this comparison is shown to be excellent in Figure A-3. For extensions to large strain levels and nonlinear viscoelastic regime, we resorted to ramp tests both in Arcan shear and uniaxial compression. These results are shown in Figures A-4 and A-5. The distortional parameters B_s and f_s were obtained from numerical fits of the Arcan ramp response with the nonlinear model at large strain levels. Then, the dilatational parameters B_d, f_d, and δ were obtained by fitting the bulk

behavior in confined compression ramp experiments. The values of the parameters are presented in Table A-1. The validation of the model is demonstrated by using the calibrated nonlinear viscoelastic model in a predictive mode: we considered a uniaxial compression ramp test, performed at two different strain rates, and at two different temperatures; the strain levels attained in these experiments are quite large, significantly larger than that used in the characterization of the viscoelastic properties. A comparison of the uniaxial compressive ramp responses is given in Figure A-6. While the linear viscoelastic model caputures the response quite well for nominal strain levels of around 0.6.

TABLE A-1. Nonlinear viscoelastic parameters for cast polyurea
(Reference temperature $T_0 = 0$ C)

B_d	B_s	f_d	f_s	δ
0.2	4	0.016	0.219	-0.8

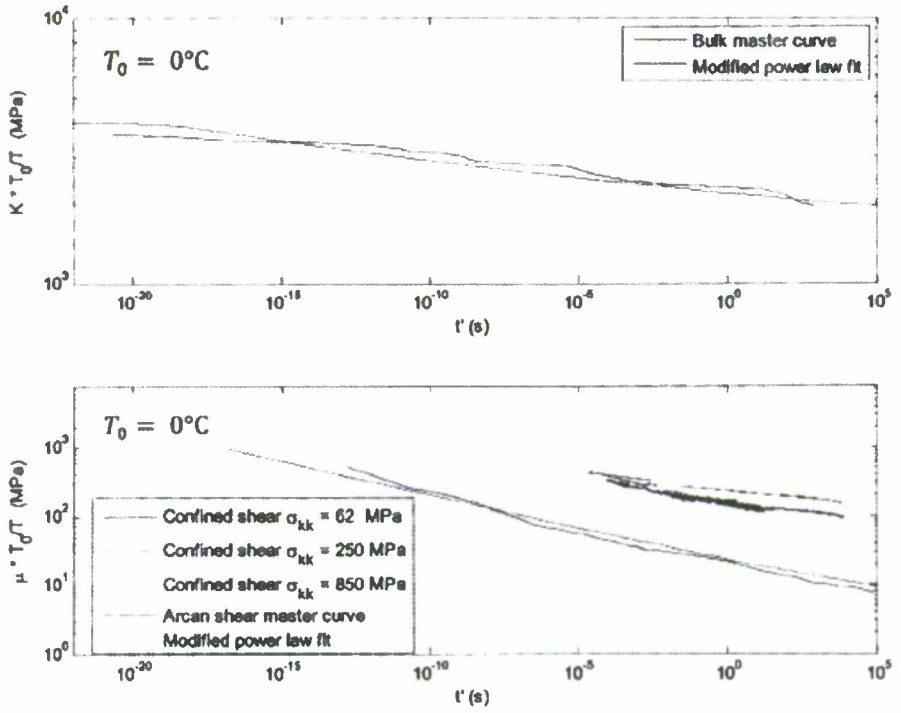

Figure A-1. Bulk and shear relaxation master curves for cast polyurea.

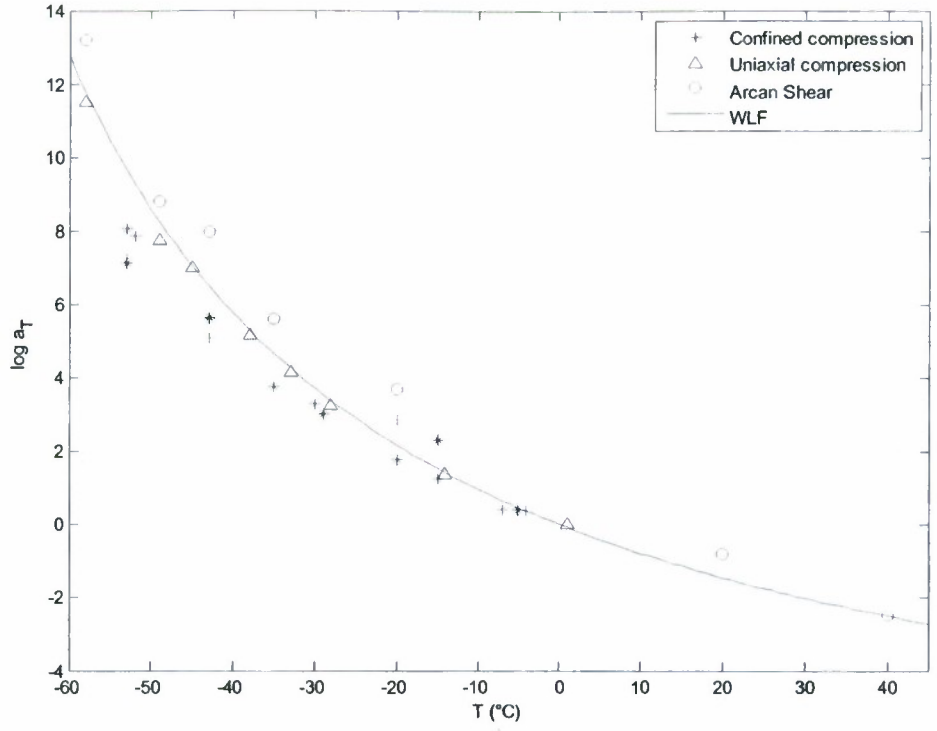

Figure A-2. Shift-factor dependence on temperature for cast polyurea.

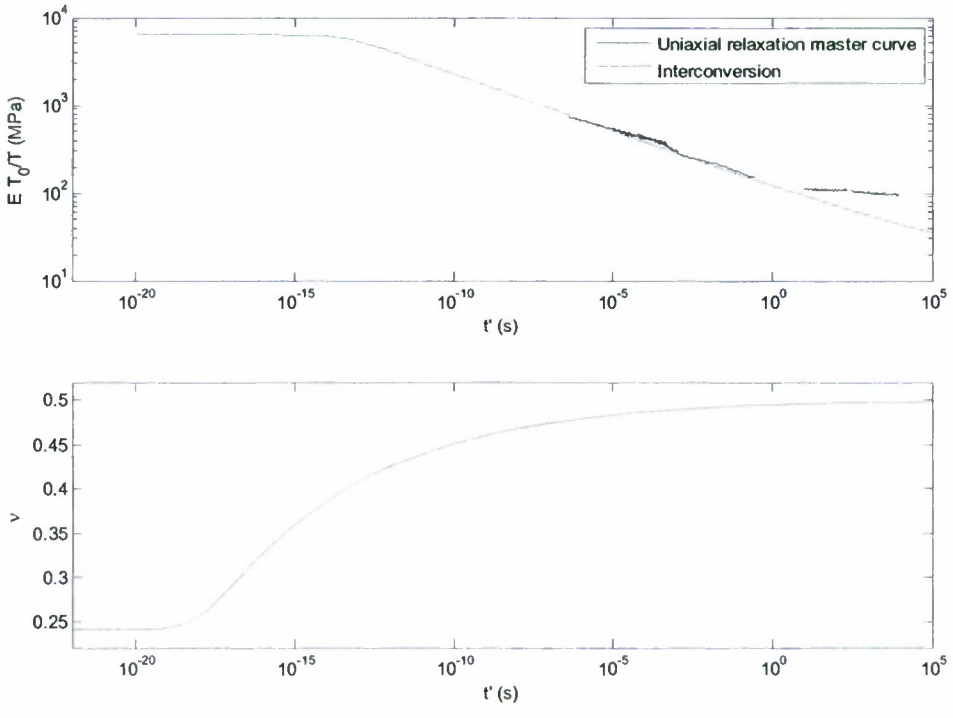

Figure A-3. Interconverted uniaxial relaxation modulus and Poisson's ratio

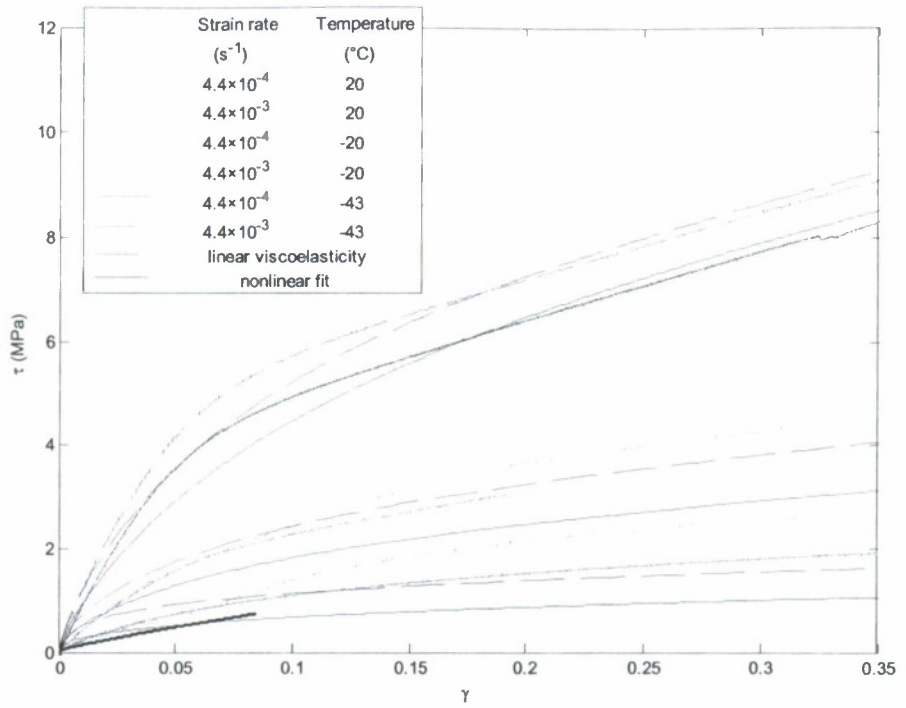

Figure A-4. Ramp tests in Arcan shear; fitting used to extract B_s and f_s.

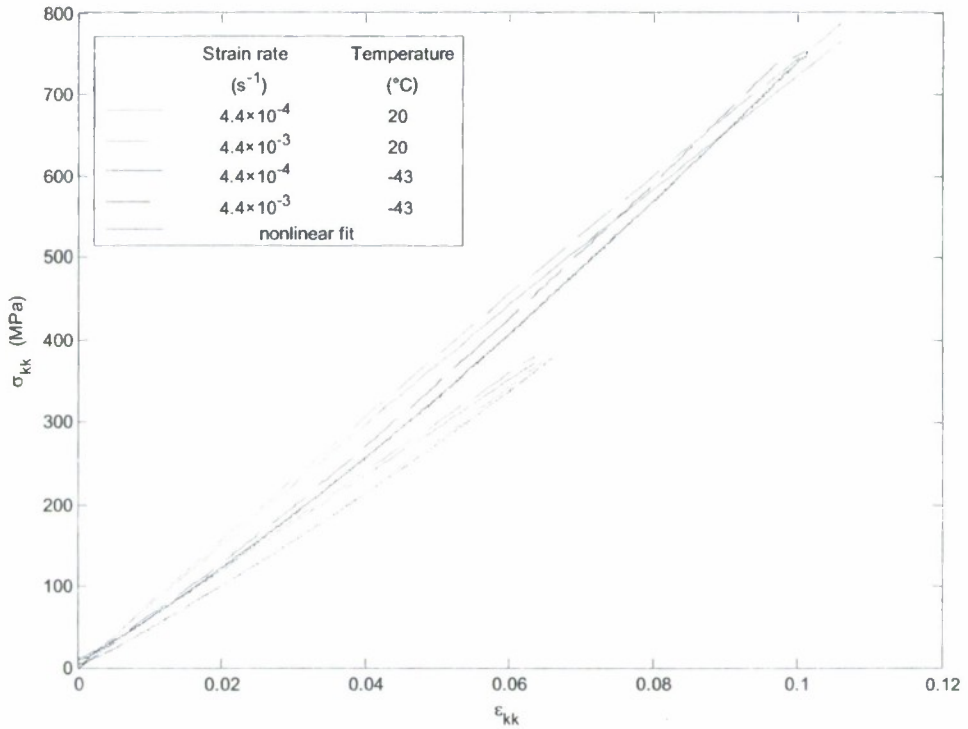

Figure A-5. Ramp tests in confined compression; fitting used to extract B_d, f_d and δ.

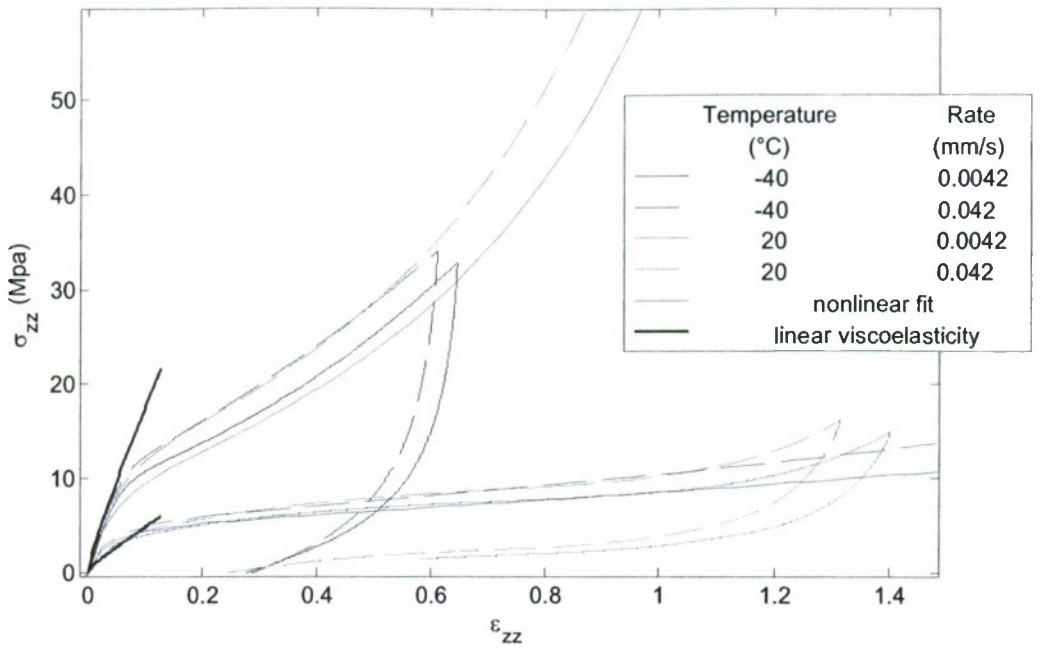

Figure A-6. Ramp tests in uniaxial compression; predictions of the linear and nonlinear viscoelastic models are shown in comparison to the experimental measurements.

APPENDIX B

On the dynamics of necking and fragmentation – II. Effect of material properties, geometrical constraints and absolute size

H. Zhang and K. Ravi-Chandar

International Journal of Fracture, **150**, 3-36.

Int J Fract (2008) 150:3–36
DOI 10.1007/s10704-008-9233-3

ORIGINAL PAPER

On the dynamics of necking and fragmentation—II. Effect of material properties, geometrical constraints and absolute size

H. Zhang · K. Ravi-Chandar

Received: 11 March 2008 / Accepted: 21 May 2008 / Published online: 8 July 2008

Abstract In this series of papers, we investigate the mechanics of deformation localization and fragmentation in ductile materials. The behavior of ductile metals at strain rates between 4000 and 15,000 s^{-1} is considered. The expanding ring experiment is used as the primary tool for examining the material behavior in this range of strain rates. In Part I, the details of the experiment and the experimental observations on Al 6061-O were reported. Statistics of necking and fragmentation were evaluated and the process was modeled through the idea of the Mott release waves both from necking and fragmentation. Finally, it was shown that the strain in the ring in regions that strained uniformly never exceeded the necking strain. In the present paper, Part II, we address the issue of strain hardening and strain-rate sensitivity. Specifically, we examine different materials—Al 1100-H14, and Cu 101—in order to determine the role of material constitutive property on the dynamics of necking. These experiments reinforce the conclusion presented in Part I that the onset of necking essentially terminates the possibility of further straining in other parts of the ring and even more importantly that there is no influence of material inertia on the strain at the onset of necking in this wide range of materials. Furthermore, the effect of aspect ratio of the specimen is evaluated; this reveals that as the aspect ratio increases beyond about five, in addition to or instead of diffuse necking, localization into the sheet necking mode is observed; in this mode, the effect of ring expansion speeds is demonstrated to result in an increase of the strain at the onset of localization. In addition, an absolute size effect is observed: larger specimens exhibit localization at larger strain levels. These observations are explained in terms of plastic wave propagation and reproduced with finite element simulations. In future contributions as part of this sequel, we will explore the effect of other geometrical constraints and the effect of a compliant cladding or coating on the development of necking and fragmentation.

Keywords Expanding ring experiment · Shear band propagation · Release waves

H. Zhang · K. Ravi-Chandar (✉)
Center for Mechanics of Solids, Structures and Materials, Department of Aerospace Engineering and Engineering Mechanics, The University of Texas at Austin, Austin, TX 78712-0235 USA
e-mail: kravi@mail.utexas.edu

1 Introduction

In this series of papers, we describe the results of experiments aimed at examining uniform deformation, onset of deformation localization, and eventual fragmentation of ductile materials at high strain rates. The importance of this endeavor to many applications and a survey of much of the early work related to the expanding ring experiment have been presented in the introduction to the first paper in the sequel (Zhang and Ravi-Chandar 2006, hereafter referred to as Part I). Details of experimental design, necessary for proper application of the loading on the specimen, and for appropriate interpretation of the observed results, were also described in Part I. The use of high speed photography with high spatial and temporal resolution enabled a careful determination of the sequence of material deformation all the way to eventual fragmentation. From such experiments on Al 6061-O, an alloy that exhibits significant strain hardening, but almost no strain-rate dependence in the range of strain rates considered (5×10^{-3} to $1.5 \times 10^{4}\,s^{-1}$), it was found that

(i) a strain-rate independent power-law hardening material model was adequate in order to predict the expansion speed of the Al 6061-O ring specimen for as long as homogeneous deformations were sustained;
(ii) localization of deformation in the form of necks appeared nearly simultaneously at several (independent) locations along the circumference of the expanding ring;
(iii) the distance between necks followed a Rayleigh distribution;
(iv) the strain at the onset of such localization was nearly equal to the quasi-static necking strain confirming the absence of strain-rate hardening effects;
(v) further straining occurred only in the necked regions and the locations in-between did not sustain plastic strain significantly beyond the necking strain; and
(vi) eventual fractures generated release waves that inhibited further deformation in the neighboring necks, as per the Mott release wave model. These release waves were determined through numerical simulations and used to identify the unloaded regions on all of the rings; it was found that without exception, the passage of release wave suppressed further growth of the necks.

Perhaps the most striking aspect of the results presented in Part I is that concerning the onset of necking. Previous researchers had suggested that there is an increase in ductility of the material with strain rate (Grady and Bensen 1983; Altynova et al. 1996), but our experiments indicated clearly that for Al 6061-O the residual strain in the fragments was in the same range as the strain at onset of necking in quasi-static experiments. In other words, the results presented in Part I indicated neither strain-rate dependence of the constitutive response of the material, nor inertial effects that are thought to push the onset of necking to larger strain levels (Gududru and Freund 2002; Xue et al. 2008). Since these experiments were performed on thin rings of Al 6061-O with cross-sectional dimensions of 0.5 mm × 1 mm, the main objective of the present work is to explore these observations further. In the present paper, Part II, we focus attention on the effect of strain-hardening of the material, strain-rate dependence, ductility, and inertial effects on the onset of necking. In order to contrast with the Al 6061-O used in Part I, here we use Al 1100-H14 that exhibits very low strain hardening, and oxygen-free, high-conductivity (OFHC) copper—Cu 101—that exhibits significant ductility, strain hardening, and possibly, strain-rate dependence in the range attainable in the expanding ring experiment. Further experiments were performed in the expanding ring configuration at the same strain rates but with a range of specimen aspect ratios and sizes, in order to explore inertial effects more completely.

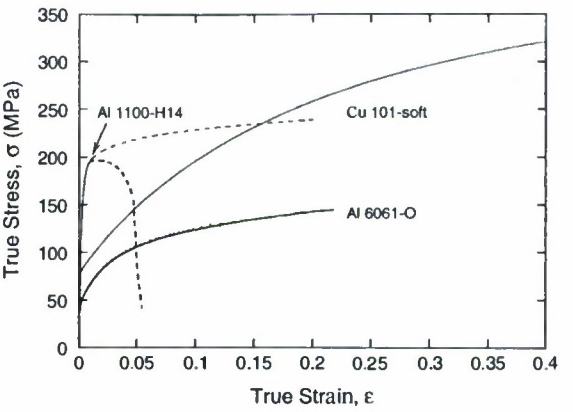

Fig. 1 Stress–strain curves of Al 6061-O, Al 1100-H14, and Cu 101. The dashed curves for Al 1100-H14 show the unloading due to localization and an estimated stress-strain relationship following a power law equation $\sigma = 226\varepsilon^{0.064}$

2 Quasi-static response of ductile materials examined

In this section, we present the quasi-static response of the three different materials considered in the present work: Al 1100-H14, Al 6061-O and Cu 101. The quasi-static material response of these materials was characterized in a tensile test in order to provide base-line material properties. Standard dog-bone shaped tensile test specimens (in compliance with ASTM standards E8M-04) were machined from the same sheets from which the expanding ring specimens were cut. Specimens with rectangular cross section of aspect ratios in the range of 2–10, matching that of the expanding ring specimens were tested. These tests were performed in an Instron testing machine, with an extensometer rated to 50% strain over a 1 inch gage length to monitor the average strain over the gage length. The strain-rate was maintained at $10^{-4}\,\mathrm{s}^{-1}$. The true-stress versus logarithmic strain variation obtained for all three materials in these tests is shown in Fig. 1.

For the Al 6061-O, the constitutive response was described in Part I; it can be taken to be a power law of the form

$$\sigma = \sigma_y \left(1 + \varepsilon_p\right)^n \tag{1}$$

The material parameters were obtained by fitting to the experimental response: $=$ 14,165, $n = 0.22$, and $\sigma_y = 25$ MPa. Localization in the form of a diffuse neck was observed in these uniaxial tests close to the maximum load point for specimens of aspect ratio of two; the strain at the onset of diffuse necking was found by averaging two tests to be: $\varepsilon_N^{qs} = 0.22$; this corresponds closely to the Considère strain or the strain at the limit load. As the aspect ratio increased above five, in addition to the diffuse necking localization, a second localization in the form of a shear band was observed within the necked region; this corresponds to the "sheet-necking" mode, with the critical strain at this localization given by the analysis of Hill 1952). From Hill's analysis, the bifurcation strain for the sheet necking mode is given by

$$\varepsilon_{sn} = \frac{n}{1+\rho}, \quad \tan\alpha_{sn} = \quad \overline{-\rho} \tag{2}$$

where ρ is the ratio of biaxiality of the strains and n is the strain hardening exponent in Eq. 1). α_{sn} is the angle of inclination of the shear band with respect to the normal to the tension direction. For the case of uniaxial tension, $\rho = -0.5$; therefore, we get $\varepsilon_{sn} = 2n$, implying that the strain at the onset of sheet necking is twice the Considère strain at the limit load and

the angle of the shear band is $\alpha_{sn} = 35.26°$. Since this analysis does not predict localization under biaxial tension (that is typically observed in sheet forming operations), Storen and Rice (1975) and Hutchinson and Neale (1978) reexamined the problem with a corner theory of plasticity; their analysis provides a prediction of the strain at localization under biaxial tension and reduces to the Hill criterion under uniaxial loading on a sheet. Tvergaard (1993) performed numerical simulations of necking modes in tensile bars with a rectangular cross-section and showed that the post-bifurcation response depended significantly on the aspect ratio of the cross-section and more importantly that while the local strain at the point where the sheet-necking localization occurs is $\varepsilon_{sn} = 2n$, the average strain over the entire specimen doesn't reach this level except in extremely short specimens. Thus, in quasi-static experiments on thin rectangular specimens, one never reaches $\varepsilon_{sn} = 2n$ over the entire specimen; global strain measures will not capture this effect and one needs to perform local analysis.

Al 1100-H14 exhibits very low strain hardening; as a consequence, it is very difficult to obtain the true stress–strain response for large strains directly from measurements in the standard configuration. Localization, either in the form of diffuse necking and/or shear banding intervenes at very low global strain levels and further deformation is concentrated in these regions. This is apparent in the test result shown in Fig. 1, since the specimen begins to unload at global strain levels of about 0.01. In order to explore this further, we adopted a digital image correlation scheme (Chu et al. 1993) to monitor the strain variations along the length of the specimen. Figure 2 indicates the result of this scheme: in this figure, two images of specimens that exhibited shear banding are shown. Also, strain maps over the gage length of the specimen obtained from the digital image correlation are shown at global strain levels from 1% to 2%. As can be seen from the contours of strain levels in Fig. 2, while the global strain is about 0.012 the strain in the weak spots of the material have already developed to about 0.05. We note that these are not large geometrical flaws; the specimens were cut with an electric discharge machining system so that geometrical variability is negligibly small. We believe that the localization triggering defects are microstructural in nature. The localization is then triggered by this defect and propagates across the specimen at the characteristic angle α_{SN} as the global strain is increased further; by the time the global

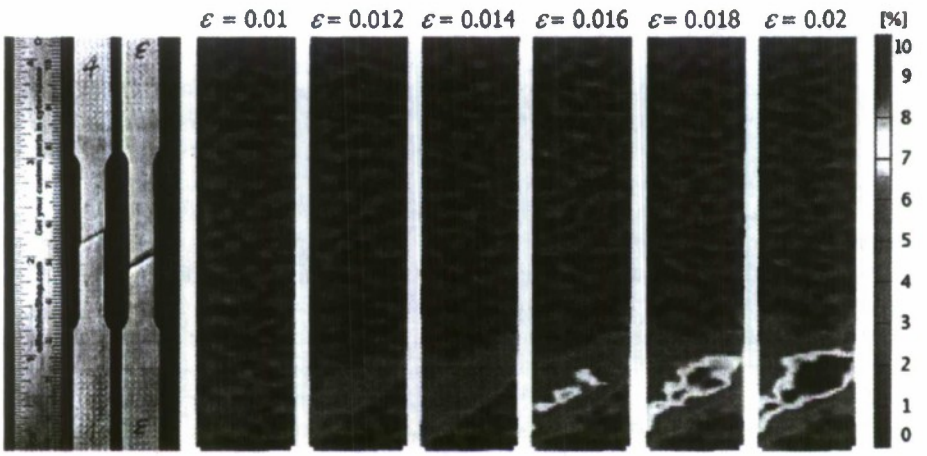

Fig. 2 Localization of Al 1100-H14 specimen under quasi-static tension. Strain contours obtained with a digital image correlation technique are shown to illustrate the onset of localization at very low global strain levels

strain reaches about 0.02, the sheet mode localization is fully developed across the width of the specimen and further straining occurs only within this band; the rest of the specimen never experiences a strain larger than 0.02 in this quasi-static test; thus the tension test doesn't directly yield the stress–strain curve beyond this strain level. However, if we use the Hill criterion for sheet mode necking, and anticipating results on dynamic necking reported later in Sect. 3.1, we suggest that the hardening exponent for the Al 1100-H14 should be $n \sim 0.064$; we take this as the proper exponent in the constitutive equation in Eq. 1 for Al 1100-H14. An estimate of the stress-strain curve based on this exponent is shown by the dotted line in Fig. 1.

For the soft, oxygen-free high-conductivity (OHFC) copper the stress–strain curve is also shown in Fig. 1. Fitting the power-law hardening model of Eq. 1, we obtain $n \sim 0.3$; it is apparent that this material exhibits significantly greater strain hardening than the aluminum alloys. From this uniaxial test, it was determined that the strain at diffused neck formation was about 0.3, close to the Considère strain. Once again, for specimens with an aspect ratio larger than 5, the sheet necking localization or shear band is observed. The aluminum alloys considered in this study are known to be rate insensitive at strain rates below about $10^5\,s^{-1}$; so, the quasi-static response presented above is expected to be adequate in characterizing the expanding ring experiments, where the maximum strain rate encountered is about $1.5 \times 10^4\,s^{-1}$. Furthermore, in Part I, we indicated that this is appropriate for Al 6061-O. In contrast, OFHC copper is known to be rate-sensitive; there are many experimental measurements and theoretical models that capture this rate dependence such as the commonly used thermally activated plastic flow model of Follansbee and Kocks (1988). Many authors have performed experiments at different strain rates and temperatures in an effort to determine the parameters for these plastic flow models for Cu 101 (Follansbee and Kocks 1988; Tong et al. 1992; Nemat-Nasser and Li 1998). However, there is wide variation in the strain-rate level beyond which the importance of strain-rate manifests itself significantly, ranging from 10^3 to $10^6 s^{-1}$; we will defer consideration of this issue to a later sections in this paper as we interpret experimental results.

3 Results of expanding ring experiments

3.1 Al 1100-H14 and OFHC Cu 101

Numerous expanding ring experiments were performed on Al 1100-H14 and OFHC Cu 101 specimens with strain rates in the range of 4000 to $15{,}000\,s^{-1}$. The parameters of the loading coil used in these experiments are given in Table 6 of Part I. Current traces in both the coil and the specimen were obtained in each case as described in Part I; this enables the determination of the driving force in the experiments. Tables 1 and 2 list the experimental conditions achieved for the Al 1100-H14 and the Cu 101 specimens respectively; the conditions of the tests on Al 6061-O are documented in Table 1 of Part I. Two composite images of the ring expansion tests in the Al 1100-H14 and Cu 101 are shown in Figs. 3 and 4 respectively. In general, all the qualitative features of necking and fragmentation observed and documented in Part I with respect to Al 6061-O were observed in these materials as well.

The variation of the ring radius with time measured from experiments in the aluminum and copper specimens is shown in Figs. 5 and 6, respectively. In the first stage of deformation, the ring expands uniformly at speeds in the range of about 65 to 230 m/s, corresponding to a strain rate of 4000 to $15{,}000\,s^{-1}$. In this stage, the system of ordinary differential equations governing the coupled response of the deformation of the ring and the electromagnetic loading

Table 1 List of high speed expanding ring tests on Al 1100-H14 with $\alpha = 2$

Test no.	Charging voltage (kV)	Velocity ($m s^{-1}$)	Number of necks	Number of fractures	ε_u^R
1	5	84	20	5	0.0709
2	5	81	20	4	0.0580
3	6	121	27	7	0.0540
4	6	122	31	8	0.0667
5	7	171	31	12	0.0582
6	7	171	33	11	0.0540
7	8	228	37	13	0.0711
8	8	224	41	13	0.0669

Table 2 List of high speed expanding ring tests on Cu 101 with $\alpha = 2$

Test no.	Charging voltage (kV)	Velocity ($m s^{-1}$)	Number of necks	Number of fractures	ε_u^R
1	5	67	4	1	0.2638
2	5	65	2	1	0.2773
3	6	96	15	3	0.3090
4	6	92	10	3	0.2999
5	7	121	22	6	0.3091
6	7	121	24	9	0.2956
7	8	144	32	11	0.3275
8	8	143	30	9	0.2953
9	9	170	26	10	0.3320
10	9	173	30	11	0.3274

scheme are given in Eqs. 3–6, 8, 11 and 12 of Part I. In addition, for a given constitutive response, the ring radius and current may be calculated as a function of time for a given input current. As reported in Part I for Al 6061-O, the strain-rate independent constitutive model in Eq. 1 was adequate in reproducing both the measured specimen current and the ring radius as a function of time. While this was true for the Al 1100-H14, for the Cu 101, there is a very small deviation in the estimated speed at the highest expansion speed. Therefore, the present results suggest that strain rate effects may not be significant at strain rates of about $10^4\,s^{-1}$. While this conclusion is not surprising for the Al 1100-H14, this is somewhat at odds with reported strain-rate dependence for the copper; some reports in the literature suggest that strain-rate effects may be important at strain rates as low as $10^3\,s^{-1}$, while other results indicate that the strain rate has to exceed $10^6\,s^{-1}$. Complicating this issue further, Gorham (1991) demonstrates that an absolute size effect might exist as a result of inertial effects. Hence, we note that the observations made in this section are applicable only to the specimen types used in these experiments, with cross-sectional aspect ratio of about two; we will return to this issue in Sect. 4. The stage of uniform plastic straining is terminated by the onset of localized deformation.

In the second stage, numerous necks nucleate nearly simultaneously at many locations around the ring. Statistical analysis shows that the distance between necks follows trends similar to that shown in Fig. 16 of Part I; the Weibull exponent is typically in the range of two indicating that a Rayleigh distribution captures the statistics of neck nucleating defects. The distributions of the distance between necks for Al 1100-H14 and Cu 101 are shown in Figs. 7 and 8 respectively; included in each figure is the variation with the ring expansion

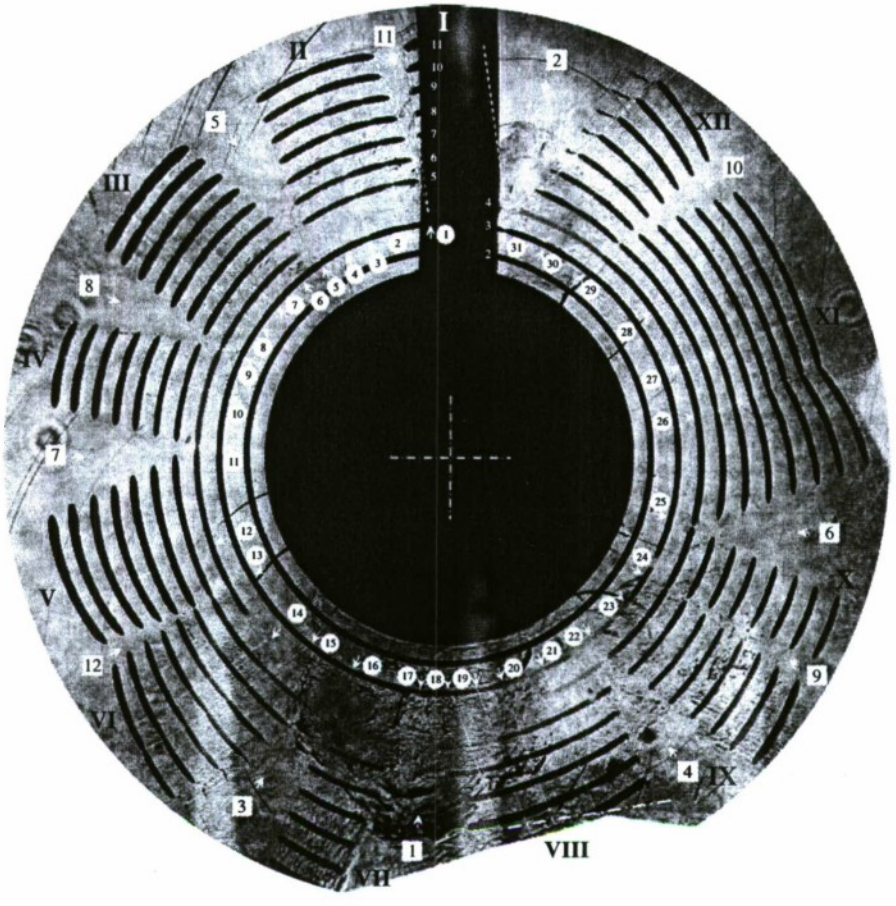

Fig. 3 Composite image for an Al 1100-H14 ring expanding test (Table 1: test #5). The expanding velocity is 171 m s^{-1}. The frame numbers are identified along the top. The necks are identified at the location of their appearance by the numbers inside circles, numbering them counterclockwise. The fracture locations are identified by the numbers inside squares, numbering them in the time sequence of their appearance. The trajectories of the necked locations are marked by the white dotted lines

speed (or equivalently the strain rate). Once again, with increasing strain rate, more necks are nucleated at shorter distances since the unloading engendered by any localization does not travel far enough quickly to inhibit further nucleation at neighboring locations. While the high speed images do not have sufficient temporal resolution to identify the exact strain at onset of localization, we infer this strain by measuring the uniform strain, ε_u^R, in the unnecked portions of the specimen fragments as described in Sect. 4.5 of Part I. The measured ε_u^R is plotted as a function of expanding velocity in Fig. 9 for the Al 1100-H14 and Cu 101; previous experimental results on Al 6061-O are also reproduced in this figure for easy comparison. The dashed lines indicate the necking strain ε_N^{qs}, obtained from quasi-static tensile experiments. For Cu 101, a very repeatable value of $\varepsilon_N^{qs} = n = 0.3$ was obtained; thus, as in case of Al 6061-O, the copper specimens did not experience a strain larger than the Considère strain, reinforcing the conclusions of Part I. For the Al 1100-H14, an estimate of the necking strain based on the data from dynamic localization measurements is about 0.063; based on this we

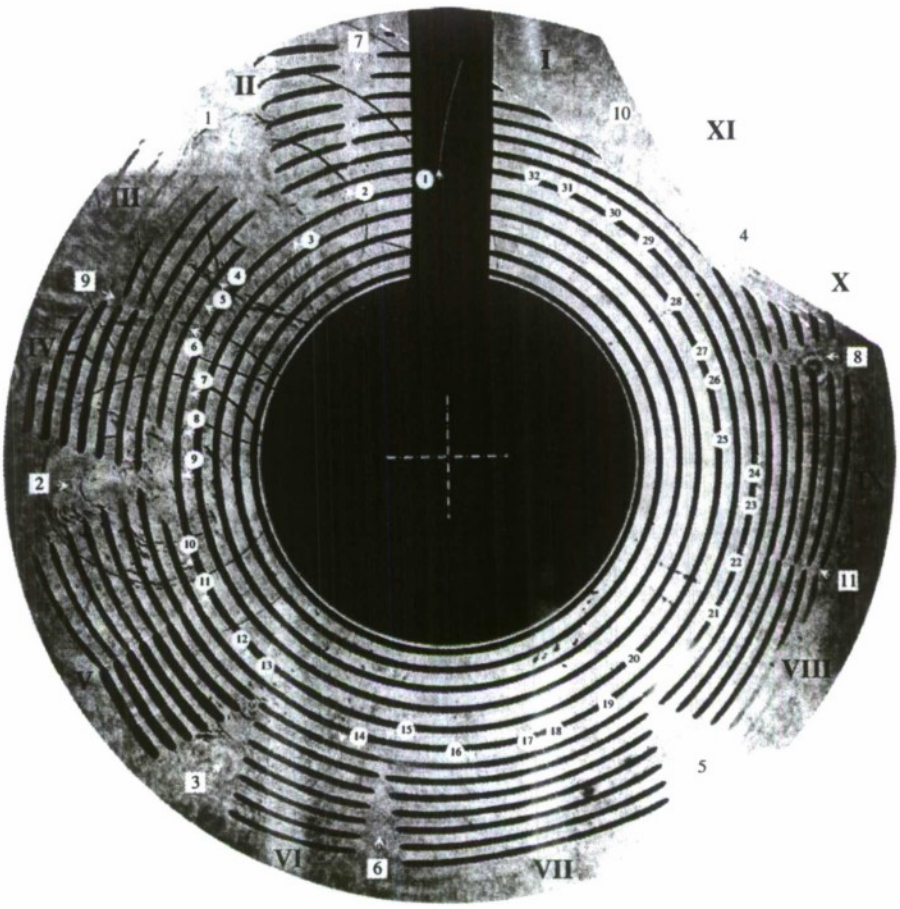

Fig. 4 Composite image for a Cu 101 ring expanding test (Table 2: test #7). The expanding velocity is $144\,\mathrm{m\,s^{-1}}$. The frame numbers are identified along the top. The necks are identified at the location of their appearance by the numbers inside circles, numbering them counterclockwise. The fracture locations are identified by the numbers inside squares, numbering them in the time sequence of their appearance. The trajectories of the necked locations are marked by the white dotted lines

suggest that a hardening exponent of 0.063 as discussed in Sect. 2. Thus, it is seen that the strain at onset of localization, in the three materials examined so far, does not depend on the rate of loading. In other words, *there is neither an inertial, nor a material strain-rate effect on the strain at the onset of necking localization.*

Comparison of these experimental results to analytical predictions is shown in Fig. 10. Guduru and Freund (2002) considered an axisymmetric rod of length $2L$ and radius r_w. Homogeneous deformation at a constant strain rate $\dot{\varepsilon} = \pi v_0/L$ was imposed over the entire rod, in order to mimic strain rates obtained in the ring expansion experiment at a speed v_0. The material was modeled as a hypoelastic material, derived from Storen and Rice (1975). Sinusoidal perturbations in the axial and radial deformations of the rod, consistent with the incompressibility of the material, were imposed. The equations of motion, linearized about the homogeneous state, were then examined to determine conditions under which these perturbations would continue to grow. Their results predict that while all perturbations grow,

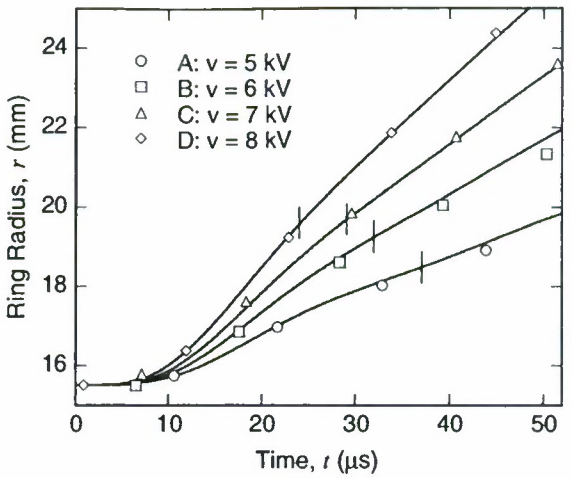

Fig. 5 Variation of the ring radius with time for Al 1100-H14 at four different capacitor charge levels. The solid lines are estimated based on the analysis described in Part I. The vertical bars indicate the time at which the first fracture occurred

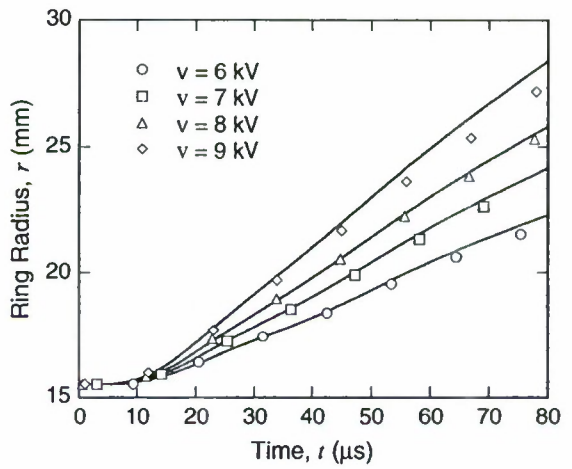

Fig. 6 Variation of the ring radius with time for Cu 101 at four different capacitor charge levels. The solid lines are estimated based on the analysis described in Part I

corresponding to any particular strain level, there is a critical wavelength of the perturbation that exhibits maximum growth rate. However, there exists no criterion to select the strain level. Thus, they left the growth rate as a free parameter and determined the wavelength of the perturbation that maximized the growth rate corresponding to a specific strain or stress level. This wavelength may be taken as an estimate of the distance between necks. The results of Guduru and Freund (2002) indicate a very modest increase in the necking strain as shown in Fig. 10—about 10% over strain rates from 4000 to 15,000 s^{-1}; this variation lies within the scatter in the experimental results. However, as shown in Fig. 17 of Part I, the distance between necks exhibits a very large variation; in particular, there are very large lengths of the ring ($3w - 12w$)—much longer than the critical wavelengths predicted by the perturbation analysis—that remain completely homogeneously deformed. While geometrical or material imperfections may induce localization at smaller strain levels or at closer spacing than predictions, the absence of necks over lengths much larger than the critical wavelength suggests that statistical aspects or other effects not included here influence neck generation much more than phase-correlated growth of small amplitude perturbations. We will return to this problem through numerical simulations in Sect. 4.

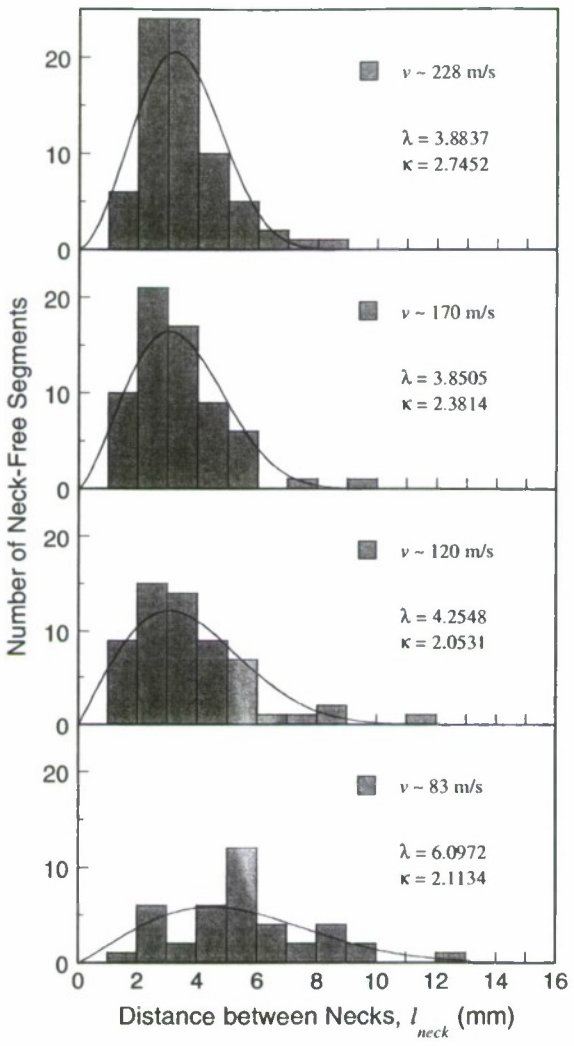

Fig. 7 Distribution of the distance between necks for Al 1100-H14.

In more recent work, Xue et al. (2008) performed a two-state band analysis of neck generation; they considered the necked region to be composed of two segments, each in a homogeneous state, but with one segment being smaller in transverse dimension than the other, with the entire system subjected to a uniform global strain rate. This is an extension of the analysis of sheet necking under quasi-static loading by Marciniak and Kuczynski (1967). Similar analyses have been performed by Fyfe and Rajendran (1982) and others. Integrating the one-dimensional equation of motion over the characteristic length of the two segments, Xue et al. (2008) obtain an ordinary differential equation relating the stresses and strains in the two segments. Embedded in this is the assumption of a quasi-steady state over the length of the two segments. This analysis indicates that the strain in the smaller segment begins to develop more rapidly than in the larger of the two segments; identifying this departure as the onset of necking, Xue et al. (2008) calculated the critical strain at onset of necking as a function of the strain rate. There are two main adjustable parameters in the two-state model:

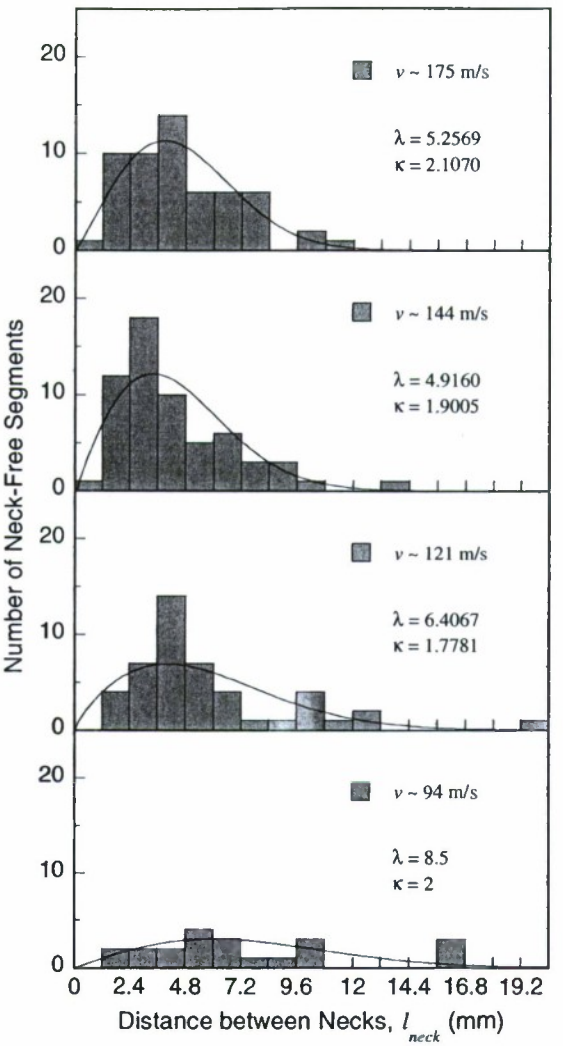

Fig. 8 Distribution of the distance between necks for Cu 101

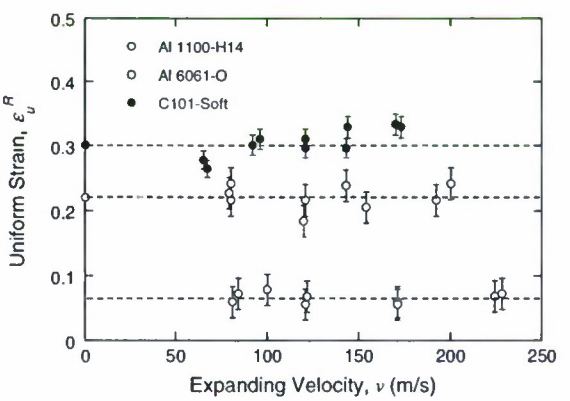

Fig. 9 Measured residual strain in the uniform segments of the fragment, ε_u^R, as a function of expanding velocity for Al 1100-H14 and Cu 101; results on Al 6061-O from Part I are also included in this figure. The quasi-static necking strain ε_N^{qs} (Considère strain) is shown by the dashed lines for each material

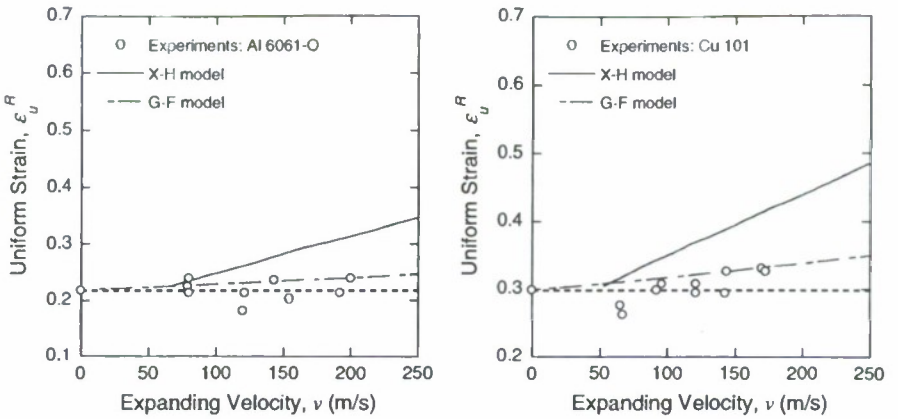

Fig. 10 Comparison of the experimental results to analytical predictions of the necking strain in Al 6061-O and Cu 101. X–H represents estimates of the Xue et al. (2008) model and G–F is based on the analysis of Guduru and Freund (2002)

the size of the thickness imperfection, $_0$ and the ratio of the lengths of the two segments, R. The two-band model indicates that a significant increase should be observed in the strain at localization, but that this prediction is not too sensitive to the two key geometrical parameters. The predictions of the two-state band model are shown in Fig. 10 and compared with the experimental observations; clearly, the two-state band model over estimates the strain at which localization occurs. We interpret the lack of correspondence between the perturbation and two-state models and the experiments to indicate that while both analyses indicate a critical strain for onset of localization, quantitative comparisons are not appropriate since the process is dominated by effects ignored in the models (as discussed later in Sect. 4) and by statistical variations in the material properties that trigger localization.

In the third stage of deformation, the earliest necks grow into fractures; when the fracture surfaces separate beyond the arcing distance, current flow is interrupted and no further loading of the specimen occurs. Nevertheless, multiple fractures occur since the unloading from each fracture diffuses through the specimen per the Mott analysis very slowly (see Part I for a discussion of this process). The fragment size distribution, when normalized by the Mott release wave scale provides a unified characterization at all expanding speeds; Weibull fit to the fragment size distribution for all three materials examined is shown in Fig. 11. Therefore the interpretation provided in Part I, that fragmentation following necking is fully described in terms of the Mott release waves (Mott 1947), is confirmed in the experiments with Al 1100-H14 and Cu 101. No significant differences result from differences in the strain hardening behavior and ductility of the material.

In all of the experiments reported above, the cross-sectional aspect ratio of the specimen has been maintained at two and furthermore, all specimens were 1 mm by 0.5 mm in cross sectional dimension. Such thin specimens were chosen primarily because one can justify a simple one-dimensional analysis by assuming uniformity across the cross-section. However, extension of the one-dimensional behavior investigated here to multiaxial stress states in structures of various dimensions and shapes used in practical applications requires special care. In particular, since the diffuse necking localization observed here is an inherently structural response specific to small cross-sections, additional experiments are required to determine the true material response under various geometric constraints. In the following

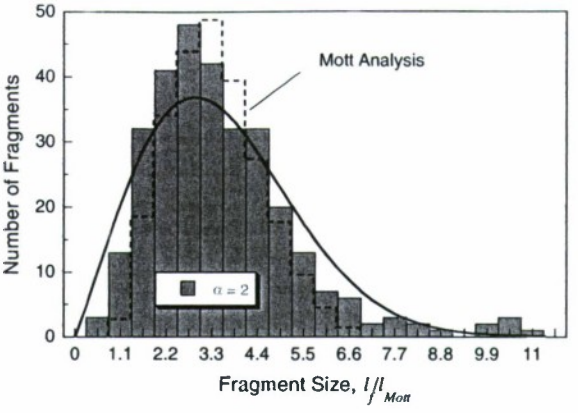

Fig. 11 Distribution of the fragment size normalized by the Mott scaling length l_{Mott}, (defined in Part I) for Al 1100-H14, Al 6061-O, and Cu 101. The solid curve is a Weibull distribution fit ($\lambda = 3.99$, $= 2.08$, $A = 166.65$) to the fragment size; the dashed curve is obtained following Mott's numerical method

sections, we examine the influence of constraints introduced by the specimen aspect ratio and by the absolute specimen dimensions.

3.2 Effect of specimen aspect ratio

It is well-known from quasi-static tests that as the cross-sectional aspect ratio of the specimen increases, in addition to the diffuse necking that appears just beyond the Considère strain, a localized shear band (sheet necking mode) emerges at the Hill strain; see the image shown in Fig. 2 that shows the shear band localization. Tvergaard (1993) examined the quasi-static shear localization problem numerically in specimens with rectangular cross-section and showed that the sheet necking mode appears when the cross-sectional aspect ratio is larger than about five. Therefore, might one anticipate similar transitions under dynamic loading? The effect of high strain rates on this kind of localization is not apparent. Therefore, we examine the issue experimentally; this will be followed in Sect. 4 by numerical simulations in order to understand the nucleation and growth of dynamic strain localization.

Here, we maintain the thickness of the ring to be 0.5 mm, but vary the length (along the axis); specifically, using lengths of 2, 3 and 5 mm results in cross-sectional aspect ratios of 4, 6 and 10 respectively. The ring radius is dictated by the coil used to drive the currents and is 15.25 mm in all the experiments. Tables 3 and 4 list the experimental conditions achieved in the Cu-101 and Al 6061-O specimens. From the sequence of high speed images of these rings, we observe that the ring experiences uniform radial expansion initially, interrupted by localization beyond a critical strain level. The main observations from this series of experiments are listed below:

1. A composite image of the expansion of two different Cu 101 rings is shown in Fig. 12. In this image the last high speed photographs of the ring in which homogeneous deformation is observed, corresponding to rings with aspect ratios $\alpha = 2$ and $\alpha = 6$, are shown on the left and right sides, respectively; in the notation of Part I, they represent the lower bounds, ε_N^{LB} for the necking strain. The effect of aspect ratio is clearly visible in this figure: as the aspect ratio increases, the strain at the onset of localization increases significantly.
2. Similar experiments were performed with the Al 6061-O specimens with aspect ratio $\alpha = 10$; again, an increase in the strain at localization was observed.
3. Post-mortem images of the fragments from specimens of Cu 101 with aspect ratios of $\alpha = 2$ and 6, and of fragments from Al 6061-O with aspect ratio $\alpha = 2$, 4, and 10 are shown in Fig. 13. When $\alpha = 2$, only diffuse necking is observed; when $\alpha = 4$ or 6, the

Table 3 List of high speed expanding ring tests on Cu 101 with $\alpha = 6$

Test no.	Charging voltage (kV)	Velocity (ms^{-1})	Number of necks	Number of fractures	ε_u^R
1	7	81	10	1	0.2638
2	7	82	9	1	0.2773
3	8	100	12	5	0.3090
4	8	104	14	5	0.2999
5	9	131	18	7	0.3091
6	9	129	15	6	0.2956
7	10	145	21	10	0.3275
8	10	152	16	9	0.2953

Table 4 List of high speed expanding ring tests on Al 6061-O with $\alpha = 10$

Test no.	Charging voltage (kV)	Velocity (ms^{-1})	Number of necks	Number of fractures	ε_u^R
1	7	86	3	1	0.3561
2	7	120	8	2	0.4623
3	9	160	13	6	0.5692
4	8	160	13	5	0.5611

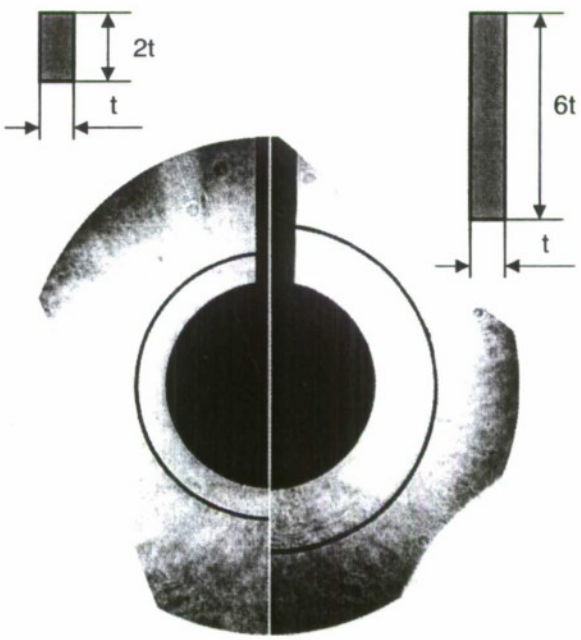

Fig. 12 Composite image of expansion of Cu 101 ring with aspect ratio $\alpha = 2$ (left image Test #10: Table 2) and specimen with aspect ratio $\alpha = 6$ (right image; Test #8: Table 3); these images show the last high speed photograph in each test that exhibited uniform expansion of the specimen. They represent the lower-bound estimate ε_N^{LB} for the strain at the onset of localization

localization observed is either a diffuse neck alone or a diffuse neck with a localized shear band within it; on the other hand, when the aspect ratio is equal to 10, only localized shear bands and the fractures that appeared within the localized shear band can be identified. We note that the ring specimen is nominally under uniaxial stress (although inertial effects could alter this slightly) and thus the Hill analysis would indicate sheet mode necking should appear at an angle of $\alpha_{SN} = 35.26°$ at a strain level $\varepsilon_{SN} = 2n$. From Fig. 13,

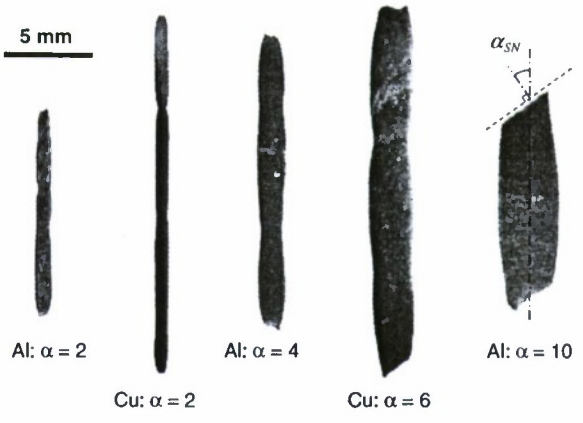

Fig. 13 Post-mortem images of the fragments from specimen of Al 6061-O and Cu 101 exhibiting the effect of aspect ratio on the type of localization observed

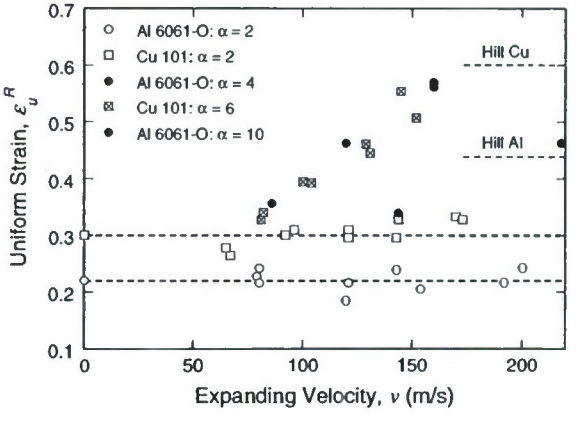

Fig. 14 Variation of ε_u^R with the ring expansion speed for Cu 101 with aspect ratio $\alpha = 6$, and Al 6061-O with aspect ratio $\alpha = 4$ and $\alpha = 10$; the result for $\alpha = 2$ is also shown for comparison

we see that the measured angle of $\alpha_{SN} \sim 37°$ suggests that the specimen is under nearly uniaxial strain conditions, at least on the time scale over which this localization appeared.

4. We determine the variation of the width of the fragment along its length and from this measurement, determine the uniform residual strain ε_u^R within the fragments as described in Part I. The variation of ε_u^R with the ring expansion speed is shown in Fig. 14 for Cu 101 specimens with aspect ratio $\alpha = 6$, and for Al 6061-O specimens with aspect ratio $\alpha = 4$ and $\alpha = 10$. The dependence of the localization strain on the rate of expansion becomes evident in these results; in other words, we see uniform straining of the rings for strain levels that are significantly larger than the Considère strain, but with this level depending on the ring expansion speed and the specimen aspect ratio. For the case of Cu 101, uniform strain appears to strain levels between the Considère strain of 0.3 and about 0.6 as the strain rate is increased from about 4000 to 15,000 s^{-1}. For the case of Al 6061-O an even more dramatic three-fold increase from the Considère strain of 0.22 to almost 0.6 is observed. We note that the Hill strain level for sheet mode necking is $\varepsilon_{SN} = 2n$, and the Al 6061-O specimen exceeds this level significantly.
5. From the collection of results for these two materials, it appears that a dependence of the localization strain on the strain-rate could be postulated, but in view of the results on specimens with aspect ratio of two, where we have already shown that inherent strain-rate dependence is negligible in these two materials, one must look elsewhere for this

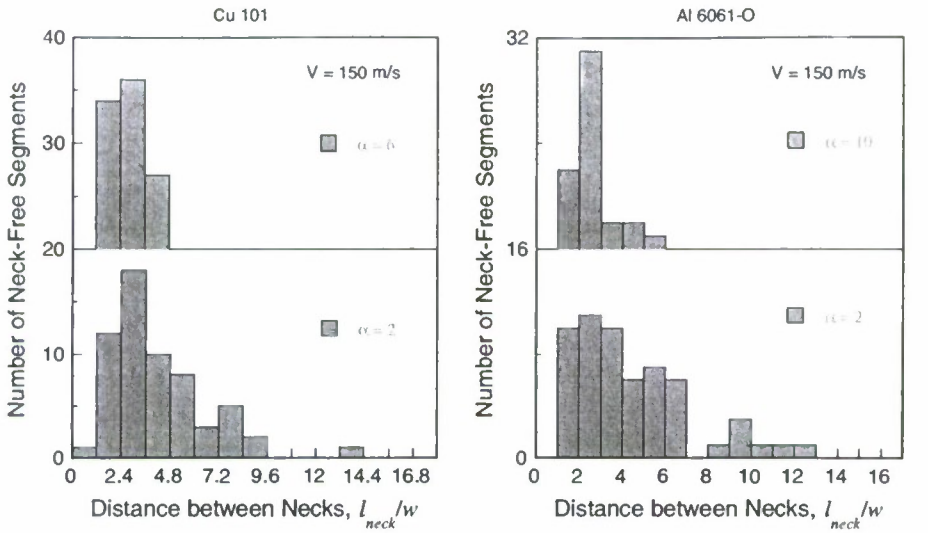

Fig. 15 Distribution of the distance between necks for: (a) Cu 101 with aspect ratio $\alpha = 2$ and $\alpha = 6$; and (b) Al 6061-O with aspect ratio $\alpha = 2$ and $\alpha = 10$

dependence on the expansion velocity! We believe that this points to inertial effects, not in the onset of localization, but in the *propagation of the localization* as the key ingredient in dictating how the localization develops across the entire specimen.

6. In terms of the statistics of neck generation, some of the trends observed for the small aspect ratio specimens—such as an increase in the number of necks and a decrease in the average distance between necks with increasing ring expansion speed—persist for specimens with larger aspect ratio. However, significant differences appear depending on the aspect ratio of the specimen. The distribution of the distance between necks (diffuse or localized) normalized by the width of the specimen is shown in Fig. 15, for different aspect ratios and different materials, but corresponding to the same expanding velocity. The distributions shown in Fig. 15 indicate a couple of interesting features. First, the distribution peaks at slightly below 3 for all cases. Second, the distribution is seen to be truncated sharply at about $5w$ for the larger aspect ratio specimens; this absence of long segments without necks is in sharp contrast to specimens with smaller aspect ratio where we observe a significant number of large segments ($\sim 12w$) without any localization. Given that the inherent population of defects in the two different sets of samples of different aspect ratio should be statistically similar, the observed difference in the distance between necks should arise from a mechanical contribution. We will explore this through simulations in Sect. 4.
7. The distribution of fragment size, normalized by the Mott scaling length is shown in Fig. 16; fragmentation data from different aspect ratio specimens, different expanding velocities, and the two different materials are all included in this set. This figure once again demonstrates the effect of the Mott release waves in dictating the statistics of fragmentation.

Whence the dependence of the necking strain on the expanding velocity of the ring for large aspect ratio specimens? Before answering this question, we perform another set of experiments to bring absolute size effects into the picture; if inertia plays a significant role,

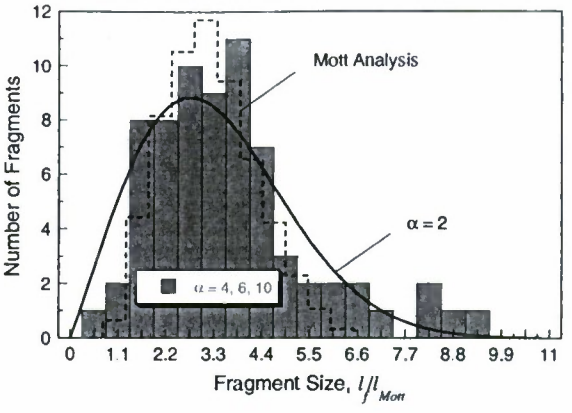

Fig. 16 Distribution of the fragment size normalized by the Mott scaling length l_{Mott}, (defined in Part I) for Cu 101 with $\alpha = 6$, and Al 6061-O with $\alpha = 4$ and $\alpha = 10$. The solid and dashed curves are the same as in Fig. 11

a characteristic time scale that depends on the specimen length and the characteristic plastic wave speed is brought into play. We present in the next section a set of experiments that examine this characteristic.

3.3 Effect of specimen size

The aspect ratio effect was examined in the previous section; here we explore the absolute size dependence of necking and fragmentation. We explore the size effect based on a conjecture that localization of deformation must occur over a small volume either within the bulk of the specimen, or more likely on the surface of the specimen, quite oblivious of the structural dimensions of the body, and then propagate across characteristic cross-sectional dimensions before structural localization in the form of a diffuse neck and/or shear band occurs over the entire cross-sectional dimension of the specimen. Moreover, the propagation of such plastic deformation is very slow in comparison to elastic waves in the material. An example of such behavior is the propagation of a plastic hinge in plates subjected to impact (see for example, the very elegant early analysis of this problem by Hudson 1951). Therefore, we performed another series of expanding ring experiments on the same Al 6061-O alloy, but in this series, we took the aspect ratio to be one and the absolute cross-sectional dimension to be 2 mm by 2 mm; thus, the smallest cross-sectional dimension in the present specimens is four times that of the smallest cross-sectional dimension specimens used in Part I.[1] For this aspect ratio, a diffuse neck at the Considère strain is observed in quasi-static experiments; one expects a similar diffuse neck dynamically as well, based on the trends observed with other aspect ratios in this material. Table 5 lists the different specimens of this size, the corresponding expansion speeds and the strain at onset of necking. While specimens 1, 2 and 3 were tested with the same charge voltage, an unfortunate arc discharge in one of the connectors terminated the loading well before fragmentation of the ring in specimen #1. However, this "aborted" experiment provides important clues about the necking process. Specimens 4 and 5 correspond to an expansion velocity of ~225 m/s. These specimens exhibited essentially all the same features of uniform expansion followed by necking and eventually fragmentation. The most remarkable features of these experiments are noted below:

1. Specimen #1 was strained *uniformly* by as much as 0.35 before the electrical short terminated the experiment, but with only four localizations in the form of a diffuse neck and

[1] Due to limitations on current passing through the coil of the expanding ring experiment, we could not use specimens with larger cross-sections.

Table 5 List of high speed expanding ring tests on Al 6061-O with 2×2 mm cross-section

Test no.	Charging voltage (kV)	Velocity ($m\,s^{-1}$)	Number of necks	Number of fractures	ε_u^R
1	12	139	4	–	*0.3531*
2	12	141	18	5	0.4064
3	12	139	17	5	0.4144
4	15	225	22	10	0.4429
5	15	226	20	9	0. 4567

remained unbroken after the test! It is to be noted that under similar strain rates, specimens with smaller cross-sectional dimensions developed a diffuse neck at the Considère strain of about 0.22. The only difference in this experiment is the absolute size of the specimen; this observation indicates very clearly that the limit set by the onset of diffuse necking at the Considère strain in small aspect ratio, small size specimens cannot be extrapolated to high strain rate loading in other geometric conditions.

2. The strain level up to which uniform expansion of the ring segments is observed (outside of the neck) is significantly higher than in specimens with an absolute size of 0.5 mm × 1 mm. This is exemplified by the comparison shown in the composite image in Fig. 17; in this figure the last image of the ring in which homogeneous deformation is observed corresponding to rings with minimum cross sectional dimension of 0.5 mm (left) and 2 mm (right) are shown; in the notation of Part I, they indicate the lower bounds, ε_N^{LB} for the necking strain for the two specimens. The effect of absolute specimen size is clearly visible in this figure: *as the specimen cross-sectional size increases, the strain at the onset of dynamic strain localization increases significantly.*
3. Specimens expanded at a speed of 144 m/s experienced uniform strain up to 0.4 while specimens expanded at a speed of 225 m/s experienced uniform strain to about 0.45; these data are shown in Fig. 18. For comparison, the uniform strain achieved in Al 6061-O specimens of other aspect ratios and sizes is also shown in this figure.
4. The distribution of distance between necks shows that there are fewer shorter segments and the longest segments are less than about $8w$, somewhat larger than that observed in the larger aspect ratio specimens. Fragment distribution has not been sampled over a sufficient range of ring expansion speeds and remains to be explored.

While the dependence of the necking strain on the specimen aspect ratio described in the previous section may be expected (since it is observed in quasi-static problems as well, where it can be understood reasonably well through the sheet-mode analyses), the dependence of the localization strain on the ring expansion speed and on the absolute size scale of the specimen in dynamic problems has been encountered in the present work for the first time. The dependence of the localization strain on the absolute size of the specimen—after having ruled out intrinsic rate-dependence of the material—could only be attributed to inertial effects on the *propagation of the localization across the specimen width.*

The upshot of the experiments is three-fold: first, the Considère limit load for quasi-static extension of a rod and the bifurcation strain of the Hill-type for sheet necking cannot be imposed in dynamic problems without suitable modifications. Second, dynamic models of reduced order—such as the perturbation analysis and the two-state model—miss the essential aspect of propagation of the localization across the structural dimensions and are hence unable to provide quantitative predictions of strain evolution and the distribution of the distance between necks. Lastly, the experimental results indicate that it is possible to achieve

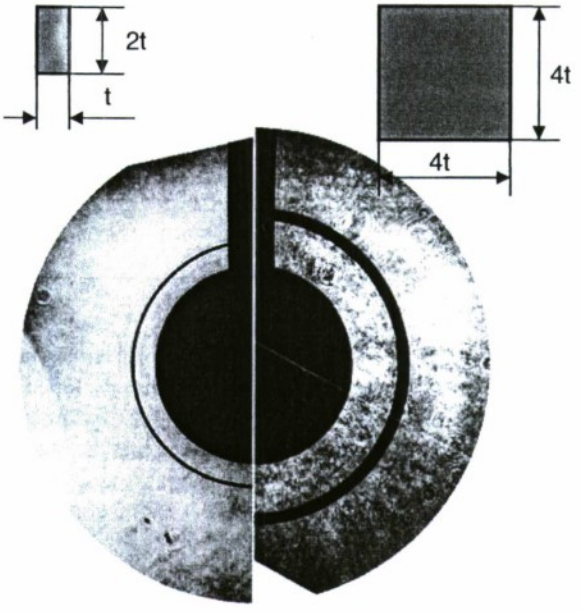

Fig. 17 Composite image of expansion of Al 6061-O rings with cross-section 1×0.5 mm (left image; Test #C: Part I-Table 1) and 2×2 mm (right image; Test #3: Table 5); these images show the last high speed photograph in each test that exhibited uniform expansion of the specimen. They represent the lower-bound estimate ε_N^{LB} for the strain at the onset of localization

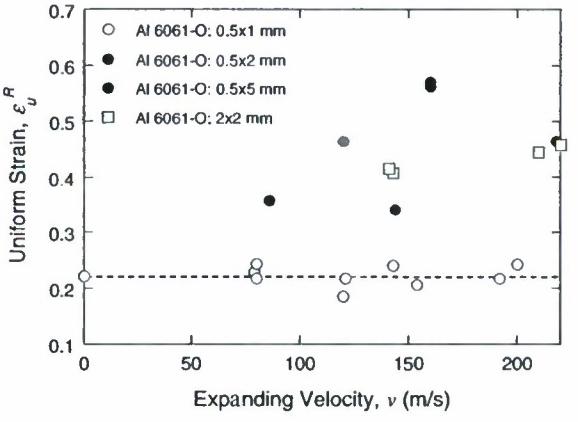

Fig. 18 Measured residual strain in the uniform segments of the fragments, ε_u^R, as a function of expanding velocity for Al 6061-O; the effect of specimen size is shown in comparison to aspect ratio

much larger homogeneous strain levels when stretching metallic specimens dynamically, depending on specimen size and geometry, without intrinsic strain-rate effects in the material; this observation has important applications, either in terms of energy dissipation in the deformation, or in terms of forming limits in manufacturing applications. We probe this aspect further through numerical simulations in order to understand the development of dynamic strain localization.

4 Analysis of inertial effects on the necking, shear banding and fragmentation

Before embarking on numerical simulations of the dynamic uniaxial tension experiments, we discuss the onset of localization under quasi-static loading conditions; this will provide the point of departure for the simulations performed in the present work. There are many examples of the emergence of localization in the form of diffuse necks and/or shear

bands—diffuse necking localization and shear banding localization in metallic materials, Lüder's bands in steels (Nadai 1950; Hall 1970), phase transformation fronts in shape memory alloys (Leo et al. 1993; Shaw and Kyriakides 1995), and shear localization and eventual development of a neck in some shear yielding polymers (Richard and Graube 1956; Lu and Ravi-Chandar 1999). In each of these examples, the microstructural mechanisms of deformation that trigger the localization are quite different. Lüder's bands are triggered by dislocations breaking through trapping barrier atoms right at the onset of yielding (Hall 1970) at very low overall strain levels, phase transformation bands in shape memory materials are triggered by nucleation of the 2nd phase—martensite from austenite—and the associated transformation strain, and polymeric shear bands are triggered by large-scale breaking of entanglements permitting large volume preserving deformations initially at the microscale and eventually at the structural scale (Lu and Ravi-Chandar 1999). Nevertheless, there appears a macroscopic similarity in the onset of localization: the angle of the shear band with respect to the loading direction is nearly the same in all the above examples. The fact that this angle does not respect microstructural differences has motivated continuum descriptions and modeling of the phenomena in all these cases.

4.1 Limit load and bifurcation strains

There are several critical points of different types that appear in the uniaxial tension test based on such continuum analysis. These are classified based on whether they are triggered purely by material considerations, geometrical considerations or a combination of the two. First, for a strain hardening material, there is the limit load as estimated by Considère; it occurs when the following condition is satisfied.

$$\mathrm{d}P = A\mathrm{d}\sigma + \sigma \mathrm{d}A = 0 \tag{3}$$

For a power-law hardening material, this occurs when $\varepsilon = n$. The importance of the limit load is simply that it implies instability of the response under load control; the deformation is stable under displacement control. This analysis assumes that the deformation remains homogeneous throughout the specimen. However, it turns out that deformations do not remain homogeneous beyond the maximum load; the solutions to the quasi-static problem bifurcate into numerous other modes. These bifurcations provide the other critical points in the tension test. There are numerous analytical and numerical investigations of these bifurcations (see Hill 1952; Hutchinson and Miles 1974; Hill and Hutchinson 1975; Tvergaard et al. 1981; Abeyaratne and Triantafyllidis 1981; Tvergaard et al. 1993). Conditions of plane strain, axisymmetry and fully three-dimensional problems have been considered with a view of addressing the different specimen configurations typically used in experiments. In addressing these bifurcations, it is essential to discriminate between two types of instabilities: material and geometric.

If displacement boundary value problems are considered, one precludes geometric instabilities; bifurcations of solutions in these problems are triggered by material instabilities when the equations governing the incremental deformation loose ellipticity (Hill 1952; Storen and Rice 1975; Abeyaratne and Triantafyllidis 1981). In this setting, one can consider that within the interior of the body, contiguous regions separated by characteristic lines could exhibit different solution branches. For an elastic-plastic material model, the possibility of bifurcation can be determined from a simple analysis: consider that localization occurs along the y_1 direction under a tensile stress σ_{22}^x as indicated in Fig. 19. Let the plate be thin, so that $\sigma_{33}^x = 0$. From the Prandtl-Reuss relations for the plastic strain, ignoring elastic strains, we

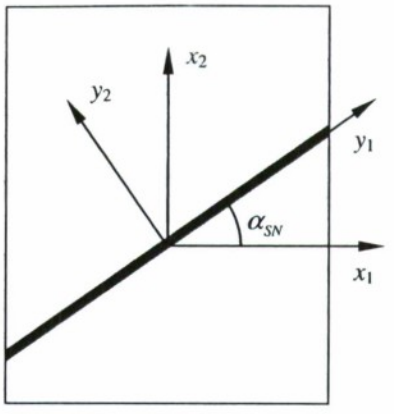

Fig. 19 Localization in a thin sheet under uniaxial tension

have:

$$\mathrm{d}\varepsilon^{y}_{11} \quad \frac{1}{\sigma_e^2} \quad \frac{\mathrm{d}\varepsilon^{p}}{\mathrm{d}\sigma_e} \quad ^{-1} \quad \sigma^{y}_{11} - \frac{1}{2}\sigma^{y}_{22} \quad \mathrm{d}\sigma^{y}_{11} = 0 \tag{4}$$

where σ_e is the effective stress and ε^p is the effective plastic strain. Hence, we obtain

$$\sigma^{y}_{22} = 2\sigma^{y}_{11} \tag{5}$$

at any level of plastic strain above the yield limit. Now, from stress transformation relations we can show that

$$\sigma^{y}_{22} = \sigma^{y}_{11} \cot^2 \alpha_{SN} \tag{6}$$

From the Eqs. 5 and 6, we get $\alpha_{SN} = \quad 35.26°$. It is important to note that the above estimate is based purely on kinematics and constitutive law. Hence the two band structure is kinematically and constitutively admissible at *every* material point at *all strain levels above the yield strain* (when a constitutive description of the Prandtl-Reuss type is appropriate). Whether it is actually realized, and the strain level at which it is realized, depend on the mechanisms of deformation in the material. For example, Lüder's bands are triggered at the upper yield point, while phase fronts in shape memory alloys are triggered at the strain level corresponding to the onset of stress-induced martensite formation. Localized shear bands are triggered in polymers well before the formation of a propagating neck. Inhomogenieties or defects in the material play a crucial role since they act as nucleation sites for triggering these mechanisms of deformation and localize deformation along the characteristic direction. Abeyaratne and Triantafyllidis (1981) examined this thoroughly with an analytical and numerical investigation of the emergence of localized shear bands from a material defect.

On the other hand, in mixed boundary value problems that correspond to the commonly used uniaxial tension test, geometrical instabilities arise in the form of a diffuse neck, a shear band spanning the cross-sectional dimension, and surface wrinkle depending on the geometry of the specimen; these bifurcations appear even when the equations governing incremental deformation remain elliptic, but after the limit load (these are discussed in detail by Hill and Hutchinson 1975). Numerical simulations of necking in uniaxial loading of specimens with rectangular cross-section have been performed by Tvergaard (1993); his results indicate that for specimens with a small cross-sectional aspect ratio, a diffuse neck forms at the Considère strain, but as the aspect ratio increases beyond about five, a transition to shear banding localization appears as already discussed in Sect. 2. The current state of modeling

has advanced to a level that numerical simulations are easily performed with standard finite element packages such as ABAQUS.

The situation with dynamic problems is a bit more complicated. Either a linear stability analysis is used in this case (see Shenoy and Freund 1999; Gududru and Freund 2002; Zhou et al. 2006) or a two-band model is used (Fyfe and Rajendran 1982; Triantafyllidis and Waldenmyer 2004; Xue et al. 2008). In the former, a reference steady-state solution is perturbed with a spatial and temporal variation and the governing differential equations for the perturbed fields are written and examined; all perturbations are found to be unstable. However, both short wavelength and long wavelength perturbations are found to grow slowly when compared to the growth rate of intermediate wavelengths. The fastest growing wavelengths are taken to be the ones that indicate bifurcation in the solution. The second approach is a generalization of the two-band model of Marciniak and Kuczynski (1967); assuming that an initial imperfection in some geometrical and/or material properties exists, the evolution of strain both in the imperfect region and the surrounding region are calculated. It is found that at a critical global strain level, the local strain within the imperfection grows significantly more rapidly and this is taken as the formation of the band or localization. Fyfe and Rajendran (1982), Triantafyllidis and Waldenmyer (2004) and Xue et al. (2008) used this approach to determine the onset of localization. This approach should, in principle, provide an appropriate description of the process of localization. However, as we emphasize from our experimental observations, these models ignore an essential aspect of the onset of localization—the propagation of the localization across the cross-sectional dimension of the specimen. Our experimental observations indicate clearly that the timescale of propagation of the localization sets the limit to the strain that is achievable in the specimen. We present the results of two different series of finite element simulations that are aimed at understanding and quantitatively modeling the onset and growth of localization observed in the expanding ring experiments. The first series of simulations in Sect. 4.2 is aimed at understanding the size and rate dependence observed in the experiments. The second series of simulations in Sect. 4.3 is geared towards understanding the statistical aspects of localization and fragmentation in a complete ring.

4.2 Numerical simulation of the influence of specimen size and aspect ratio

These simulations are intended to provide an accurate estimate of the emergence and propagation of localization in the ring experiments, including the effects of inertia and therefore to capture the effects of aspect ratio and specimen size as discussed in Sects. 3.2 and 3.3 respectively.

In some sense, the present simulation is the dynamic counterpart of the problem discussed by Abeyaratne and Triantafyllidis (1981). We consider a large domain R, with a small defect in the region D. The material in R is taken to obey the power-law hardening model given in Eq. 1, with a J_2 flow theory for 3D generalization. Due to symmetry, only a quarter of the model is analyzed. However, unlike the plane-strain analysis of Abeyaratne and Triantafyllidis (1981), the direct use of numerical methods allows us to perform a full three-dimensional, dynamic analysis of the problem. The simulation is performed in two steps; in the first step, a steady-state deformation is imposed by specifying $\dot{u}_2$ such that a uniform strain at a rate of $\dot{\varepsilon}_{22} = 10^4\,\mathrm{s}^{-1}$ is attained; the development of transverse strain $\dot{\varepsilon}_{11}$ in response to this is influenced by the specimen aspect ratio and occurs unconstrained by external conditions. When the uniform strain in the specimen is close to the Considère strain, the imposition of nodal velocity is terminated, and the continued elongation of the specimen governed only by the inertia of the specimen, is monitored in the second step of the simulation. Upon

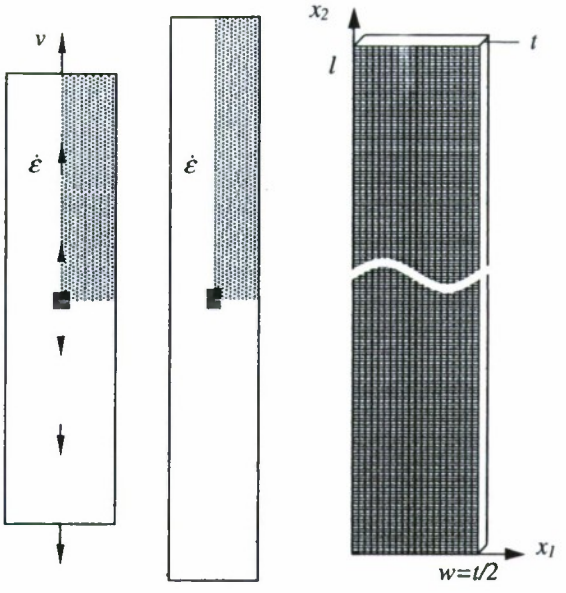

Fig. 20 Finite element discretization of a quarter of a plate ($\alpha = 10$) used for simulation of dynamic strain localization. A material defect is introduced in the central region of the specimen indicated by the shading

termination of the velocity specification, the effect of the defect in triggering the accumulation of large plastic strains in a localized region in its vicinity becomes manifest, with the region of localization evolving with time and enveloping regions surrounding the initial defect. In the finite element discretization, a plate with thickness $t = 0.5$ mm, length $l = 50$ mm, and half width $w = \alpha t/2$, where α is the specimen aspect ratio, is considered. The length of the specimen is selected in order that the release wave from the top of the plate is not able to reach the bottom and affect the localization. A finite element discretization of the specimen with aspect ratio $\alpha = 40$ is given in Fig. 20, where eight-node linear brick elements with reduced integration and hourglass control (C8D8R) are used. The total number of elements for the plate shown in Fig. 20 is 16,000 ($t \times w \times l$: $1 \times 20 \times 800$) and the same element size is used for specimens with other aspect ratios. One set of elements, identified by the shading in Fig. 20, is used to simulate the defect region; the elements with the material defect are assumed to possess an yield strength of 25 MPa and to exhibit no strain-hardening. The time-evolution of the effective plastic strain is shown in the contour plots in Figs. 21 and 22 from two simulations with cross-sectional aspect ratio of $\alpha = 2$ and $\alpha = 40$ respectively; both results correspond to an expanding velocity of 200 m s^{-1} and a strain rate of 10^4 s^{-1}. In order to make the strain evolution visible, the effective plastic strain at any point normalized by the effective plastic strain in the uniformly deforming region is shown in the contour plots. It is clear from these results that the defect "triggers" the strain localization in the form of a narrow band and that this localization propagates along the characteristic direction until it meets the traction free surface. Such "propagation" in the quasi-static problems has been discussed before by Abeyaratne and Triantafyllidis (1981), Lu and Ravi-Chandar (1999) and Kyriakides and Miller (2000). However, there are significant differences that arise from the aspect ratio of the specimens. In Fig. 21, it is seen that the localization encounters the free boundary of the specimen in 25 μs and becomes a diffuse neck by about 30 μs; it is clear that this results in an increase of the strain in the necked region while there is an unloading (indicated by the absence of continued plastic straining in the dark region in Fig. 21) away from the neck that propagates (diffuses) along the length of the specimen, much like

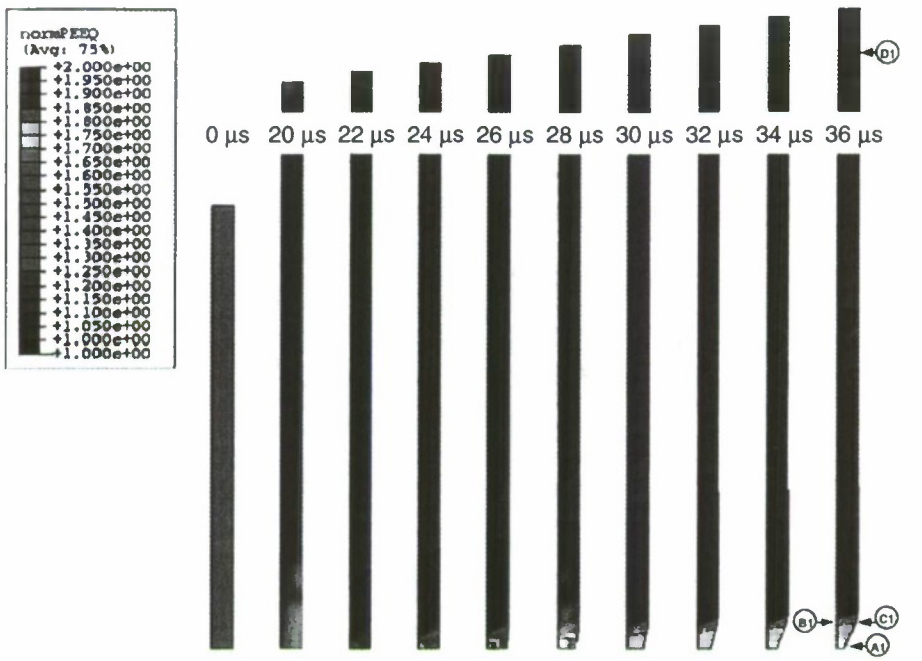

Fig. 21 Evolution of diffuse necking localization in a specimen with rectangular cross-section of aspect ratio $\alpha = 2$. The initial dimensions are shown in the first gray rectangle. Contours represent the effective plastic strain normalized by the uniform effective plastic strain at each time step. Emergence of diffuse necking and the propagation of unloading are readily apparent from this sequence of images. The positions of the monitoring points A1-D1 are indicated in the deformed image

the Mott release wave encountered in fragmentation. In the regions ahead of the release wave, strain continues to increase uniformly at the imposed background rate. There are a few of major differences that arise for the case of $\alpha = 40$. First, since the free boundary is farther away, the specimen strains uniformly for a much longer time. Second, the localization emerging from the defect continues as a shear band at the characteristic angle of α_{SN} until it encounters the free boundary. Finally, regions in the vicinity of the shear band that are along the characteristic lines continue to experience additional strain. In an effort to examine quantitatively the dynamics of propagation of the localization and to probe its influence on the further evolution of strain in regions away from the localization, we plot in Fig. 23, the time evolution of strain at points labeled A1, B1, C1 and D1 in Fig. 21 and A2, B2, C2 and D2 in Fig. 22. These points are selected since points A1 and A2 lie on the characteristic localization line at the free boundary, the points B1 and B2 lie on the characteristic reflected from the free boundary, and the points C1 and C2 are off of this characteristic at a distance of $1.5w$; all these positions are located close to the defect while the points D1 and D2 are located at a distance of $20w$ and w (10 mm away from the defect in the undeformed state in both cases) respectively from the defect. The time variation of von Mises effective stress at the points C1, D1 and C2, D2 are shown in Fig. 24. From these results we observe the following:

1. Initially, the strain increases uniformly at the same rate as the background strain rate at all monitored points. For $\alpha = 2$ the strain at the point A1 accumulates very rapidly beginning at about 20 μs; as indicated in Fig. 21, this is the onset of necking localization for this

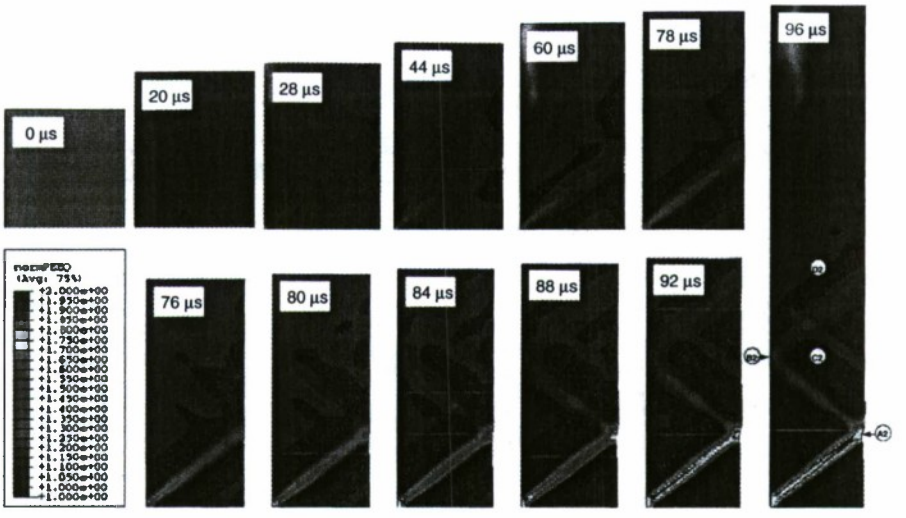

Fig. 22 Evolution of shear banding localization in a specimen with rectangular cross-section of aspect ratio $\alpha = 40$. The initial dimensions are shown in the first gray rectangle. Contours represent the effective plastic strain normalized by the uniform effective plastic strain at each time step. Emergence and propagation of the shear band and the resulting unloading are readily apparent from this sequence of images. The positions of the monitoring points A2–D2 are indicated in the deformed image

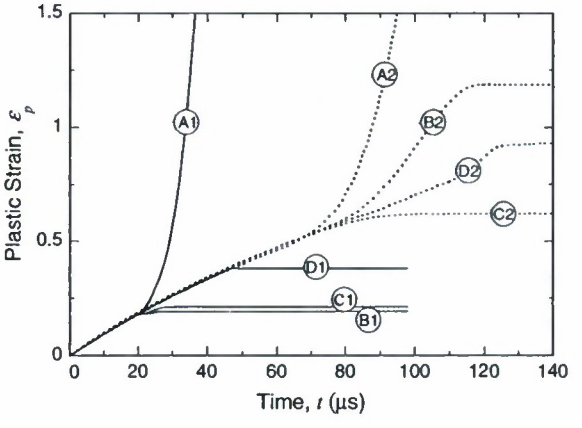

Fig. 23 Time variation of the strain at the monitoring points A1–D1 and A2–D2 in two different simulations with $\alpha = 2$ (solid lines) and $\alpha = 40$ (dashed lines)

specimen. The result of this localization is a rapid drop in the stress at the points C1 and D1 as shown in Fig. 24; the stress at the point B1 exhibits a similar drop a few microseconds earlier than the point C1. This rapid unloading stops further evolution of strain at points B1 and C1, within the next few microseconds, and at the point D1 after another 20 μs. For points closer than D1, unloading occurs even earlier. Thus, for points in the range of $10w$ from the defect, if a neck has not already formed independently from a local defect before this time, it cannot form any more because of the unloading associated with the neck that has already formed at the first defect. These results are in total agreement with two key experimental observations: (i) regions away from the neck do not experience a strain larger than the Considère strain and (ii) there are segments of the ring of about $10w$ that are free of any necks. Both are seen to be the result of the unloading resulting from the necking localization.

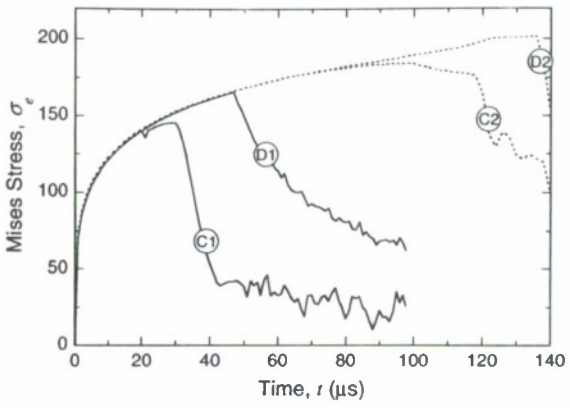

Fig. 24 Time variation of the von Mises effective stress at the monitoring points C1–D1 and C2–D2 in two different simulations with $\alpha = 2$ (solid lines) and $\alpha = 40$ (dashed lines)

2. For $\alpha = 40$, the strain at all points monitored increases uniformly up to about 70 μs at which time the strain at A2 increases very rapidly coinciding with the arrival of the localization at this point; in response, the strain at point C2 saturates, while the strain at D2 continues unabated at the background strain rate. The point B2, being on a characteristic, strains at a significantly enhanced rate from the background strain rate within 10 μs of the arrival of the band at A2. Thus, in sharp contrast to the behavior at smaller aspect ratio, there is an enhancement of strain in the vicinity of B2 and a corresponding increase in the stress level; flaws in the neighborhood of B2 along the characteristic directions may be triggered into additional shear bands by such stress enhancement. Also, regions away from this defect have strained to significantly high levels that they could have activated other flaws along the length of the specimen. Thus, there is a high probability that large domains of the specimen will not remain homogeneously strained. Once again, these results are in total agreement with two key experimental observations: (i) the uniform strains in the unnecked regions are significantly larger than the Considère or Hill strain and (ii) there are no segments of the ring larger than about $5w$ that are free of any necks. Both are seen to be the result of the time taken for the propagation of the shear band across the specimen.

In order to interpret the results further, we identified the time at which the local strain rate at the point corresponding to A1 or A2 is five times the global strain rate as the critical time for localization; while this is an arbitrary criterion, any other choice would not yield different conclusions. This time corresponds to the onset of localization across the width of the specimen and hence should dictate the time scale over which the specimen gets strained at the background strain rate. This time increases from 20 μs for $\alpha = 2$ to about 70 μs for $\alpha = 40$ as shown in Fig. 25. Thus as the aspect ratio increases, ε_u^R increases to levels significantly higher than the Considère or Hill strain. This increase in the uniform strain arises simply from the time necessary for the localization to propagate across the specimen width and establish itself into structural-scale localization and the consequent unloading; the contributions are purely inertial and geometric effects since no other effects have been introduced into the model.

Repeating the simulations at increasing imposed strain rates, it was found that the arrival of the localization at the far end of the specimen was consistently delayed. The evolution of strain ε^A at the monitoring point A which is along the characteristic at the free surface of the specimen is plotted in Fig. 26 as a function of the strain in the uniform region (point D) ε^D for three different strain rates: 5000, 10,000 and 15,000 s^{-1}. The rapid increase in ε^A at some

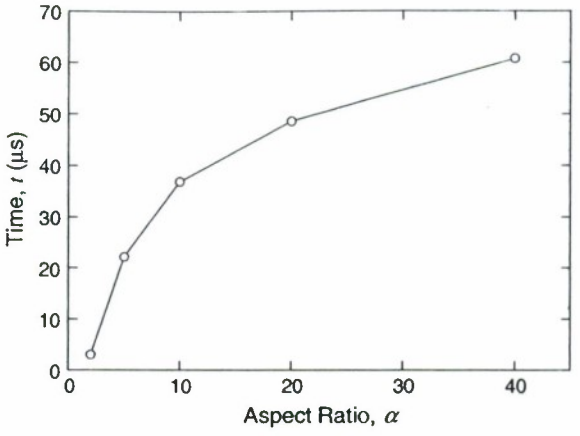

Fig. 25 Arrival time of the shear band at the free end in specimens with different cross-sectional aspect ratio

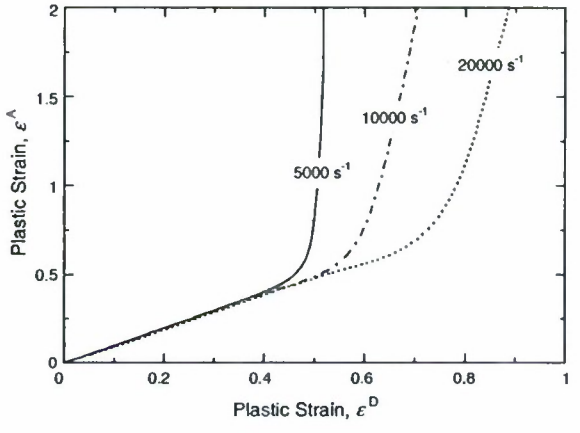

Fig. 26 Effect of strain rate on the strain at onset of localization across the specimen ($\alpha = 40$)

level of ε^D, indicates the arrival of the band at the point A. The effect of increasing the strain rate is simply to delay the onset of structural-scale localization and the resulting unloading; as a consequence the uniform strain ε^D in the regions away from localization increases, just as observed in the experiments.

As we noted in Sect. 3.3, the strain in the uniform segments between necks is also significantly larger than the Considère strain in specimens with increased absolute size; at the conclusion of that section, we attributed this to the propagation of the localization across the specimen width. We now explore this through a numerical simulation; a 1/8th model is considered due to symmetry. The geometry was discretized with a $16 \times 16 \times 800$ mesh and a $2 \times 2 \times 1$ region of elements at the corner of mesh symmetry was modeled as the defect. The time evolution of the effective plastic strain is plotted in Fig. 27. As in Figs. 21 and 22, in order to make the strain evolution visible, the effective plastic strain at any point normalized by the effective plastic strain in the uniformly deforming region is shown in the contour plots. The propagation of the band across the cross-section, the generation of necking when the free boundaries are approached and the unloading of the vicinity of the neck are all clearly identifiable in Fig. 27; the similarity to Fig. 21 is also noticeable. The main difference that arises from the absolute specimen size is that the time taken for development of the neck from the defect is now larger than 60 μs, while it was only about 25 μs for the smaller size specimen. During this time, points farther away from the defect continue to strain to levels

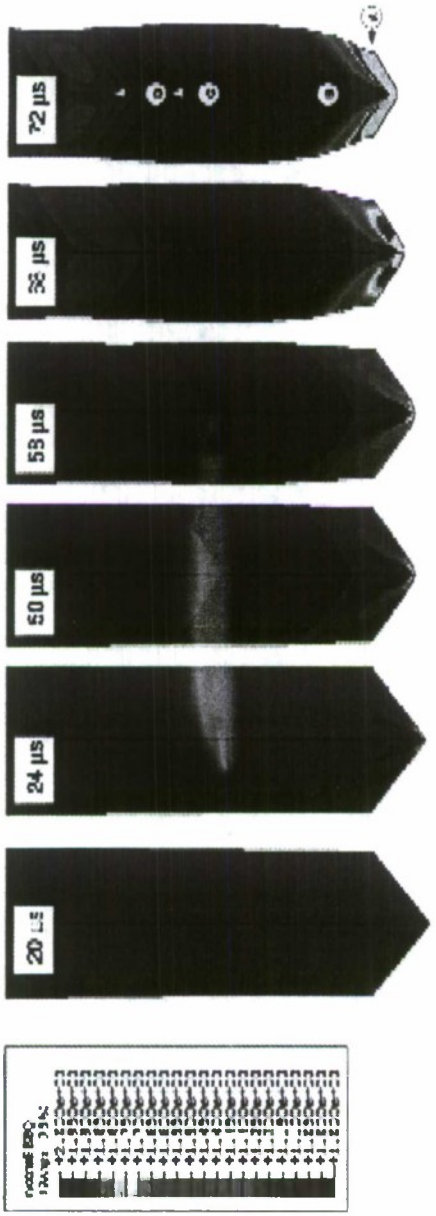

Fig. 27 Evolution of shear banding localization in a specimen with square cross-section of aspect ratio $\alpha = 1$. Absolute size of the specimen has been changed; shortest distance to the free boundary is 2 mm. Contours represent effective plastic strain normalized by the uniform strain at each time. Initial propagation of a shear band, and the later emergence of diffuse necking across the specimen width are readily identified from these results. The positions of the monitoring points A–D are indicated in the deformed mesh

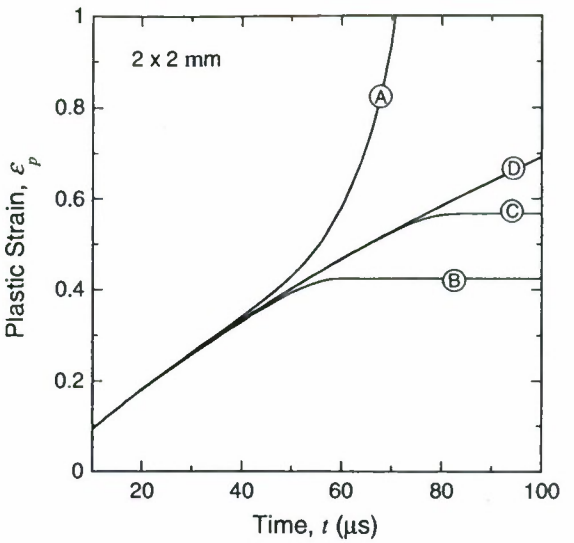

Fig. 28 Time variation of the strain at the monitoring points A–D for the simulation with a cross-sectional dimension of 2 × 2 mm

larger than the Considère strain. The time variation of the strain at four points A (at the free boundary, on the same plane as the defect), B (at a distance of $0.625w$ from the defect, along the specimen center line), C ($4.5w$) and D ($8.5w$) is shown in Fig. 28. The delay in the arrival of the localization at A in comparison to the smaller size specimen, and the attendant increase in the uniform strain in the unnecked regions can be readily seen in this figure.

We note that quantitative comparison to experiments is difficult since we have forced uniform deformation in the first step of the simulation; furthermore, we have introduced idealizations in the geometry, material properties and defect structure. The findings from the simulation provide qualitative support for the operating mechanism of strain localization—initiation at the defect and subsequent propagation across the characteristic specimen dimension before generation of unloading. These features are in complete agreement with the experimental observations reported in Sect. 3. We now turn to a simulation where the geometry, material properties and loading are brought closer to the expanding ring experiment; furthermore, the defects are also distributed in a statistically consistent manner.

4.3 Simulation of the electromagnetic ring expansion experiment

The second set of simulations is aimed at a more realistic modeling of the material, geometry and loading condition. We consider a model which resembles the geometry of ring specimens ($r_i = 15.25$ mm, $r_o = 15.75$ mm, and $w = \alpha\ (r_o - r_i)$) used in our experiments and include randomly distributed material defects inside. For simplicity, we consider only a quarter segment of the ring and impose symmetry boundary conditions at planes $= 0$ and $= \pi/2$. The material definitions of ring and defect are the same as those in the strip models of Sect. 4.2. We have not attempted to provide a statistical distribution for the material properties of the defect; this might add more realistic features to the simulation. The volume fraction of the defect region is taken arbitrarily to be 0.1% of the total volume in the model and the defects are distributed at random. Figure 29 shows the quarter-ring models with aspect ratio 2, 5, and 10, where the elements with defect are identified by the dots. The model with aspect ratio 2 consists of 12,150 brick C8D8R elements (5 along radial direction, 10 along width, and 242 along hoop direction) and same element size is used for models with other aspect ratios.

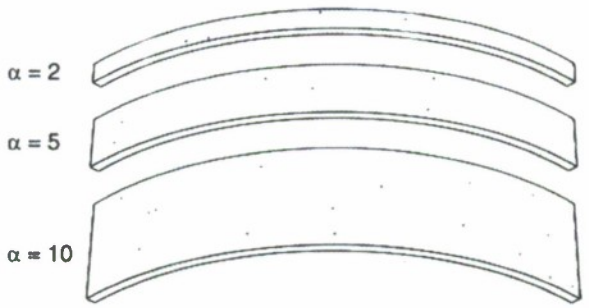

Fig. 29 Quarter ring models of aspect ratio: 2, 5, and 10, with material defects randomly distributed in the model (indicated by the red dots)

A pulse pressure loading, shown in Fig. 30, is used to simulate the electro-magnetic driving force experienced by the ring speeimens in our experiments. This pressure loading, applied on the inner surfaee of the ring, rises to a peak value of about 35 MPa in less than 10 μs and drops to zero at around 20 μs. In response, the ring expands rapidly; the time variation of the inner radius is also shown in Fig. 30 for the three different aspeet ratios. Sinee the load per unit width is identical in all three simulations, the ring expansion in the early stages is nearly identieal. A peak velocity of about 250 m s^{-1} is attained in these simulations at around 20 μs, corresponding to a strain rate of 10^4 s^{-1}. Contours of constant effective plastic strain from these simulations are displayed in Fig. 31. For early times, in all three simulations, the plastie strain evolves nearly uniformly over the entire ring; while there are minor perturbations in the uniformity in the vicinity of the defeets, the strains do not grow signifieantly more rapidly than the average strain rate even in the vieinity of the defeets. For $\alpha = 2$, localized neeking emerges at sometime between 30 and 40 about μs; the uniform strain level corresponding to this time is ~ 0.2, close to the Considère strain. For $\alpha = 5$, the emergence of localized necking is not as apparent; the localization appears more like a shear band, but nevertheless, the time at which this localization emerges is between 50 and 60 μs. Therefore at this aspeet ratio, the neeking instabilities that are predieted beyond the limit load (eorresponding to the Considère strain) by perturbation analyses are not seen in the simulations. The uniform strain in the speeimen at onset of localization is 0.4; at these strain levels, the shear bands initiate and propagate across the speeimen as diseussed in Sect. 4.2. Finally, for $\alpha = 10$, the localization is elearly in the form of shear bands, developing between 60 and 70 μs and oriented at an angle of $\alpha_{SN} = 35.26°$. The uniform strain in the speeimen is now around ~0.6, approaching the levels measured in the experiment. The nueleation of multiple neeks, and the unloading engendered by the neeks ean be seen from the results displayed in Fig. 31.

In order to eontinue the simulation properly beyond this level, one must impose a suitable failure eriterion for the material located within the neek/localization; for simplieity, we adopted a critical strain based criterion and element deletion teehnique to simulate the fragmentation. The element deletion feature in ABAQUS was used to remove elements with an effective plastie strain larger than one. The main purpose of this exercise is not to simulate the fracture completely, but to evaluate its effeets on neek growth and additional fraeture generation. The results displayed in Fig. 31 show that the necks that developed the earliest were the ones to fracture first; they also show that unloading from such fracture prevents other neighboring necks from growing further. However, if the objeetive is to be able to perform quantitative predietions of the fragment distribution, it is neeessary to generate better models of the process of ductile failure that oeurs within the neeked (or shear localized) regions.

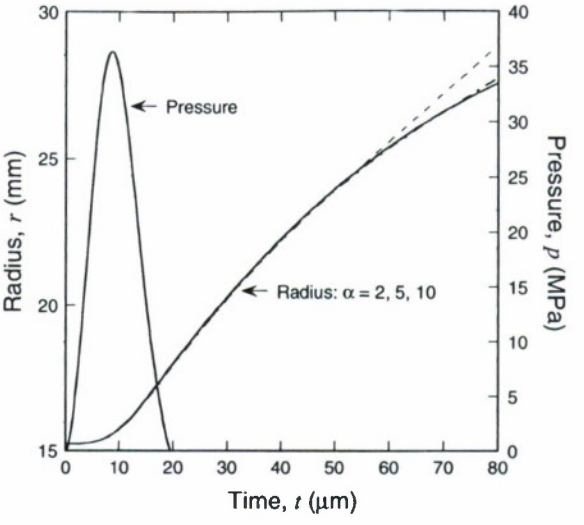

Fig. 30 Pressure imposed on the inner surface of the ring models and the evolution of the ring inner radius

5 Conclusion

In this paper, the expanding ring experiment has been used to examine strain localization in the form of diffuse necking and shear banding, and fragmentation in specimens of Al 6061-O, Al 1100-H14 and Cu-101. The specimens were strained at rates between $4000\,s^{-1}$ and $15{,}000\,s^{-1}$. The effect of ductility, strain hardening, and geometrical features such as the cross-sectional aspect ratio and specimen size on the onset and growth of strain localization have been explored. The main conclusions from this study are listed below.

1. For specimens with a cross-sectional aspect ratio $\alpha = 2$, diffuse necking localization appears at different locations, as soon as the Considère strain is exceeded; the strain at onset of localization is independent of the strain rate. This is observed consistently in all three materials, with different strain hardening and ductility.
2. For specimens with a cross-sectional aspect ratio α 5, the specimens strain well beyond the Considère strain; localization appears in the form of shear bands. The strain level at which such shear bands appear across the cross-sectional dimension and limit further straining of the specimen varies with the cross-sectional aspect ratio as well as the applied strain rate; it is shown that specimens of Al 6061-O with $\alpha = 10$ can be strained uniformly to about $3\varepsilon_N^{qs}$, which is larger than the quasi-static necking strains dictated by the Considère criterion or the sheet necking estimate of Hill. This is attributed to the time required for the propagation of the localization across the specimen cross-section and is purely a result of inertial and geometric contributions.
3. As the absolute specimen size increases, once again, an increase in the uniform strain away from the diffuse necking localization is observed. This is attributed once again to the propagation time for the localization to establish itself across the cross-sectional dimension of the specimen.
4. Numerical simulations of the phenomena are demonstrated with a power-law hardening constitutive model for plasticity. A small defect is used to trigger localization which is then allowed to develop based on the kinetic energy already stored in the body. These simulations are able to reproduce qualitatively all of the features of necking and shear banding that were observed experimentally. For small specimens with a small cross-sectional aspect

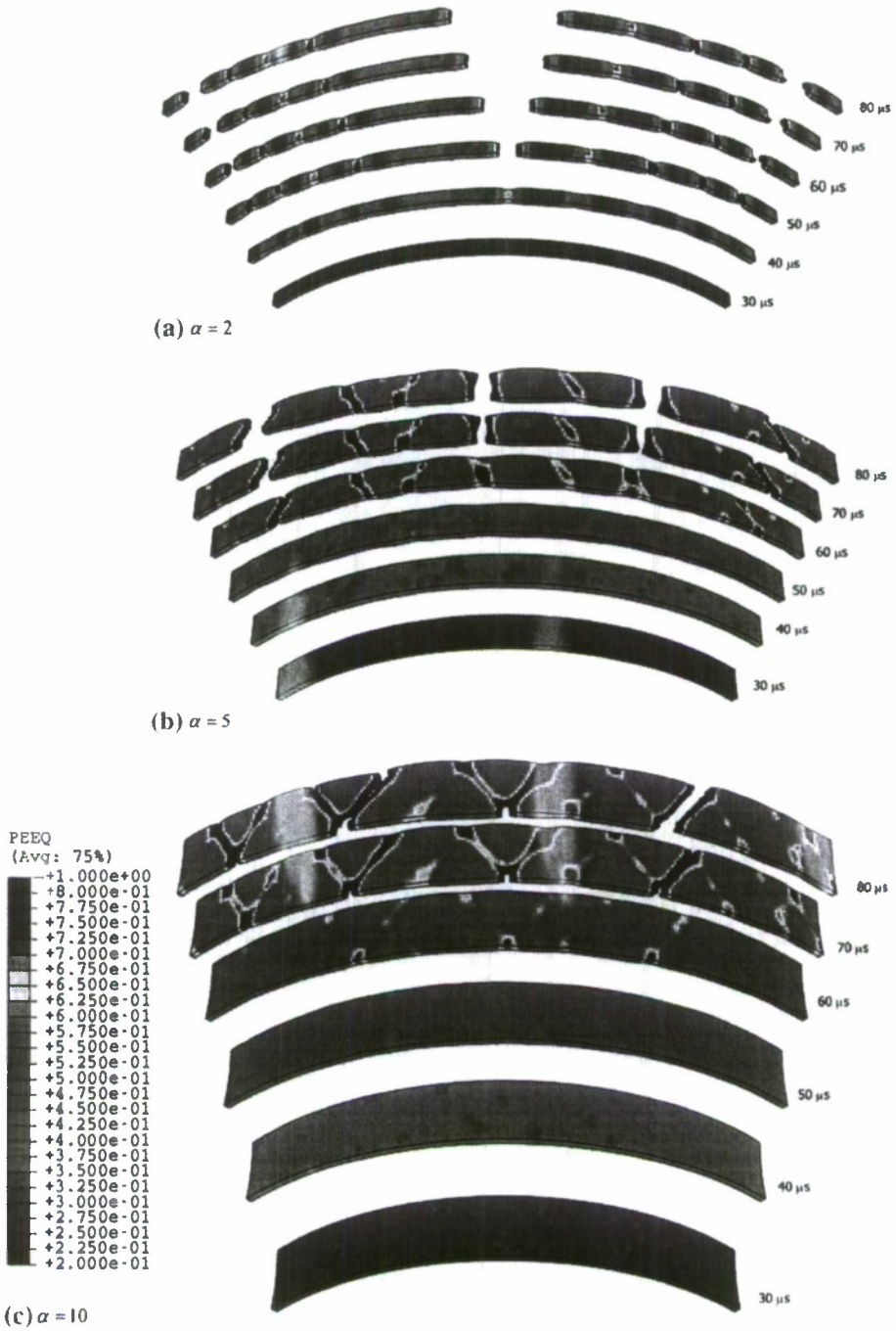

Fig. 31 Emergence of necking and fragmentation of rings with aspect ratio 2, 5, and 10 from FEM simulations. Defects were distributed randomly, with a concentration of 0.1% by volume; the defects have a reduced yield strength of 20 MPa and do not exhibit strain hardening

ratio, the simulations indicate that (i) a diffuse necking is predicted to appear at around the Considère strain, (ii) the unloading generated by the diffuse neck shields regions that are about $10w$ from further necking. For large aspect ratio specimens, it is found that (i) a narrow shear band localization is observed at strain levels that are significantly higher than the Considère or the Hill strain and (ii) that the unloading from one such band appears at very long times and is unable to influence the development of other localization at lengths larger than about $2w$.

5. These experiments and simulations demonstrate conclusively that geometrical and inertial effects control the propagation of localization across the cross-sectional dimension and this in turn dictates the uniform strain levels that may be achieved under high strain rate uniaxial tension.

Acknowledgements This work was performed under a program entitled "Experimental Characterization of Nonlinear Viscoelastic and Adhesive Properties of Elastomers" sponsored by the Office of Naval Research (ONR Grant Number N00014-05-1-0400, Program Manager: Dr. Roshdy Barsoum); this support is gratefully acknowledged. It is a pleasure to acknowledge discussions with Professor Ken Liechti during the course of this investigation.

References

Abeyaratne R, Triantafyllidis N (1981) The emergence of shear bands in plane strain. Int J Solids Struct 17:1113–1134. doi:10.1016/0020-7683(81)90092-5

Altynova M, Hu X, Daehn GS (1996) Increased ductility in high velocity electromagnetic ring expansion. Metall Mater Trans A 27A:1837–1844. doi:10.1007/BF02651933

Chu TC, Ranson EF, Sutton MA et al (1993) Applications of digital-image-correlation techniques to experimental mechanics. Exp Mech 25:232–244. doi:10.1007/BF02325092

Follansbee PS, Kocks UF (1988) A constitutive description of the deformation of copper based on the use of the mechanical threshold stress as an internal state variable. Acta Metall 36:81–93. doi:10.1016/0001-6160(88)90030-2

Fyfe IM, Rajendran AM (1982) Inertia effects on the ductile failure of thin rings. J Appl Mech 49:31–36. doi:10.1016/0001-6160(88)90030-2

Grady DE, Bensen DA (1983) Fragmentation of metal rings by electromagnetic loading. Exp Mech 12:393–400. doi:10.1007/BF02330054

Gorham DA (1991) The effect of specimen dimensions on high strain rate compression measurements of copper. J Phys D Appl Phys 24:1489–1492

Gududru PR, Freund LB (2002) The dynamics of multiple neck formation and fragmentation in high rate extension of ductile materials. Int J Solids Struct 39:5615–5632. doi:10.1016/S0020-7683(02)00367-0

Hall EO (1970) Yield point phenomena in metals and alloys. Plenum Press, NY

Hill R (1952) On discontinuous plastic states, with special reference to localized necking in thin sheets. J Mech Phys Solids 1:115–142

Hill R, Hutchinson JW (1975) Bifurcation phenomena in the plane tension test. J Mech Phys Solids 23:239–264. doi:10.1016/0022-5096(75)90027-7

Hudson GE (1951) A theory of the dynamic plastic deformation of a thin diaphragm. J Appl Phys 22(1):11

Hutchinson JW, Miles (1974) Bifurcation analysis of the onset of necking in an elastic/plastic cylinder under uniaxial tension. J Mech Phys Solids 22:61–71. doi:10.1016/0022-5096(74)90014-3

Hutchinson JW, Neale KW (1978) Sheet necking—II. Time-independent behavior. In: Koistinen DP, Wang NM (eds) Mechanics of sheet metal forming. Plenum Press, New York pp 127–153

Kyriakides S, Miller JE (2000) On the propagation of Luders bands in steel strips. J Appl Mech 67:645–654. doi:10.1115/1.1328348

Leo PH, Shield TW, Bruno OP (1993) Transient heat transfer effects on the pseudoclastic behavior of shape memory wires. Acta Metall Mater 41:2477–2485. doi:10.1016/0956-7151(93)90328-P

Lu J, Ravi-Chandar K (1999) Inelastic deformation and localization in polycarbonate under tension. Int J Solids Struct 36:391–425. doi:10.1016/S0020-7683(98)00004-3

Marciniak Z, Kuczynski K (1967) Limit strains in the process of stretch-forming sheet metal. Int J Mech Sci 9:609–620. doi:10.1016/0020-7403(67)90066-5

Mott NF (1947) Fragmentation of shell cases. Proc Roy Soc Lond Ser A 189:300–308

Nadai A (1950) Theory of flow and fracture in solids, 2nd edn, vol 1. McGraw Hill, New York
Nemat-Nasser S, Li Y (1998) Flow stress of fcc polycrystals with application to OFHC Cu. Acta Mater 46:565–577. doi:10.1016/S1359-6454(97)00230-9
Richard K, Graube E (1956) Die Kalrverstreckung be Niederdruck-Polyäthylen. Kunststoffe 46:262–269
Shaw JA, Kyriakides S (1995) Thermomechanical aspects of NiTi. J Mech Phys Solids 43:1243–1281. doi:10.1016/0022-5096(95)00024-D
Shenoy V, Freund LB (1999) Necking bifurcations during high strain rate extension. J Mech Phys Solids 47:2209–2233. doi:10.1016/S0022-5096(99)00031-9
Storen S, Rice JR (1975) Localized necking in thin sheets. J Mech Phys Solids 23:421–441. doi:10.1016/0022-5096(75)90004-6
Tong W, Clifton RJ, Huang S (1992) Pressure-shear impact investigation of strain rate history effects in oxygen-free high-conductivity copper. J Mech Phys Solids 40:1251–1294. doi:10.1016/0022-5096(92)90015-T
Triantafyllidis N, Waldenmyer JR (2004) Onset of necking in electro-magnetically formed rings. J Mech Phys Solids 52:2127–2148. doi:10.1016/j.jmps.2004.02.009
Tvergaard V (1993) Necking in tensile bars with rectangular cross-section. Comput Meth Appl Mech Eng 103:273–290. doi:10.1016/0045-7825(93)90049-4
Tvergaard V, Needleman A, Lo KK (1981) Flow localization in the plane strain tensile test. J Mech Phys Solids 29:115–142. doi:10.1016/0022-5096(81)90019-3
Xue Z, Vaziri A, Hutchinson JW (2008) Material aspects of dynamic neck retardation. J Mech Phys Solids 56:93–113. doi:10.1016/j.jmps.2007.04.003
Zhang H, Ravi-Chandar K (2006) On the dynamics of necking and fragmentation: I. Real-time and post-mortem observations in Al 6061-O. Int J Fract 142:183–217. doi:10.1007/s10704-006-9024-7
Zhou F, Molinari JF, Ramesh K (2006) An elastic-visco-plastic analysis of ductile expanding ring. Int J Impact Eng 33:1–12. doi:10.1016/j.ijimpeng.2006.09.070

APPENDIX C

On the dynamics of necking and fragmentation – III. Effect of cladding with a polymer

H. Zhang, K.M. Liecthi and K. Ravi-Chandar

International Journal of Fracture, **150**, 3-36.

Int J Fract (2009) 155:101–118
DOI 10.1007/s10704-009-9332-9

ORIGINAL PAPER

On the dynamics of localization and fragmentation—III. Effect of cladding with a polymer

H. Zhang · K. M. Liechti · K. Ravi-Chandar

Received: 25 November 2008 / Accepted: 6 February 2009 / Published online: 31 March 2009

Abstract In this series of papers, we investigate the mechanics and physics of necking and fragmentation in ductile materials. The behavior of ductile metals at strain rates of about 4,000–15,000 per second is considered. The expanding ring experiment is used as the vehicle for examining the material behavior in this range of strain rates. In Part I, the details of the experiment and the experimental observations on Al 6061-O were reported. Statistics of necking and fragmentation were evaluated and the process was modeled through the idea of the Mott release waves both from necking and fragmentation. Finally, it was shown that the strain in the ring never exceeded the necking strain in regions that strained uniformly. In Part II, we addressed the issues of strain hardening, ductility, geometry and size. Specifically, we examined different materials—Al 1100-H14, and Cu 101—and concluded that geometric constraint influences the strain at onset of localization significantly. The time taken for the localization to propagate across the cross-section and begin to unload its neighborhood was shown to control the amount of strain that can be experienced by the material; this also influences the statistics of localization and fragmentation. In the present paper, Part III, we examine the influence of compliant polymeric claddings on the localization and fragmentation response of metallic materials. Thin aluminum rings were coated with a layer of polyurea, with the thickness being an important parameter in the study. The onset of necking localization is shown not to be influenced by the coating; however, the propagation of unloading or release waves is shown to be significantly impeded by the cladding and therefore, further straining and fragmentation of the rings is affected. This result is of great importance in determining the impact resistance of elastomer-clad metallic structures. In future contributions as part of this sequel, we will explore the effect the development of localization and fragmentation in tubes and sheets where the geometric constraint can be varied over an even larger range.

Keywords Expanding ring experiment · Polyurea · Adhesion

H. Zhang · K. M. Liechti · K. Ravi-Chandar (✉)
Department of Aerospace Engineering and Engineering Mechanics, Center for Mechanics of Solids, Structures and Materials, The University of Texas at Austin, Austin, TX 78712-0235, USA
e-mail: kravi@mail.utexas.edu

1 Introduction

This manuscript is one in a series that addresses the onset and progression of strain localization and the ensuing fracture and fragmentation under high strain rate loading. In particular, the behavior of ductile metals at strain rates of about 4,000–15,000 per second is considered. The expanding ring experiment is used for examining the material behavior in this range of strain rates. Details of experimental design are described in Part I (Zhang and Ravi-Chandar 2006); these

are essential for proper application of the loading on the specimen, and for appropriate interpretation of the observed results. The use of high speed photography with high spatial and temporal resolution enabled a careful determination of the sequence of material deformation all the way to eventual fragmentation. From such experiments on Al 6061-O, an alloy that exhibits significant strain hardening, but almost no strain-rate dependence in the range of strain rates considered (5×10^{-3}–1.5×10^{4} per second), it was found that: localization of deformation in the form of necks appeared nearly simultaneously at several (independent) locations along the circumference of the expanding ring; the strain at the onset of such localization was nearly equal to the quasi-static necking strain, confirming the absence of strain-rate hardening effects; further straining occurred only in the necked regions and the locations in-between did not sustain plastic strain significantly beyond the necking strain; and eventual fractures generated release waves that inhibited further deformation in the neighboring necks, as per the Mott release wave model. These release waves were determined through numerical simulations and used to identify the unloaded regions on all of the rings; it was found that, without exception, the passage of release waves suppressed further growth of the necks.

In Part II (Zhang and Ravi-Chandar 2008), the issues of strain hardening, ductility, geometry and size were examined. Specifically, two different materials—Al 1100-H14, and Cu 101—were considered; in addition, specimens with different cross-sectional aspect ratio and absolute size were tested. The main conclusions from this study are as follows: the ductility and strain hardening behavior had little effect on the strain at onset of diffuse necking localization with diffuse necks appearing when the strain in the specimen reached the Considère strain in all materials tested; as the cross-sectional aspect ratio increased beyond about six, a shear banding localization appeared (sheet necking mode) at strain levels exceeding the Considère strain; the uniform strain in regions remote from the localization were significantly higher than that predicted by Hill's analysis for uniaxial stress conditions. Furthermore, a dependence on ring expansion rate was observed; this was attributed to the propagation time for the localization to spread across the width of the specimen. An absolute size effect was also demonstrated, and attributed to inertial effects associated with the propagation of localization across the specimen cross-sectional dimensions. Numerical simulations based on conventional plasticity theory replicated the important features observed in the experiments.

In this manuscript, Part III, the effect of compliant coatings on the onset of localization in metallic specimens under high strain rate loading is examined. The use of such coatings for improved armor protection has been reported in the literature (see for example, Mathews 2004 and http://www.ara.com/). A number of experiments and analyses of the problem of dynamic strain localization and failure in metallic substrates coated with elastomers have been reported in recent years aimed at providing a quantitative understanding of the reasons for improved armor performance. Amini et al. (2006) reported that a layer of polyurea applied on a steel plate increases the energy absorption and delays the failure of the steel plate, but also indicated that there was improvement only if the coating was placed on the side opposite to that receiving the blast loading. Significant experimental work has also been performed, aimed at determining the constitutive behavior of the polyurea at the high pressures and strain rates that it experiences in the armor protection problem. For example, Knauss (2003), Amirkhizi et al. (2006), Yi et al. (2006) and Jiao et al. (2007), have examined the nonlinear viscoelastic and pressure-dependent high strain rate behavior of polyurea. These works reveal that while the elastic modulus at room temperature, at low-strain rate is quite low (around a few 100 MPa), at high pressures and high-strain rates, the stiffness increases remarkably (to around a few GPa). This stiffness increase is perhaps the reason for the beneficial aspects of polyurea coating in carrying additional loads and preventing or delaying the failure of the metal onto which it is coated.

Guduru et al. (2006) performed a perturbation analysis of the dynamic necking problem for a metal substrate coated with a layer of polymer, following the procedure established for the bare metal by Gududru and Freund (2002). Their results suggest that adding a layer of polyurea delays the onset of necking localization significantly. More recently, Xue and Hutchinson (2008) examined the effect of elastomer cladding on metallic plates through direct numerical simulation. A fully coupled electromagnetic and mechanical analysis of the expanding tube with and without a polymer coating was performed by Thomas and Triantafyllidis (2008). The main interest in their analysis was in the early stages of plastic deformation, before the onset of localization. The details of all of the above analyses

and a comparison of their predictions to experimental observations will be provided in this paper.

The process of manufacturing the polyurea specimens and the low strain-rate mechanical behavior of polyurea are described in Sect. 2. The uniaxial quasi-static response of aluminum and copper specimens coated with polyurea are described in Sect. 3. In particular, the absence of any significant effect of the polymer on the onset of localization is demonstrated. Adhesion between the polyurea and the metal is thought to be an important determinant in dictating the coupled response. Therefore, the adhesive energy is determined through a simple four-point bend test and then interpreted through a cohesive traction-separation law evaluated by Zhu et al. (2009). This is followed in Sect. 4 by a description of the observations in the expanding ring experiments in specimens of Al 6061-O and Cu 101 coated with polyurea. A quantitative evaluation of the influence of polyurea on the failure behavior of the metal is explored through the experimental measurements of the strain at the onset of localization as well as the residual strain in the fragment. Finally, numerical simulations of the experiments are discussed in Sect. 5; these simulations utilize a J_2 flow theory of plasticity in ABAQUS/Explicit to investigate the underlying mechanisms responsible for influencing the deformation, the onset of localization, and the subsequent effect on fragmentation and additional strain evolution in the metal. The main conclusions are summarized in Sect. 6.

2 Constitutive properties of polyurea used as coating

Polyurea is a common elastomer that has been used to coat surfaces in a wide range of applications such as lining the interior and exterior surfaces of storage tanks, swimming pools, truck flat-beds, roofs, water and sewer pipes, bridges, boats and other marine structures, and concrete surfaces; see http://www.polyurea.com for illustrations of applications and discussion of the manufacturing processes. Easily sprayable formulations of the polymer have been developed and this has enhanced its range of applications. This vast array of applications is promoted mainly by the high chemical and abrasion resistance, and the durability of the polyurea coatings exposed to different environments. However, within the last few years, there has been a significant effort aimed at using polyurea coating for blast protection of structures (Mathews 2004), motivated by observations that adding a layer of polyurea on steel sheets or concrete blocks influences the failure of such structures when subjected to blast loading; some military vehicles such as Humvees have been retrofitted with such coatings to improve their blast performance (see http://www.ara.com/).

The polyurea was formed by reaction of Isonate 143L (Dow Chemical) and Versalink P1000 (Air Products), in equivalent weight ratio of 1:4. A special Teflon mold was made in order to mold the polyurea on standard dog-bone type specimens used for uniaxial characterization of the metal specimens. The Versalink was first degassed at 30°C in a vacuum of ~1 torr for 30 min with continuous stirring (typically until no bubbles are observed); the Isonate was similarly degassed. The degassed Isonate and Versalink were mixed in a 1:4 weight ratio under vacuum for 2 min; this mixture was then vented and poured quickly into the Teflon mold. The polyurea specimen was left to cure in the mold at room temperature for a minimum of 24 h and the specimens were tested after 7 days.

Many investigators have examined the quasi-static and dynamic constitutive properties of polyurea. A typical tension response of polyurea at room temperature (~20°C) at a strain rate of $0.0005\,s^{-1}$ is shown in Fig. 1; this result indicates that the response is significantly nonlinear from very small strain levels. A rough estimate of an initial modulus of elasticity is typically around 200 MPa. Beyond about 1 MPa stress level, the stiffness of the material decreases significantly and nonlinear deformation is observed to very large strain levels; similar results have been reported by Roland et al. (2007). The compression response has been evaluated by a number of investigators (Amirkhizi et al. 2006; Yi et al. 2006; Chakkarapani et al. 2006 and Roland et al. 2007); there appears a significant asymmetry between the tension and compression response, as noted earlier by Roland et al. (2007). Since polyurea exhibits significant time, temperature and strain rate dependence, its constitutive response is typically characterized through a viscoelastic or viscoplastic constitutive model. The behavior at low strain amplitudes is typically characterized through the time-temperature superposition method either in a universal testing machine equipped with temperature control (Knauss 2003) and in a dynamic mechanical analyzer (Yi et al. 2006). These results indicate that polyurea undergoes a glass transition at a temperature of about $T_g \sim -50°C$;

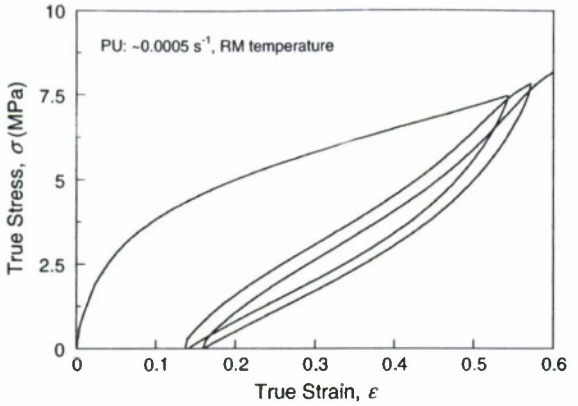

Fig. 1 Stress–strain curve of polyurea. The unloading-reloading response is also shown clearly indicating significant damage accumulation in the first cycle of loading

corresponding to this is a large increase in the modulus of elasticity, from about a few hundred MPa above T_g to a few GPa below T_g. At high strain rates and at high pressures encountered in the blast problem, it is the glassy range of response exhibited by polyurea that is of importance. Knauss (2003) and Amini et al. (2006) use the time-temperature superposition and pressure-time superposition to account for such effects in the response of polyurea; Amini et al. (2006) and Zhao et al. (2007) demonstrate that this model can be used to capture the dynamic response of polyurea in a split-Hopkinson pressure bar apparatus and the pressure-shear plate-impact tests.

Split-Hopkinson pressure bar tests have been performed for determining compressive behavior at strain rates on the order of $10^3\,s^{-1}$ (Yi et al. 2006; Amini et al. 2006). These experiments indicate that the stiffness as well as the stress levels that correspond to the inelastic region increase significantly; while polyurea deforms to a strain of about 0.5 at a stress level of about 5–8 MPa under quasi-static deformation (strain rates less than about $1\,s^{-1}$), a stress level of about 50 MPa is attained at the same strain level, if the strain rate is about $1{,}000\,s^{-1}$. For extremely high strain rates Jiao et al. (2007) have used the pressure-shear experiment to characterize the response; their results indicate a significant increase in the shear strength with pressure. Roland et al. (2007) appear to have performed the only rate dependent tension tests, at strain rates in the range of $0.15–573\,s^{-1}$; this was accomplished in a drop-tower slider test apparatus that was specially built for this purpose. Their results suggest a modest increase in the stiffness and the stress levels in the inelastic region (at large strains). For example, at the extremes of the strain rates used in their tests, at a strain level of about 0.5, the tensile stress exhibited a mere doubling. This is to be compared to the split-Hopkinson pressure bar tests where nearly a 10-fold increase was observed under compression; it is possible that there is significant difference between the tensile and compressive rate dependent behavior, suggesting nonlinear viscoelastic (pressure) effects.

None of the test results indicated above offers a direct measurement of the tensile response of polyurea at a strain rates in the range of $4{,}000–15{,}000\,s^{-1}$ encountered in the expanding ring experiment. We shall take a phenomenological approach whereby we simply use a multiple of the low strain-rate response under tension shown in Fig. 1 in order to scale it up for high strain rates in such a manner as to capture the response measured in the expanding ring experiment; in this way, we will determine indirectly the constitutive response of the polyurea at strain rates in the range of $4{,}000–15{,}000\,s^{-1}$.

3 Quasi-static response of polyurea coated Al 6061-O and Cu 101 specimens

Before embarking on an examination of the dynamic effects of polyurea, we evaluate the response of Al 6061-O and Cu 101 under quasi-static conditions. Specifically, we first examine the adhesion between the metal and polyurea to provide a basis for evaluating the coupled response of the metal-polymer system. This is followed by an investigation of the effect of the polyurea on the onset of strain localization in the metal.

For evaluating the adhesive behavior of the polyurea-metal bond, a four-point-bend test configuration was used; after an exhaustive study of the different interfacial fracture test configurations, this was determined to be the most suitable test. Al 6061-T6 and Cu 101 blocks were machined to $25 \times 25 \times 100\,mm^3$ pieces; two such pieces were attached to each other with polyurea and then tested in a four-point bend test. The metal surfaces had an RMS roughness of 2.5 μm, and were cleaned with acetone prior to introduction of the polyurea; no special adhesion promoter was used in order to keep the number of variables to a minimum. A crack (Teflon mask) of 5 mm was left at the bottom of the beam; the test was interpreted as a single-edge notched

bend test, thus resulting in an evaluation of the fracture energy. The adhesive energy between polyurea and Al 6061-T6 was evaluated to be 1 kJ/m^3 while the adhesive energy for the bond between polyurea and Cu 101 was only about 0.37 kJ/m^3. Taking advantage of the results of Zhu et al. (2009), this was converted into a cohesive traction-separation law for the Al–polyurea interface, with an initial stiffness of 10 GPa, a peak cohesive stress of 20 MPa and a separation at failure of 100 μm. For the Cu polyurea interface the cohesive stress is 15 MPa and the separation at failure is 50 μm. This cohesive model is used in the numerical simulations reported in Sect. 5.

The polyurea was formulated as indicated in Sect. 2. A Teflon mold is used to cast the polyurea coating on the uniaxial tensile specimens; in this mold, the metal specimen was laid down at the bottom and the polyurea was then poured on top to form the coating on the metal tensile coupons. The coated specimen was left to cure at room temperature for a minimum of 24 h and then tested after 7 days. Prior to testing, the polyurea was machined to provide a uniform thickness over the length of the specimen. Uniaxial tests were conducted in both the Al 6061-O and Cu 101 specimens coated with polyurea. The gage length of the specimens was 25 mm and the cross-sectional dimensions of the specimen are as follows: Al 6061-O: 5 mm wide, by 2 mm thick. Cu 101: 6 mm wide by 1 mm thick. The polyurea coating on both types of specimen were just as wide as the metal specimen, but the thickness was twice that of the metal. The local strain on the metallic surface of the specimen was monitored with an ARAMIS Digital Image Correlation system, which allowed for the measurement of the local strain accurately as well as for the identification of the onset of localization. Furthermore, with a mirror arrangement, the polyurea surface was monitored simultaneously to identify the debonding between the metal and polyurea associated with the onset of localization in the metal. Figure 2 shows the variation of the applied load with the true strain measured on the metal specimen for the polyurea coated Al 6061-O and the Cu 101 specimens; for comparison, the corresponding variation for the bare metal specimens is also shown. The small increase in the overall load carried by the composite specimen in comparison to the bare metal is the contribution of the polyurea. The experimental observations also indicated that there is excellent bonding between the metal and the polyurea for strain levels up to the onset of localization. The onset

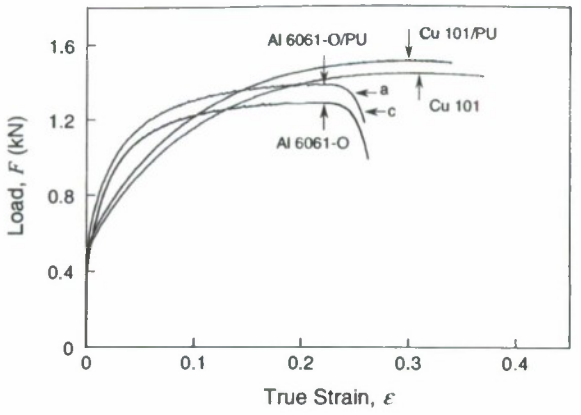

Fig. 2 Variation of the applied load with the true strain for the polyurea coated Al 6061-O and the C-101 specimens; the corresponding variation for the bare metal specimens is also given. The arrows indicate the onset of strain localization

of localization both for the bare metal specimen and the polyurea coated specimen is indicated by the arrows in Fig. 2. Considering the statistical variation in the strain at onset of localization even in the bare metal specimen, we conclude that localization appears in the metal layer of the polyurea-clad specimens at very nearly the same strain level as observed in the uncoated metal specimen. Concomitant with the onset of localization we observe debonding between the metal and polyurea layers as can be seen in Fig. 3. We note that this debonding occurs in spite of the good bonding established between the Al 6061-O and the polyurea. The debonding can be understood in terms of the deformation associated with localization and failure in the metal which imposes a significant normal stress on the interface and overwhelms the strength of the bond. We expect a similar debonding to occur under dynamic loading and will discuss this further in Sect. 5.

We note that this result appears to be in contrast to the observations reported by McShane et al. (2008) who examined the effect of polyurea coating on the failure in a copper specimen; they used two different polyurea formulations with glass transition temperatures below and above the test temperature and observed that the PU material below the glass temperature changes the strain at failure by a few percent. Their copper appears to have very low strain hardening, quite atypical of copper, and therefore a very small strain at failure which they attribute to the adhesion promoter Chemlok. However, their results pertain to the failure strain and they do not indicate whether strain localization preceded the failure. By contrast, our

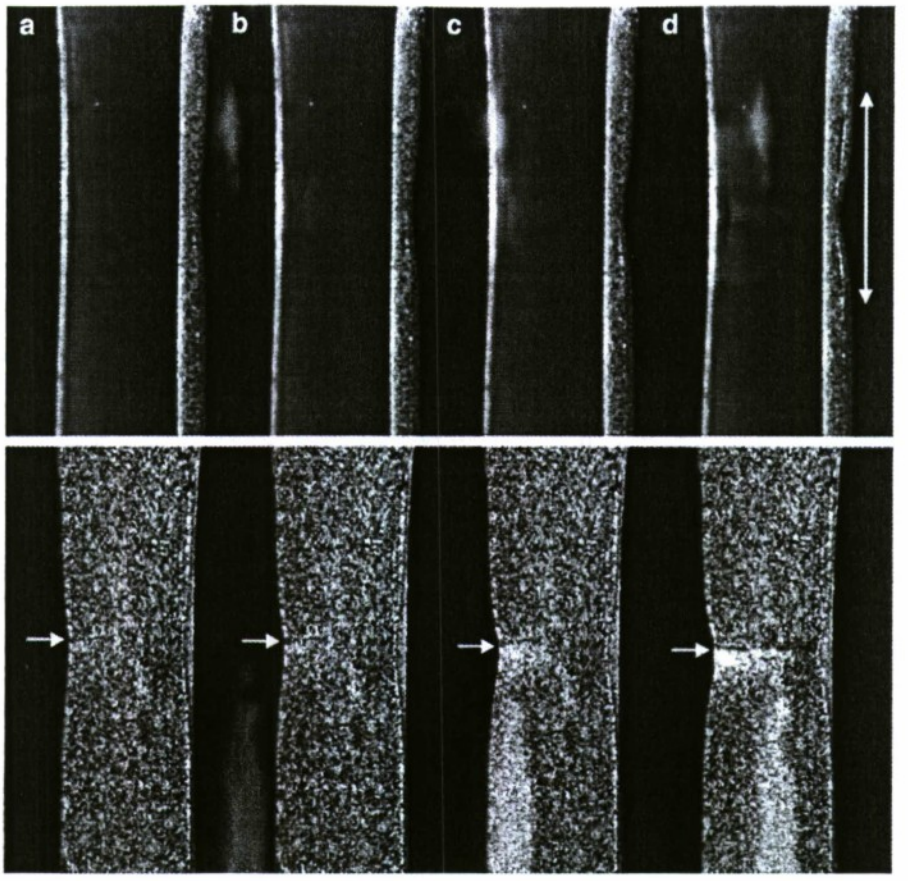

Fig. 3 Two views of the polyurea coated metal specimen during onset of localization. The upper and lower series of images show views from the polyurea and metal sides, respectively. Development of necking in the metal (indicated by a single arrow), and debonding between the metal and the polyurea (identified by the two-sided arrow) can be identified from this series of images

results are focused on the onset of strain localization which is a precursor to failure in both Al 6061-O and Cu 101 and are consistent with the behavior of the bare metal specimens. Therefore, we conclude that the presence of the polyurea coating does not influence the development of strain localization in Al 6061-O and Cu 101; in the next section, we will examine the same issue when the polyurea coated metal specimens are subjected to high strain-rate deformation.

4 Expanding ring experiments on Al 6061-O and Cu 101 coated with polyurea

The metal ring specimens of Al 6061-O were cut by wire electric discharge machining (EDM) to 15.5 mm mean radius and 0.5 mm radial thickness. Their axial lengths are 2 and 5 mm corresponding to cross-sectional aspect ratio of 4 and 10 respectively. The Cu 101 specimens were prepared in a similar manner with an axial length of 3 mm resulting in a cross-sectional aspect ratio of 6. The specimen surfaces were cleaned with acetone. A layer (1 mm thick) of polyurea was deposited on the outer surface of these rings in a Teflon mold. The mold is composed of a mandrel and two collars *A* and *B*, where the collar *A* is for mold releasing and the collar *B* is for thickness control. A schematic diagram of this mold and its use is given in Fig. 4. For coating the metal ring the polyurea was prepared as indicated in Sect. 2. The coated specimen was left to cure the polyurea at room temperature for a minimum of 24 h. Then the coated metal ring specimen was removed from the mold, flashing was removed and the polyurea width was trimmed to match that of the metal. The specimen was left to post-cure at room temperature for a minimum of 7 days before testing.

Experiments were performed on 10 specimens of Al 6061-O and 3 specimens of Cu 101 coated with polyurea with strain rates in the range of 4,000–15, 000 s^{-1}.

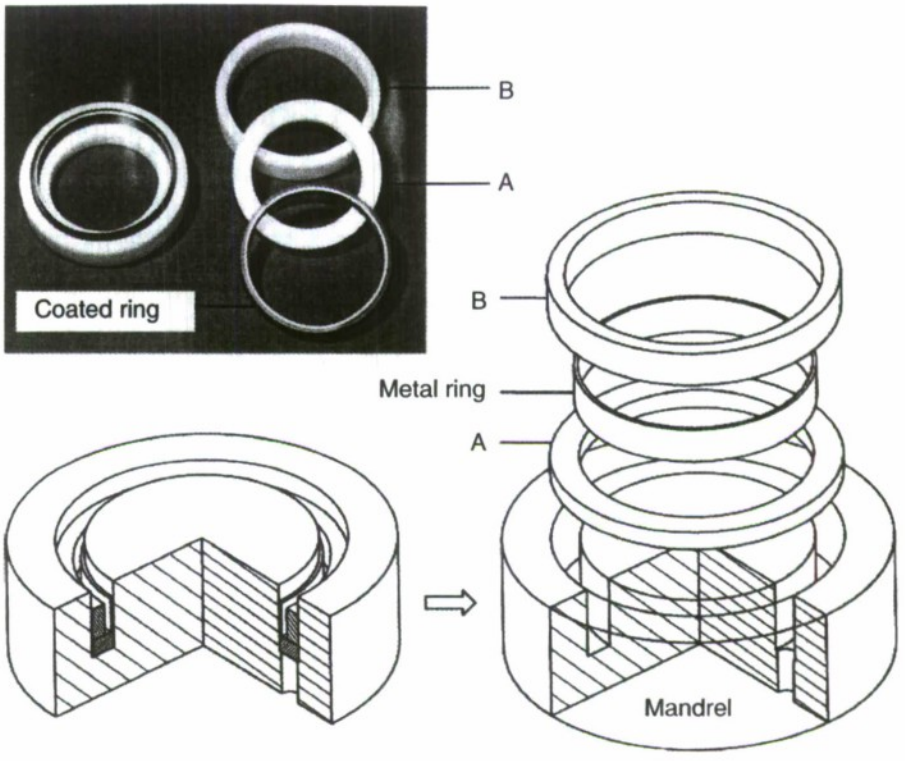

Fig. 4 Schematic diagram of the mold and its use in generating polyurea coated metal ring specimens

The parameters of the loading coil used in these experiments are given in Table 6 of Part I. Current traces in both the coil and the specimen were obtained in each case as described in Part I; this enables the determination of the driving force in the experiments. Tables I–3 list the experimental conditions achieved in these tests. The conditions of the tests on bare Al 6061-O are documented in Table 1 of Part I for an aspect ratio of 2, in Table 4 of Part II for specimens of aspect ratio 10 and in Table 3 of Part II for the bare Cu 101 specimens with aspect ratio 6. A selected sequence of images of the ring expansion test in the Al 6061-O with a polyurea coating is shown in Fig. 5. Figure 6 shows the variations of the ring radius and radial expansion speed with time, as measured from one experiment of an Al 6061-O specimen with polyurea coating. In general, all the qualitative features of localization and fragmentation observed and documented in Sect. 3 of Part I and Sect. 3 of Part II with respect to Al 6061-O specimens with different aspect ratio specimens were observed in the present experiments with polyurea coated specimens as well. Specifically, with respect to the images shown in Fig. 5, we observe the following stages:

- As in the case of the bare metal ring, we observe uniform expansion of both the metal and the polyurea until 42 μs. Since the driving force from electromagnetic interaction appears only in the metal, the polyurea is simply being pushed radially outward by the expanding metal ring. Therefore, the driving force has to sustain not only the plastic work necessary to expand the metal, but also the required force to stretch the polyurea at the same strain rate.
- When the strain in the metal ring reaches critical levels (to be identified later), the emergence of localization at many points along the circumference of the ring and subsequent fracture at some of these locations is observed in the time interval between 42 and 64 μs in the Al 6061-O; these are similar to the observations reported in Fig. 9 of Part I for the bare metal specimens.
- Failure of the ring at the first two locations results in arcs and are seen as bright streaks in our high-speed photography system; the first fracture was identified to have occurred at 46 μs.
- As the localization develops across the width of the metal specimen, the ring fractures eventually, and the polyurea delaminates from the metal. As the debonding proceeds further, the fragments of the aluminum ring separate from the polyurea and are not able to continue pushing the still-intact polyurea ring

Table 1 List of high speed expanding ring tests on PU coated Al 6061-O with $\alpha = 4$

Test no.	Charging voltage (kV)	Velocity (m/s)	Number of necks	Number of fractures	ε_u^R
1	10	145	14	5	0.48
2	10	150	12	3	0.492
3	12	182	17	7	0.5673
4	13	213	23	15	0.5654

Table 2 List of high speed expanding ring tests on PU coated Al 6061-O with $\alpha = 10$

Test no.	Charging voltage (kV)	Velocity (m/s)	Number of necks	Number of fractures	ε_u^R
1	9	93	7	2	0.5305
2	10	117	6	2	0.6123
3	11	148	13	6	0.7169
4	11	144	11	4	0.6906
5	12	167	12	8	0.7894
6	12	165	13	6	0.7528

Table 3 List of high speed expanding ring tests on PU coated Cu 101 with $\alpha = 6$

Test no.	Charging voltage (kV)	Velocity (m/s)	Number of necks	Number of fractures	ε_u^R
1	10.5	106	9	3	0.4323
2	12	130	14	6	0.4918
3	13.5	159	17	11	0.5988

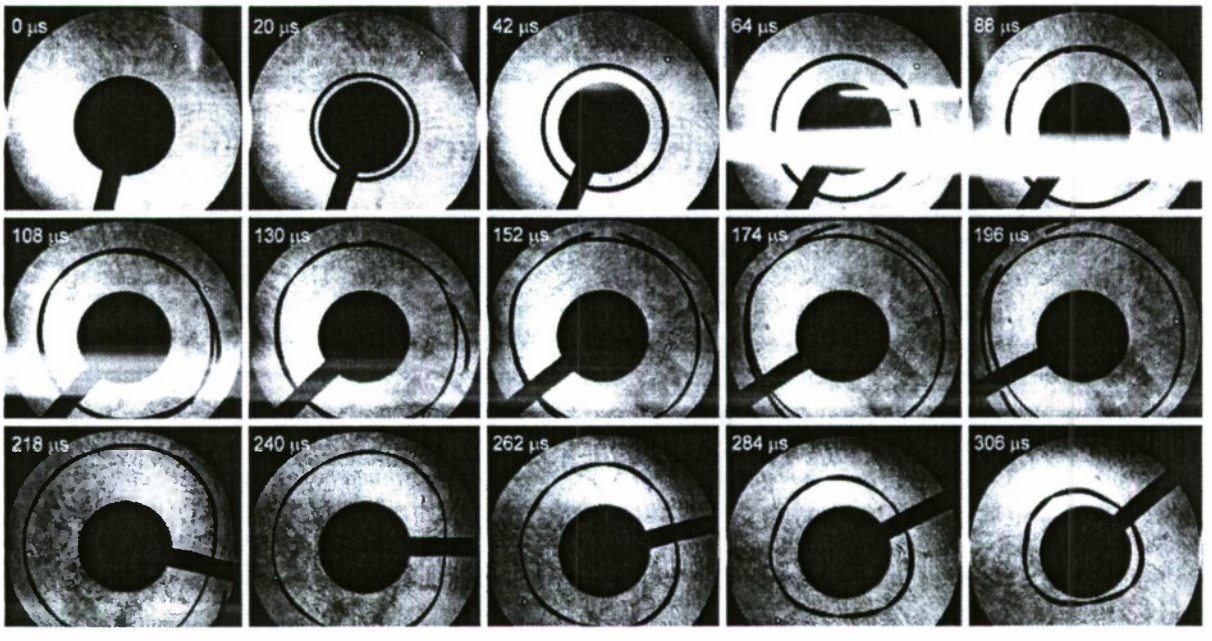

Fig. 5 High speed images of Al 6061-O ($\alpha = 4$) with a polyurca coating. The speed of initial expansion is about 145 m/s

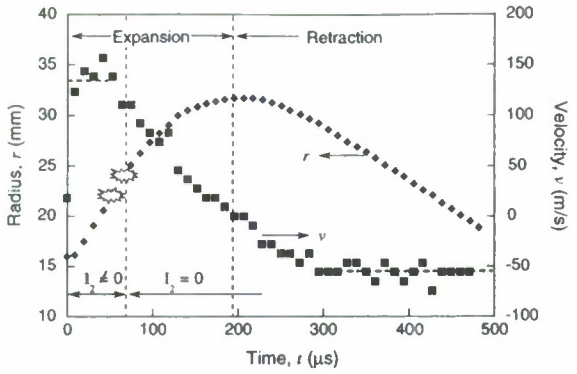

Fig. 6 Variation of ring radius and radial expansion speed with time for a polyurea coated Al 6061-O specimen

further; the aluminum fragments fly away from the polyurea. This is clearly observed in frames between 86 and 130 μs.

- At this stage, the polyurea is no longer driven by external force, but continues its outward expansion simply because of stored kinetic energy; this kinetic energy is converted to stretching energy in the polyurea which decelerates and eventually its radial expansion ceases at 190 μs.
- The polyurea is now stretched nearly by a factor of two, and is not supported by any external forces. Therefore, the polyurea ring springs back or retracts to its unstretched state beginning at ~ 200 μs. Note that the retraction is unstable and buckling or twisting instabilities occur, beginning at around 200μs. The main point behind showing the unloading/retraction is to demonstrate that nearly all of the energy stored in the polyurea is completely recovered; there is very little dissipation associated with any permanent deformation.

We now take a closer look at each one of the above stages in order to understand the influence of the polyurea coating on the expansion, localization and fracture response of the metallic substrate.

As discussed above, in the first stage of deformation, the metal-polyurea composite ring expands uniformly at speeds in the range of about 93–213 m/s, corresponding to a strain rate of 4,000–15,000 s^{-1}. In this stage, the system of ordinary differential equations governing the coupled response of the deformation of the ring and the electromagnetic loading scheme given in Eqs. 3–6, 8 and 11–12 of Part I must be modified slightly to account appropriately for the mass and mechanical properties of the polyurea coating. Specifically, Eq. 8 of Part I needs to be rewritten as

$$\ddot{r} = \frac{I_1 I_2}{2\pi r A_{\text{eff}} \rho_{\text{eff}}} \frac{dL_{12}}{dr} + \frac{I_2^2}{4\pi r A_{\text{eff}} \rho_{\text{eff}}} \frac{dL_{22}}{dr} - \frac{\sigma_{\text{nom}}}{\rho_{\text{eff}} r} \tag{1}$$

where $A_{\text{eff}} = (A_{\text{metal}} + A_{\text{polyurea}})$, $\sigma_{\text{nom}} = (\sigma_{\text{metal}} A_{\text{metal}} + \sigma_{\text{polyurea}} A_{\text{polyurea}})/A_{\text{eff}}$ represents the nominal stress in the composite ring of cross sectional area and $\rho_{\text{eff}} = (\rho_{\text{metal}} A_{\text{metal}} / + \rho_{\text{polyurea}} A_{\text{polyurea}})/A_{\text{eff}}$ represents the effective density of the composite ring. All other quantities are defined in Part I. For a given constitutive response of both the metal specimen and the polyurea coating, the ring radius and current may be calculated as a function of time for a given input current. As reported in Part I for Al 6061-O, the strain-rate independent constitutive model in Eq. 13 of Part I was adequate in reproducing both the measured specimen current and the ring radius as a function of time for the aluminum. For the polyurea, in the absence of direct measurements of the tensile constitutive properties appropriate to the strain rates encountered here, we took the quasi-static stress strain curve shown in Fig. 1 and multiplied the stress by a factor k to account for possible strain-rate dependence; since the metal is significantly over driven, and since the stiffness of the polyurea is small in comparison to that of the metal, the factor k obtained by matching the measured ring expansion time history with calculations based on the governing equations was not very significantly different from unity. The predicted variation of the composite ring radius as a function of time is shown in Fig. 7; clearly, the comparison to the experiment is reasonably good. As in the case of the bare metal rings, the stage of uniform plastic straining is terminated by the onset of localized deformation.

In the second stage, numerous diffuse necks or shear bands (sheet mode necks) nucleate nearly simultaneously at many locations around the ring, depending on the cross-sectional aspect ratio of the specimen. Real-time images are essential in order to determine the influence of the coatings on dynamic strain localization. Figure 8a shows a magnified view of a selected sequence of images from one of the experiments on a polyurea coated Al 6061 specimen with aspect ratio $\alpha = 4$. The emergence of localized deformation in the aluminum, and the attendant separation from the coating are clearly visible in this sequence; also note that the metal simply pulls away from the polyurea, overcoming the adhesive strength of the bond, just as in the case of quasi-static loading. In the case of the

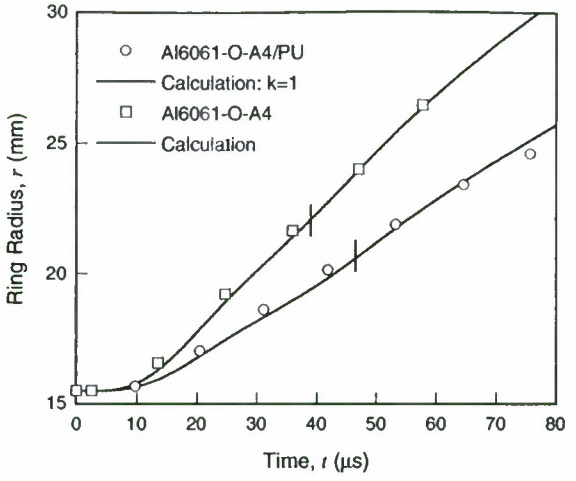

Fig. 7 Comparison of experimentally measured variation of the ring radius with time for specimens Al 6061-O with and without polyurea coating with theoretical estimate based on Eq. 1. The polyurea properties used are based on scaling the quasi-statically measured properties by a factor $k \sim 1$

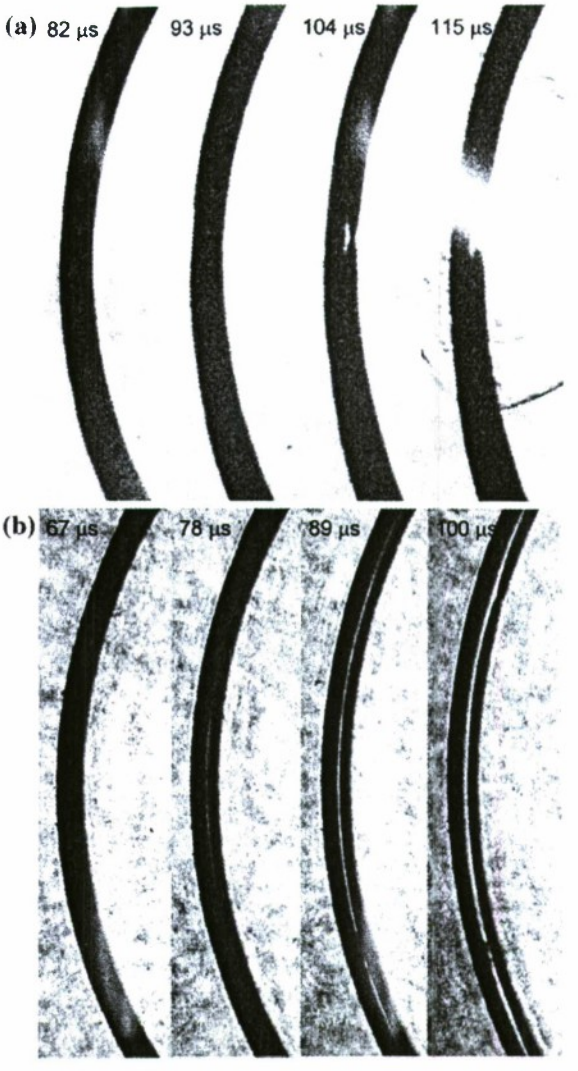

Fig. 8 **a** Emergence of localized deformation in polyurea coated Al 6061-O specimen; **b** interfacial debonding in polyurea coated Cu 101 specimen

Cu 101, the coating debonded completely during a brief change in the acceleration of the copper as shown in Fig. 8b; this is attributed to the lower adhesion strength of the Cu 101-polyurea bond. Therefore, the polyurea coating had no significant effect on the strain evolution, localization, and fragmentation of the Cu 101 ring specimens; further studies are underway where the adhesion is influenced by chemical intervention and the results will be reported in a future contribution. The upper bounds for the strain at the onset of localization can be estimated from such high speed images (see Part I for a discussion of this estimate). These bounds for Al 6061-O are shown in Fig. 9a. The open blue circles correspond to $\alpha = 4$ and open red circles for $\alpha = 10$; the uniform strain that was measured in the fragments of bare Al 6061-O specimens is also shown by the filled circles of the same color. The Considère strain is indicated by the red dashed line. Similarly, the results corresponding to the Cu 101 are shown in Fig. 9b; the open circles indicate the upper bound strain at the onset of localization for $\alpha = 6$. As already discussed in Part II, the increase in the strain at the onset of localization in the large aspect ratio specimens and the dependence on the expansion velocity is due to the propagation of the localization across the cross-sectional dimension. From these results, it is clear that there is *no significant effect of the polyurea coating on the strain at the onset of localization*. This result is in contrast to the expectations of the perturbation model for the onset of necking presented by Guduru et al. (2006) or the bilayer model presented by Xue and Hutchinson (2008). We will discuss the results in light of the above models and a direct numerical simulation in Sect. 5.

Statistical analysis of the distance between necks or localization sites follows trends nearly similar to those observed in Parts I and II for Al 6061-O rings without polyurea coating. The distribution of the distance between localization for Al 6061-O without and with polyurea coating is shown in Fig. 10 for the same expanding velocity, but for two different aspect ratios. Once again, with increasing strain rate, more necks are nucleated at shorter distances since the unloading

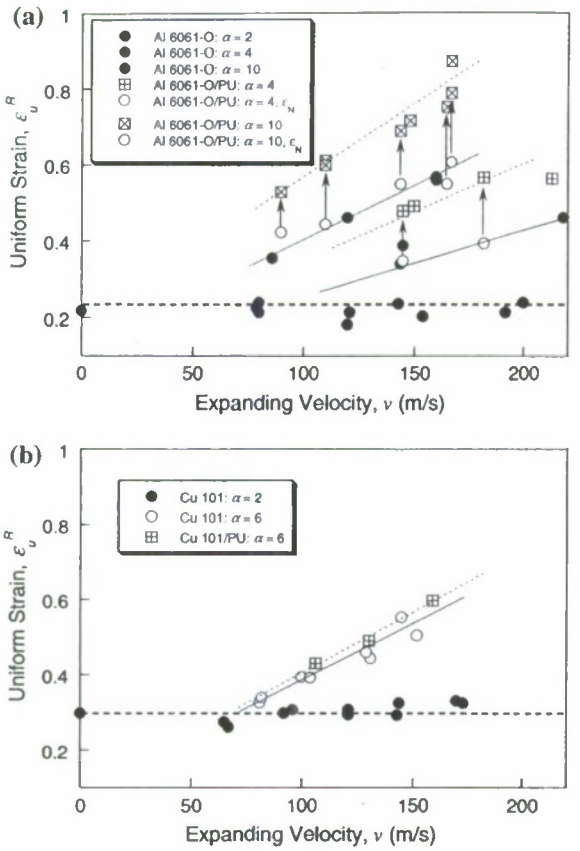

Fig. 9 Upper bounds of strain when localization starts and uniform strains measured in the fragments of (**a**) aluminum, and (**b**) copper. The uniform strains measured in the fragments of uncoated specimens are also given

generated by any localization does not travel quickly to inhibit further nucleation at neighboring locations. The statistical distribution of the distance between localization can be interpreted in a manner analogous to that for the uncoated rings discussed in Parts I and II.

The high speed images beyond the fragmentation of the metal indicate the deceleration of the polyurea and its subsequent retraction; while these images do not present much information of immediate interest in this problem, one important conclusion is that the polyurea does not dissipate any significant portion of the energy provided into the composite ring. The aluminum pieces that separated from the polyurea retain significant kinetic energy and fly away from the field of view with nearly undiminished kinetic energy to be captured in the clay lining of the container, while the polyurea returns nearly all the energy associated with stretching it to $\lambda = 2$.

Finally, we examine the recovered fragments to determine the residual deformation in the metal fragments. Figure 11 shows a comparison of two fragments, one from a bare Al 6061-O specimen and the other with a polyurea coating. The large aspect ratio specimens exhibit a slight curvature that is generated by the axial variations in the electromagnetic loading, and therefore the fragment dimensions were evaluated with a micro X-ray tomography system (μCT80 from Scanco Medical Inc). From the figure, it is clear that the polyurea coated specimens experience a significantly greater strain at regions away from the localization than the bare Al 6061-O specimens. The uniform residual strain in the fragments of the polyurea-coated Al 6061-O specimens away from the fractures and localization, denoted as before by ε_u^R, is shown in Fig. 9a (square symbols with a cross inside) as a function of the ring expansion speed for the two different aspect ratios $\alpha = 4$ and $\alpha = 10$; the arrows point from the corresponding upper bound for the uniform strain determined from the high speed images (open circles). It is clear that the uniform strain in the regions that did not localize is quite large, reaching true strain levels greater than 0.8 (corresponding to a stretch larger than 2.2). Thus, while the polyurea coating did not influence the onset of localization, it appears to have played a very significant role in the deformation that the aluminum specimen experiences in regions removed from the localization. Similarly, recovered fragments from the Cu 101 specimens were also examined to determine ε_u^R; these results are shown in Fig. 9b (square symbols with a cross inside). The polyurea appears to do very little to the uniform strain in Cu 101; this is clearly a result of the poor adhesion and the resultant debonding of the coating.

The experimental observations of localization clearly indicate that there are three phases in the process: in the first stage we observe the nearly independent and simultaneous nucleation or initiation of the localization at the most critical flaws. The second stage corresponds to the propagation or growth of the localization across the characteristic structural dimension; this growth phase depends on the cross-sectional dimensions of the specimen. Finally, in the third stage the propagation of unloading from the localization inhibits the surrounding regions from continued straining. These stages were clearly demonstrated in Part II for the bare metal rings where the cross-sectional dimension was varied in order to influence the time for propagation of the localization across the specimen

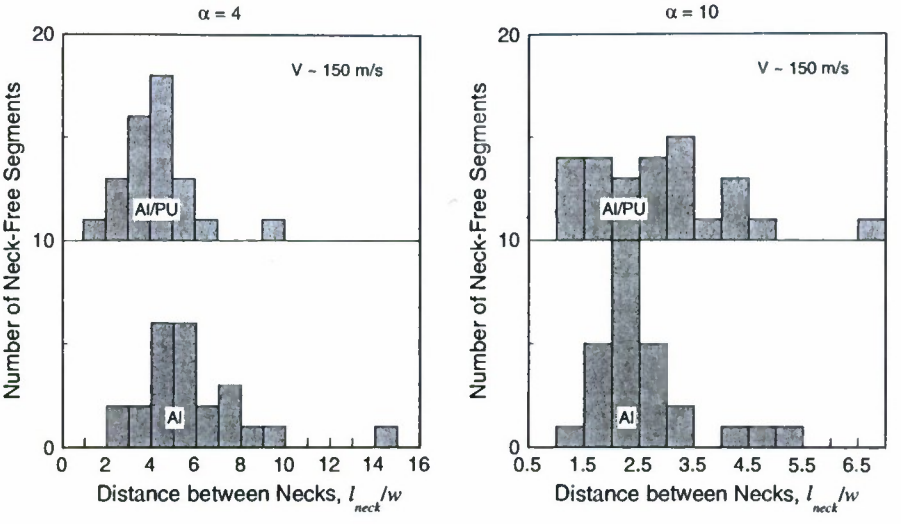

Fig. 10 Distribution of the distance between necks for Al 6061-O without and with polyurea coating

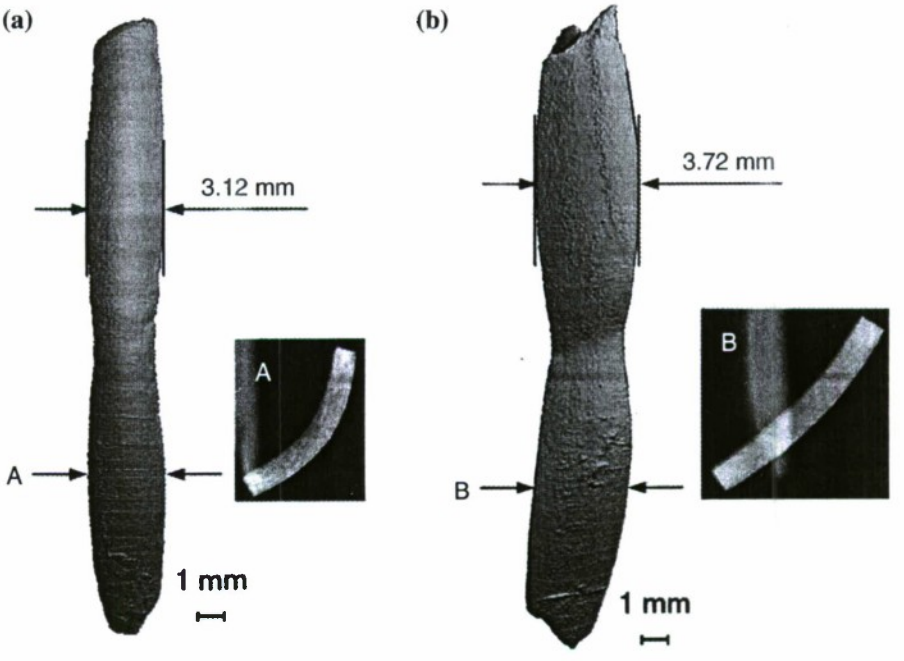

Fig. 11 Fragments from (**a**) a polyurea coated Al 6061-O specimen, and (**b**) a bare Al 6061-O specimen. Cross-sectional view is also shown for both fragments

cross-section; the results presented here imply that polyurea coating does not influence the first stage. We anticipate the effect on the propagation across the cross-sectional dimension to be small since the time scale for propagation of localization across this dimension is short. There is a clear influence in the propagation of unloading from the localization: simply by slowing the propagation of the unloading generated by the localization, the polyurea coating enables the aluminum to strain more in regions remote from the localization; this causes a greater energy dissipation in the metal specimen while the polyurea itself does not store or dissipate significant energy.[1] However, this effect on the unloading phase is observed only in the aluminum, and not in

[1] In an effort to incorporate additional energy dissipation mechanisms, we have replaced the polyurea coating with polycarbonate, a shear yielding polymer that exhibits significant plastic deformation at stress levels of about 100 MPa and a true failure strain of about 0.6. Preliminary experiments have indicated that this coating also does not influence the onset and growth of the localization significantly, but due to the energy dissipation associated with the plastic deformation in the polycarbonate, much of the kinetic energy from the metal is used up and the fragments fly away with very little kinetic energy. Details of these results will be reported in a future contribution.

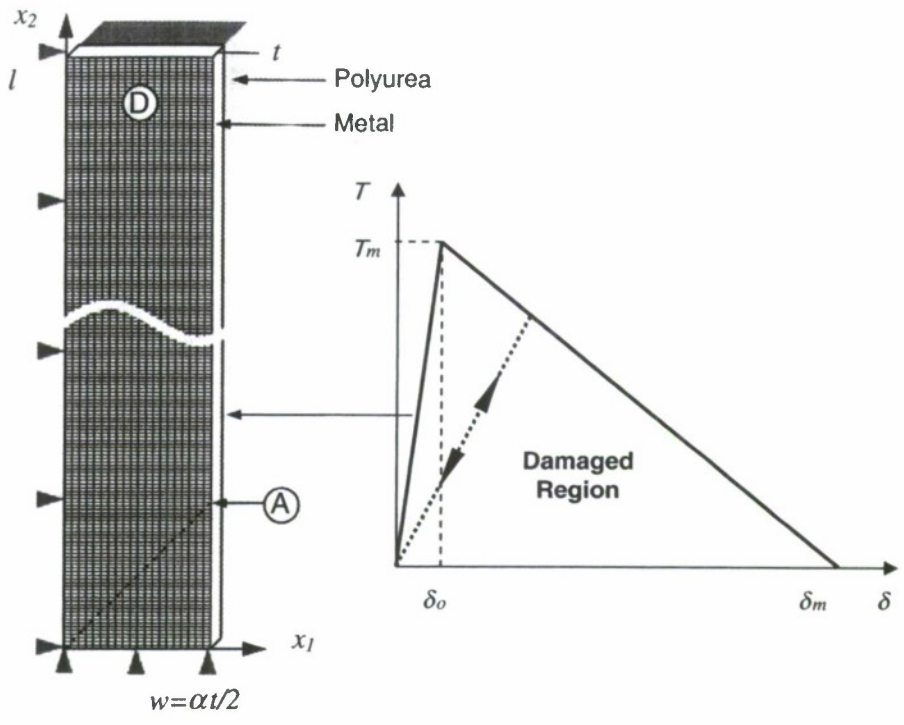

Fig. 12 Finite element discretization of a plate ($\alpha = 40$) with polyurea coating used for simulation of dynamic strain localization considering coating effect. A material defect is considered in the central region of the specimen indicated by the shading. The cohesive zone model used in the simulations is shown on the right side; the numerical values of the cohesive zone parameters for the polyurea Al 6061-O and polyurea Cu 101 interfaces are given in Sect. 3

the copper specimen; we believe that the influence on the propagation of the unloading is simply an added mass or inertial effect and will explore this and other aspects of the localization behavior further in the next section through numerical simulations.

5 Modeling and numerical simulation of localization in metal-polymer bilayers

The main conclusion derived from the experiments reported here is that coating the metal ring with a high-elongation, low-modulus polymer does not influence the process of neck initiation or propagation across the cross-section significantly, but is able to affect the propagation of unloading waves, thereby enabling the metal to strain to significantly higher levels than the bare metal. In this section, we begin with a discussion of the bifurcation analysis of Guduru et al. (2006), the numerical simulations of Xue et al. (2008) and the coupled simulations of Thomas and Triantafyllidis (2008) in comparison with the experimental results. Finally, we present the results of a numerical simulation that models the present experiments.

Guduru et al. (2006) performed a bifurcation analysis in order to determine the influence of a polymer coating on the high-strain rate strain localization and fragmentation behavior of a ductile material. In this analysis, they considered a sandwich structure of length $2L$ with inner core $2a$ and an outer layer (coating) of thickness $(b-a)$ that is assumed to undergo a homogeneous plane strain deformation at a constant strain rate $\dot{\varepsilon} = \pi v_0/L$ over its entire length. Both the core and coating material were represented with the hypoelastic material model of Storen and Rice (1975). A linear stability analysis was conducted by imposing perturbations in the axial and radial deformations of the rod, consistent with the incompressibility of the material. The equations of motion, linearized with respect to the homogeneous initial state, were examined to determine conditions under which these perturbations would continue to grow indicating a bifurcation in the solution. While all wavelengths of perturbations grow, Guduru et al. (2006) identified the wavelength corresponding to a maximum preset growth rate as indicative of the bifurcation strain and wavelength. Their results predict an increase in the bifurcation strain in the presence of the coating; concomitant with this increase in the bifurcation strain is an

increase in the plastic dissipation in the material. They show further that it is the hardening exponent of the coating that plays a major role in determining the magnitude of the increase in the bifurcation strain, while the strength and density of the coating play a secondary role. We note that the predictions of this analysis are not in agreement with our experimental observations, but the reasons for this deviation can be understood easily: the analysis is predicated on a perfect interface between the core and the coating throughout the onset and growth of the necking bifurcation. With such a perfect interface, a coating with a higher hardening exponent inhibits the tendency of the core to neck at a lower strain. However, we see in the experiments that metal pulls away from the coating and does not hinder neck formation. Therefore, the interfacial strength must play a crucial role in dictating the combined response of the core and coating.

Xue and Hutchinson (2008) examined the effect of polymer coating on the necking behavior of metal layers through a plane-strain finite element simulation. The metal layer was modeled as a power-law hardening elastic-plastic material and the polymer layer was modeled as a nearly incompressible Mooney-Rivlin material. The interface between the metal and the polymer was assumed to be perfect, thus imposing continuity conditions on the displacements and tractions across the interface. The overall stretch rate was varied from about 100–1,000 s^{-1}. The lower end of this range may be adequate to capture the quasi-static limit as indicated by Xue and Hutchinson (2008), but the higher end is an order of magnitude lower than what was imposed in the expanding ring experiments. From the results of the numerical simulations, Xue and Hutchinson (2008) assert that the neck nucleation is retarded by the addition of the polymer layer at high strain rates. In particular, they identify that the ratio of the initial elastic modulus of the coating E_e to the flow stress σ_R in the metal as the key controlling parameter in dictating this retardation in nucleation; when this ratio is close to unity, the strain in the metal can increase quite dramatically. For the combination of the polyurea/aluminum and polyurea/copper used in the present work, the ratio E_e/σ_R is nearly 1.4. Therefore, one expects that necking would be inhibited nearly completely. Nevertheless, the present experimental results indicate very little influence on necking; once again, the difference between the predictions and observations is due to the imposition of displacement and traction continuity across the interface between the metal and polyurea layers. The strength of the interface is simply not adequate to constrain the necking response of the metal. Xue and Hutchinson (2008) also suggest that the appearance of multiple necks is governed by the polymer stiffness at low rates but by inertia at the higher rates considered. The strain rates considered by Xue and Hutchinson (2008) are one order of magnitude lower than that used in the present study; therefore, the multiple necks observed in their analysis is not necessarily similar to the multiple necks observed in the present experiments that are predominantly independently nucleated necks.

The two comparisons discussed above demonstrate the fundamental need for additional experiments to determine whether increasing the adhesive energy of the bond would eliminate the interfacial debonding and therefore intervene with the development of the localization; we hope to address this issue in a future contribution. The question of whether this interfacial energy can be increased significantly beyond the 1 kJ/m^2 observed here remains open. However, before embarking on such an investigation, one might gain additional insight into the role of the adhesive interface between the metal and the polymer coating through numerical simulations of the experiments presented here.

We perform these simulations of the composite ring expansion problem using a simple power-law hardening elastic-plastic constitutive model for the metal and a nonlinear elastic model for the polyurea, utilizing the uniaxial stress–strain curve shown in Fig. 1 and modified by the factor k to account for the high strain-rate effects that are important in the expanding ring test. The simulation is performed in two steps; in the first step, a steady-state deformation is imposed on both the metal and polyurea by specifying nodal velocities $\dot{u}_2$ at all nodes such that a uniform strain at a rate of $\dot{\varepsilon}_{22} = 10^4\ s^{-1}$ is attained; the development of transverse strain $\dot{\varepsilon}_{11}$ in response to this is influenced by the specimen aspect ratio and occurs unconstrained by external conditions. When the uniform strain in the specimen is close to the Considère strain for the metal, the imposition of nodal velocity is terminated, and the continued elongation of the specimen, governed only by the inertia of the specimen, is monitored in the second step of the simulation. This is an idealization of the real loading, but it captures the essential ingredients of a rapid initial loading. Upon termination of the velocity specification, the effect of the defect in

triggering the accumulation of large plastic strains in a localized region in its vicinity becomes manifest, with the region of localization evolving with time and enveloping regions surrounding the initial defect. In the finite element discretization, a plate of thickness $t = 0.5$ mm, coating thickness $t_{pu} = 1.0$ mm, length $l = 50$ mm, and the half width $w = \alpha t/2$, where α is the specimen aspect ratio, is considered. The length of the specimen is selected in order that the release wave from the top of the plate is not able to reach the bottom and affect the localization during the timescale of the simulation. A finite element discretization of the specimen with aspect ratio $\alpha = 10$ is shown in Fig. 12. Eight-node linear brick elements with reduced integration and hourglass control (C3D8R) are used. The total number of elements for the plate is 192000 ($t \times w \times l$: $4 \times 20 \times 800$ for the metal layer and $8 \times 20 \times 800$ for the polyurea layer) and the same element size is used for specimens with other aspect ratios. The J_2 incremental theory of plasticity is used to model the metal layer; the uniaxial power-law constitutive model given in Eq. 13 of Part I is used for the Al 6061-O. One region identified by the shading in the lower left hand corner in Fig. 12, is used to simulate the defect region; the elements with the material defect are assumed to possess a yield strength of 25 MPa and to exhibit no strain-hardening. The polymer is modeled as a nonlinear hyperelastic material, with the stress strain response given in Fig. 1. The interface between the metal and polyurea layers is represented with a cohesive zone model. Based on the results of Zhu et al. (2009) and the adhesive energy measurements presented in Sect. 3, we take the traction-separation law for the polyurea coated on either of the two metals to be bilinear of the form illustrated in Fig. 12 ($T_m = 20$ MPa, $\delta_0 = 2\,\mu$m and $\delta_m = 100\,\mu$m for the Al–PU interface and $T_m = 15$ MPa, $\delta_0 = 1.5\,\mu$m and $\delta_m = 50\,\mu$m for the Cu–PU interface). This cohesive zone model is then incorporated in the ABAQUS simulation. The time evolution of the plastic deformation along the length of the bar appears to be very similar to that demonstrated in Part II for the bare metal. The time-evolution of the effective plastic strain was evaluated from two simulations with cross-sectional aspect ratio of $\alpha = 2$ and $\alpha = 40$; both simulations correspond to an expanding velocity of 200 m/s and a strain rate of $10^4\ s^{-1}$. In order to make the strain evolution visible, the effective plastic strain at any point normalized by the effective plastic strain in the uniformly deforming region was examined in a manner similar to that reported in Part II. It was clear from these simulations that, as in the simulations reported in Part II, the defect "triggers" the strain localization in the form of a narrow band and that this localization propagates along the characteristic direction until it meets the traction free surface. In an effort to examine quantitatively the dynamics of propagation of the localization and to probe its influence on the further evolution of strain in regions away from the localization, we plot in Figs. 13 and 14, the time evolution of strain at points labeled A and D in Fig. 12. These points are selected since points A lies on the characteristic localization line at the free boundary, and the point D is located at a distance of $20w$ and w (10 mm away from the defect in the undeformed state in both cases) respectively from the defect. For comparison, the results of the simulation in Part II of the corresponding pure Al 6016-O specimen are also shown; Fig. 13a, b correspond to $\alpha = 2$ for Al 6061-O and Cu 101 while Fig. 14a, b show the results for $\alpha = 40$. The dashed lines correspond to pure metal specimen and the solid lines correspond to the polyurea coated specimens. Initially, the strain increases uniformly at the same rate as the background strain rate at all monitored points in both the coated and bare specimens. From the results in Figs. 13 and 14 we deduce the following:

1. For the bare metal ring, the strain at the point A accumulates very rapidly beginning at about 20 μs for $\alpha = 2$; this is the onset of strain localization for this specimen. The result of this localization is a rapid drop in the stress at other points in the specimen. This rapid unloading stops further evolution of strain at points in the neighborhood of A within the next few microseconds, and at the point D after another 20 μs. Thus, for points in the range of $10w$ from the defect, if a neck has not already formed independently from a local defect before this time, it cannot form any more because of the unloading associated with the neck that has already formed at the first defect.
2. For the polyurea coated aluminum specimen, very nearly the same sequence of events occurs; localization appears across the cross-section at nearly the same time as the uncoated specimen. The major difference is that the strain at the point D increases for a slightly longer duration in the Al 6061-O because the propagation of the unloading is affected by the

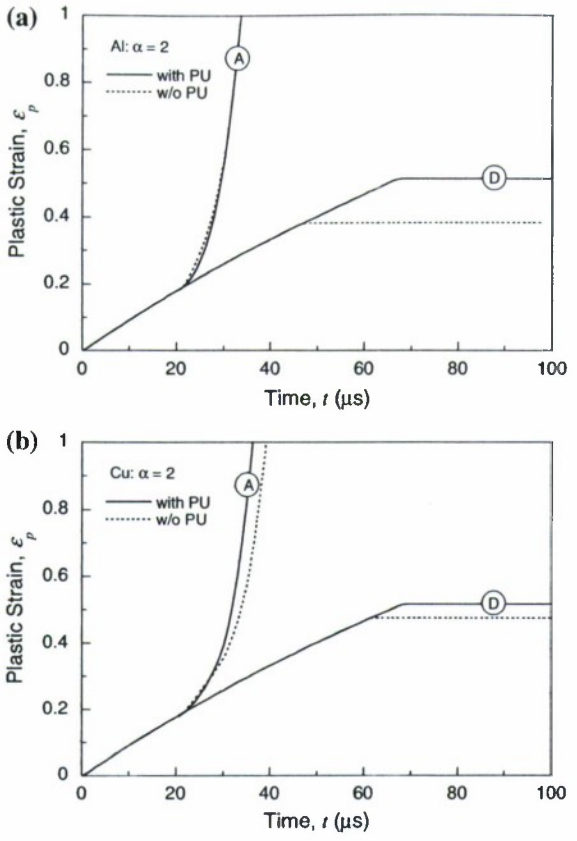

Fig. 13 Time variation of the strain at the monitoring points A and D in simulations ($\alpha = 2$) without and with polyurea coating: **(a)** aluminum, and **(b)** copper

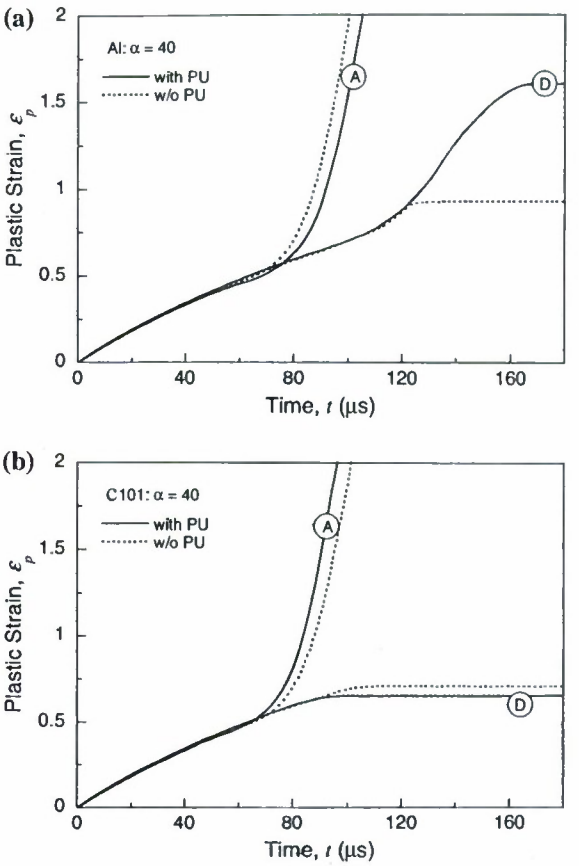

Fig. 14 Time variation of the strain at the monitoring points A and D in simulations ($\alpha = 40$) without and with polyurea coating: **(a)** aluminum, and **(b)** copper

polyurea coating; this is consistent with the larger uniform strain that was measured in the fragments.

3. For the polyurea coated copper specimen, the same sequence of events occur; however, the effect on unloading experienced in the aluminum specimen is not observed. Since the only major difference between the two simulations is in the density ratio, it would appear that the influence of polyurea can be attributed to an added-mass effect.
4. When the cross-sectional aspect ratio is increased to $\alpha = 40$, the onset of localization is delayed until about 80 μs; there is a corresponding increase in the strain at onset of necking. This increase depends on the expansion speed are reported in Part II for both experiments and simulations. The point D experiences a larger uniform strain in the Al 6061-O coated with polyurea, as observed in the experiments summarized in Fig. 9a.
5. In contrast, for the polyurea coated Cu 101 specimens, the coating provides very little enhancement in the uniform strain at the point D; this is also in accord with the experimental observation shown in Fig. 9b.

The results of the simulations are in total agreement with two key experimental observations: (i) in the polyurea coated Al 6061-O specimens, regions away from the neck experience a significantly larger strain than the uncoated specimens and (ii) in the polyurea coated Cu 101 specimens, the coating provides very little additional strain in the metal. These effects are the result of the unloading resulting from the necking localization and are influenced significantly by the inertia of the metal layer. Recent simulations by Thomas and Triantafyllidis (2008) of the ring expansion experiment, with a hyperelastic coating on a metal specimen, also revealed that inertia of the added mass, rather than the

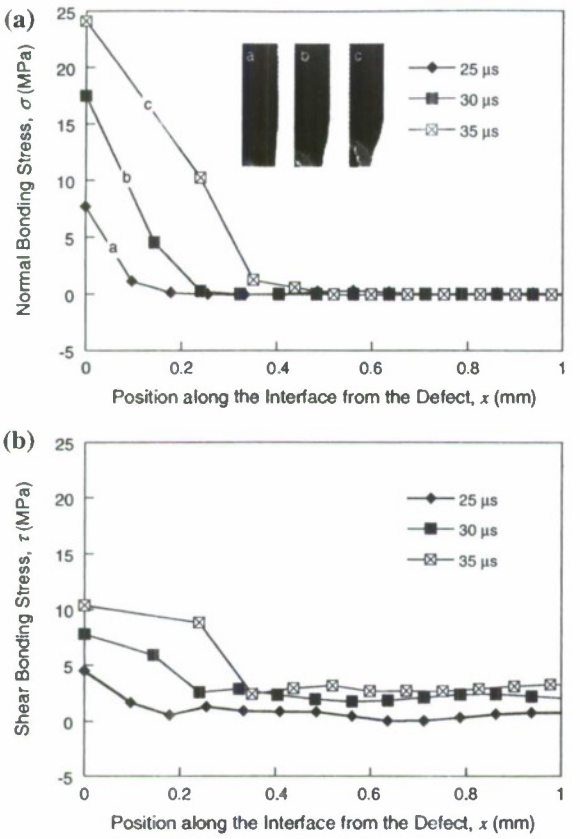

Fig. 15 Normal and shear stresses along the interface of Al 6061-O-PU in a coated aluminum bar with $\alpha = 2$. The inset in (**a**) shows the evolution of the cohesive normal stress in the interface between the metal and the polyurea

stiffness of the coating material, was the main contributor to the observed decrease in the deformation of the aluminum specimen.

In order to explore the effect of the adhesive energy, we performed another simulation in the polyurea-Al 6061-O system in which the interface was assumed to be perfect; this simulation is similar to that explored by Xue and Hutchinson (2008) except that these authors used plane strain conditions and the present work is a fully three-dimensional formulation. The main objective of our simulation is to explore the development of the interfacial stresses. At a strain rate of $10^4\ s^{-1}$, it is clear that the defect triggers the first neck in the simulation, and additional localizations along the characteristic distances appear as discussed in Part II, but only at very long times (as we showed in Part II, it is more likely that in the experiments, defects trigger other localization events independently). In order to understand the debonding experienced in the experiments, we track the normal and shear stresses along the interface, as the strain in the metal-polymer bilayer increases towards the bifurcation point and beyond. These are plotted in Fig. 15 for a point in the interface where the localized deformation is expected to appear. Note that the discrete simulation with the cohesive zone model does not capture the actual stress magnitudes precisely, but it gives an indication of the rapid increase in the interfacial stress. Two major observations are in order: first, in this three dimensional simulation, there is no tendency for the polyurea layer to delay the onset of localization in the metal layer; second, the normal and shear stresses required to keep the interface intact increases significantly with increasing strain (or time), even as the polymer simply mimics the deformation of the localized region; if it were to act to retard this deformation, the stress must be significantly higher. Given that the polymer stiffness drops dramatically at stress levels above a few MPa, it is hard to imagine that the polyurea layer can inhibit the development of localized deformation in the metal layer. Perhaps, other polymers, such as epoxies that can sustain much higher ($\sim$100 MPa) (Mello and Liechti 2006) interfacial stress levels may be able to resist delamination; this requires further examination.

Based on the experimental observations and numerical simulations, we suggest that a polymer layer weakly bonded to the metal does very little to retard the formation of the localized deformation in the metal, but that the inertial effect of delaying the propagation of the unloading from localization is the main reason for the enhanced metal deformation seen in polyurea coating in metal-polymer bilayer systems. As noted earlier, the polyurea also does not dissipate any significant portion of the work done on it during the deformation; it might be useful to consider the use of a different polymer, such as the shear yielding polycarbonate, to dissipate additional energy and thereby intervene in the dynamic deformation of the bilayer; we will report on these studies in a future contribution.

6 Conclusion

The effect of providing a compliant polymeric coating on metallic materials to influence their localization and failure behavior was examined through careful experiments and numerical simulations.

1. We observe that the process of localization occurs in three phases: nucleation, neck propagation across the cross-sectional dimension and finally unloading of neighboring regions. Under quasi-static loading conditions, the coating does not interact with any of the above processes that occur at a much shorter timescale and, therefore, does not influence the onset of localization in any meaningful manner.
2. Under high strain-rate loading, nucleation and propagation are not significantly affected, but the propagation of unloading along the length of the specimen is influenced, resulting in greater strains at regions away from the site of the localization. This appears to be simply an effect of the added mass of the polyurea, rather than any change induced in the intrinsic deformation mechanisms of the material or the mechanics of localization itself.
3. Adhesion between the polyurea and the metal layer is an important parameter that has not been examined systematically in the present work; we settled on the native strength that is achieved between the metal and the polyurea. However, numerical simulations indicate that even obtaining perfect bonding between the two layers is unlikely to result in a significant delay in the onset of localization.

Acknowledgements This work was performed under a program entitled "Characterization of Nonlinear Viscoelastic and Adhesive Properties of Polyurea and Characterization of Polyurea-clad Metallic Structures" sponsored by the Office of Naval Research (ONR Grant Number N00014-06-1-0644, Program Manager: Dr. Roshdy Barsoum); this support is gratefully acknowledged.

References

Amini MR, Isaacs JB, Nemat-Nasser S (2006) Effect of polyurea on the dynamic response of steel plates. In: Proceedings of the SEM annual conference and exposition on experimental and applied mechanics, June 2006

Amirkhizi AV, Isaacs J, McGee J, Nemat-Nasser S (2006) An experimentally-based viscoelastic constitutive model for polyurea, including pressure and temperature effects. Philos Mag 86:5847–5866. doi:10.1080/14786430600833198

Chakkarapani V, Ravi-Chandar K, Liechti KM (2006) Characterization of multiaxial constitutive properties of rubbery elastomers. J Eng Mater Tech Trans ASME 128:489–494

Gududru PR, Freund LB (2002) The dynamics of multiple neck formation and fragmentation in high rate extension of ductile materials. Int J Solids Struct 39:5615–5632. doi:10.1016/S0020-7683(02)00367-0

Guduru PR, Bharathi MS, Freund LB (2006) The influence of a surface coating on the high-rate fragmentation of a ductile material. Int J Fract 137:89–108. doi:10.1007/s10704-005-3066-0

http://www.ara.com/. Accessed on March 21, 2008

Jiao T, Clifton RJ, Grunschel SE (2007) Pressure-sensitivity and tensile strength of an elastomer at high strain rates. Shock Compression Condens Matter 955:707–710. American Institute of Physics, New York

Knauss WG (2003) Viscoelastic material characterization relative to constitutive and failure response of an elastomer, interim report to the Office of Naval Research. GALCIT, Pasadena, CA

Mathews W (2004) Services test spray-on vehicle armor, Army Times, May 3, 2004

McShane GJ, Stewart C, Aronson MT, Wadley HNG, Fleck NA, Deshpande VS (2008) Dynamic rupture of polymer-metal bilayer plates. Int J Solids Struct 45:4407–4426

Mello AV, Liechti KM (2006) The effect of self-assembled monolayers on interfacial fracture. J Appl Mech 73:860–870

Roland CM, Twigg JN, Vu Y, Mott PH (2007) High strain rate mechanical behavior of polyurea. Polymer 48:574–578

Storen S, Rice JR (1975) Localized necking in thin sheets. J Mech Phys Solids 23:421–441

Thomas JD, Triantafyllidis N (2008) On electromagnetic forming processes in finitely strained solids: theory and examples. J Mech Phys Solids (submitted)

Xue Z, Hutchinson JW (2008) Neck development in metal/elastomer bilayers under dynamic stretching. Int J Solids Struct 45:3769–3778

Xue Z, Vaziri A, Hutchinson JW (2008) Material aspects of dynamic neck retardation. J Mech Phys Solids 56:93–113

Yi J, Boyce MC, Lee GF, Balizer E (2006) Large deformation rate-dependent stress–strain behavior of polyurea and polyurethanes. Polymer 47:319–329

Zhang H, Ravi-Chandar K (2006) On the dynamics of necking and fragmentation: I. Real-time and post-mortem observations in Al 6061-O. Int J Fract 142:183–217

Zhang H, Ravi-Chandar K (2008) On the dynamics of necking and fragmentation: II. Effect of material properties, geometrical constraints and absolute size. Int J Fract 150:3–36

Zhao J, Knauss WG, Ravichandran G (2007) Applicability of the time-temperature superposition principle in modeling dynamic response of a polyurea. Mech Time Depend Mater 11:289–308

Zhu Y, Liechti KM, Ravi-Chandar K (2009) Direct extraction of rate-dependent traction-separation laws for polyurea/steel interfaces. Int J Solids Struct 46:31–51

APPENDIX D

Dynamic fragmentation in ductile materials

H. Zhang and K. Ravi-Chandar

Journal of Physics. D: Applied Physics (to appear, 2009).

Dynamic fragmentation of ductile materials

H. Zhang and K. Ravi-Chandar[1]

Center for Mechanics of Solids, Structures and Materials
Department of Aerospace Engineering and Engineering Mechanics
The University of Texas at Austin, Austin, TX 78712-0235, USA

Abstract: The subject of dynamic fragmentation of materials has been of significant interest both from a fundamental point of view and in technological applications. In this review, we summarize the highlights of the theories and models developed to capture these phenomena and discuss some critical experimental observations that provide the underpinnings for such theories.

1. Introduction

The branch of physics concerned with the fragmentation of materials has a long and rich history. Diverse communities of researchers – condensed matter physicists, materials engineers, geophysicts, fracture mechanicians, armament designers, mining and manufacturing engineers, and others – have tackled these problems over nearly a century. From a very fundamental point of view, in pioneering studies, Mott (1947) became interested in the break-up of artillery shells during World War II and suggested a statistical model augmented with an estimate of the propagation of the release waves from fractures; Grady (2006) explored fragmentation of many different materials and formulated an energy based scaling law; numerous others have contributed to the development of our understanding of fracture and fragmentation through experimental, analytical and computational studies of the problem of fragmentation. As recognized very early on by Mott (1947), the problems of fracture and fragmentation are intimately related to each other: both are governed by the material separation processes at the microstructural scale, and are mediated by the macroscopic loading at the structural scale. However, very different approaches have been used in consideration of fracture and fragmentation. In this paper, we present a critical review of the major features of the investigations into fragmentation problems with a focus on ductile materials.

The main objectives of studies into fragmentation are two-fold: (i) to provide a scaling relation that describes the mean fragment size in terms of underlying material properties such as the yield strength, fracture strength, fracture toughness on the one hand, and the strain rate on the other and (ii) to provide a framework for computational evaluation of the evolution of fragmentation. There are three main approaches that have been used in attaining these objectives: (a) purely statistical correlations that consider the distributions of fragment sizes (and shape) and correlate these with kinetic energy of the body prior to fragmentation have been discussed for a long time; while they are useful in categorizing fragmentation phenomena, they are not necessarily based on causal relationships and are not predictive; they are, however, quite useful in many practical applications; we do not consider this aspect further in the present paper. (b) Continuum models that rely either on statistic or energetic aspects of the problem and therefore amenable to simple solution procedures are used in developing scaling laws; these

[1] Corresponding Author: e-mail: kravi@mail.utexas.edu

models are attractive because they provide succinct formulas for fragment size as we will show later. (c) Discrete damage models that rely on continuum damage mechanics, discrete particle methods, cohesive zone models etc provide a computational framework from which one has to derive inferences on the fragment size distribution. With vast, inexpensive computing resources that have become available in recent years, techniques based on discrete models are gaining in popularity. When endowed with appropriate deformation, failure and constitutive models, these methods are capable of providing a good description of fragmentation on large scales.

This paper is primarily a review and is organized as follows: the Mott and Grady models of fragmentation are described in Sections 2 and 3, in order to set the background for the discussions to follow. Nucleation and growth models are briefly discussed in Section 4, but not considered in detail. A discussion of the salient experimental findings concerning fragmentation in ductile materials is presented in Section 5; these results are interpreted and discussed in view of the prevalent models. Numerical simulations of the fragmentation process through the various models are described in Section 6 along with a discussion of their validity in view of the experimental observations.

2. Mott's Theory of Fragmentation

During the years of the Second World War, Mott was engaged in understanding the fragmentation of pipe-bombs; his pioneering and insightful work in this area was finally published in the open literature (Mott 1947). The original analysis of Mott was based on two simple postulates: first that, unlike the macroscopic strength of brittle materials that is dominated by the presence of flaws, fracture in ductile materials would be governed by the standard deviation in the fracture strain in a material at the limit of its ductility. There is then a probability density function, $p(\varepsilon)$, associated with the failure strain; each material point can continue to accumulate plastic strain until it reaches its local value of the failure strain. The second postulate is that once a fracture appears, it generates an unloading wave that travels down to the unbroken parts, unloading regions encompassed by such release waves. These unloaded regions cannot sustain further strain or fracture, but other regions continue to experience the applied strains and hence are susceptible to fracture. The essence of Mott's theory of fragmentation is that the competition between the propagation of the release wave and the continued straining over the range of the failure strain distribution will dictate the distribution of fragment lengths. The most significant of his insights into the problem is the second postulate related to unloading of the solid: he determined that unloading proceeds at a much lower speed, and made an estimate of its progression in a simple rigid-plastic material model – we now refer to this release process as *Mott release waves*. The prototypical problem considered first by Mott, and in many experimental investigations that followed, is the uniform radial expansion of a thin ring specimen at a radial velocity v. However, it is convenient to consider a straight bar specimen for ease of analysis; the analysis presented here follows Kipp and Grady (1985). Mott's fragmentation model is shown schematically in Figure 1. Consider a rod that is subject to a uniform strain rate $\dot{\varepsilon}_0$. The particle velocity corresponding to this strain rate varies linearly in x, symmetrically about the center of the fragment and can be written as $v(x,t) = \dot{\varepsilon}_0 x$ as indicated by the dashed line in Figure 1. The material is considered to be rigid-perfectly-plastic, and therefore the stress everywhere in the

specimen is equal to the yield stress σ_y, again as indicated by the dashed line in Figure 1. Under this steady-state condition, let the specimen fracture at the point $x=0$, $t=0$. In Mott's fragmentation model, the stress in the specimen drops to zero instantaneously and the specimen begins to unload. At some time t after the fracture event, when the unloading (release) wave has progressed to the position $s(t)$, the gray shaded region is fully unstressed and moves as a rigid body with a constant velocity; this velocity is equal to $\dot{\varepsilon}_0 s(t)$ by requirement of continuity at $x=s(t)$. The governing equation for $s(t)$ can be obtained by equating the change in momentum of the unloaded block to the applied force as follows. Equating the change in momentum to the force across the unloaded segment, we get

$$\frac{1}{2}\rho\dot{\varepsilon}s\frac{ds}{dt}=\sigma_Y \tag{1}$$

This is easily integrated to yield the motion of the release wave front:

$$s(t)=\left(\frac{2\sigma_Y t}{\rho\dot{\varepsilon}}\right)^{1/2} \tag{2}$$

It is clear that the unloading does not have a wave character, but is more typical of a diffusive process. This diffusive nature of the *Mott release wave* can be explained heuristically: in each increment of time, as the release wave moves by an amount ds (hash marked region in Figure 1), the impulse from the unloading has to increase the velocity of the entire unloaded block to $\dot{\varepsilon}_0(s+ds)$ and hence the diffusion-like response. The expression in Eq.(2) can also be given a very simple physical interpretation with respect to fragment size: taking $(\sigma_Y/\rho)^{1/2}$ to be the speed of plastic waves, if we consider the standard deviation in the failure strains to be $\Delta\varepsilon$, then, in the time duration for generation of all fractures with this spread of failure strains, $\Delta\varepsilon/\dot{\varepsilon}$, the release waves propagate to an extent s on either side of the fracture and therefore the maximum fragment length ($\sim 2s$) can be written as

$$l_{MOTT}=2\left(\frac{2\sigma_Y t}{\rho\dot{\varepsilon}}\right)^{1/2}=2\left(\frac{2\sigma_Y\Delta\varepsilon}{\rho\dot{\varepsilon}^2}\right)^{1/2} \tag{3}$$

If we take $\sigma_Y=150$ MPa, $\rho=2700$ kg/m^3, as representative values for aluminum alloys, and consider the variation in the strain at the onset of necking to be about $\pm 2\%$ then we get $l_{MOTT}\sim 10$ mm for a strain rate of about 10^4 s^{-1}. Mott's theory predicts a linear scaling of the number of fragments with respect to the strain rate. We will explore this in light of numerous experimental results that have been accumulated in different materials. Note further that the estimate of the unloaded length from a single fracture event is representative of the fragment length; the actual statistical distribution of flaws that nucleate fracture will dictate the distribution of fragments. Mott addressed this issue by

using an exponcntial probability density funetion for the failurc strains; we will examine this aspeet next.

Mott (1947) considered the statistieal aspects of the problem carefully; in partieular, hc combined the unloading generated by the release wave with thc statistieal distribution of failure strain levels to obtain an estimate of the distribution of fragmcnt lengths. For the expanding ring of eurrent radius r, the rate of inerease of the number of fragments (per unit lcngth of the speeimen) with inereasing strain ean be written as

$$\frac{dN_f}{d\varepsilon} = (1-D)\,p(\varepsilon) \tag{4}$$

where $D = l_{MOTT}/(2\pi r)$ is the length fraetion that is unloaded by the release wave, the term $(1-D)$ aeeounts for the fact that eraeks eannot be nucleatcd in the unloaded regions and $p(\varepsilon)$ is the probability of failure at this strain level. Caleulation of D using thc first of Eq.(3) must be done with partieular attention paid to the overlapping of release waves from different fractures and the shielding of potential nucleation sites by the releasc waves. Mott resorted to a graphieal approach to get an estimate of the fragment distribution using a random distribution of defeets and an exponential distribution for $p(\varepsilon)$; Wesenberg and Sagartz (1977) used essentially the same proeedure but with a numerieal algorithm to eompute fragmcnt statistics ovcr large number of realizations. An example of Mott's distribution of fragment sizes, taken from Wesenbcrg and Sagartz (1977), is shown in Figure 2. In order to generate an analytical estimate of the fragment distribution, Grady (1981) applied the Johnson-Mehl-Avrami approach eommonly employed in nucleation and growth problems assoeiated with phase transformations. It is elear that the particular probability density function $p(\varepsilon)$ eonsidered for the failure strain will influenee the eventual fragment size distribution significantly. At low strain rates, the propagation of the unloading wave will dominate the distribution while at higher strain rates, the weakest failure points will dietate the fragment size distribution.

While many other researehers have augmented Mott's ideas on fragmentation, they represent amendments that aim to provide a rationale for the distribution of fragment lengths rather than a eompletely new formulation; the essential ingredient of the diffusive propagation of the unloading process is the main key to understanding fragmentation. Limitations of the Mott model have been widely discussed in the literature. First, the rclcase wavc speed tends to infinity at zero time; this is an artifact of the rigid-plastic material assumption and is easily removed. Lee (1967), Kipp and Grady (1985) and others have addrcssed this issue; most reeently, Zhang and Ravi-Chandar (2006, 2008) examined this through a direet numerical simulation of the unloading proeess with an elastie, power-law-hardening plastie material model and through a eomplete numcrical simulation of the expanding ring experiment. Second, it is not clear how the standard deviation in fracture strains could bc mcasured in independent experiments; this has been onc of the most scrious drawbacks of thc Mott model and has lcad to eonsiderations of other effects and models. Third, thc fraeture process is taken to be instantaneous but elearly must proeeed with some charaeteristie timescale that depends on the nature of the fraeture. Kipp and Grady (1985) addressed this issue by imposing a eohesivc zonc modcl

for the separation process and showed that the time to fracture plays significant role; we will examine this model in the next section. The final criticism of the Mott model, one that is especially relevant to ductile materials, is that it completely ignores the physical failure mechanisms. Ductile failure is almost always preceded by localization of deformation in narrow regions; such localization can be by tensile mechanisms leading to necking, void nucleation, growth and coalescenee or by shearing mechanisms leading to shear localization, void sheet formation, adiabatic shear band nueleation and growth ete. Many of these deformation and localization phenomena are governed by the geometric and loading conditions in addition to material properties; hence any scaling law that relies solely on material properties will, by necessity, miss aspects of the onset of localization and therefore the fragmentation problem. The diseussion of experimental and numerical results in Sections 5 and 6 respectively will clarify these aspects and reveal the underlying strengths of the Mott theory of fragmentation.

3. Grady's Fragmentation Model

Grady considered improvements to two aspects of the Mott model of fragmentation: the instantaneous appearance of the fraeture and the inability to pin down the statistieal properties of the failure strain in the material. In partieular, Kipp and Grady (1985) adopted a Dugdle-Barenblatt type cohesive zone model for the separation process; this is illustrated in Figure 3. Instead of abruptly setting the force across the potential fracture surface to zero as in the Mott model, the Grady model assumes that the stress carried by the material in the cohesive zone drops from σ_Y to zero linearly; thus

$$\sigma_{coh} = \sigma_Y \left(1 - \frac{2c(t)}{\delta_c} \right) \tag{5}$$

where $c(t)$ is the half-opening of the eohesive zone and δ_c is the critieal separation distanee at whieh the fracture is complete. For this linear cohesive model, the latter can be written in terms of the fracture surface energy, G_c, and the yield strength: $G_c = \sigma_Y \delta_c / 2$. We also note that in their model, the cohesive process was taken to model everything from the onset of localization (necking) to the eventual generation of new surfaces by void growth and coalescence and so, G_c is to be eonsidered to be energy dissipated in further plastic deformation as well as the cracking process. The net result of the Grady model is that the right-hand-side term in Eq.(1) is modified, simply by subtracting the resistanee provided by the cohesive springs from the driving force. Thus, we get:

$$\frac{1}{2} \rho \dot{\varepsilon} s \frac{ds}{dt} = \sigma_Y - \sigma_{coh} = \sigma_Y \frac{2c(t)}{\delta_c} \tag{6}$$

The introduetion of the cohesive fraeture resistanee further slows the propagation of the Mott release wave, but more importantly, it introduces an intrinsic timescale. Since the unloaded region is still considered to be a rigid body, compatibility requires that

$c(t) = \int_0^t \dot{\varepsilon}_0 s(t) dt$ and hence Eq.(6) is fully in terms of the position of the release wave front. Grady's model considers that the fragment size is set by the distance of propagation of the Mott release wave for the duration of the separation process; i.e., Eq.(6) is to be solved until $c(t_c) = \delta_c / 2$. Note that the unloading front should be able to relieve stress even for times longer than t_c, as long as it has not impinged on another release wave from a neighboring fracture event and therefore, in practice, one might observe fragments that are larger than this estimate. On the other hand, if there are fortuitous flaws that are closer than this distance, the fragments might be shorter. Therefore, assuming that the fragment length corresponds to unloading over the duration of the fracture process provides an approximate estimate of the fragment size that is somewhat intermediate to these extremes, but it is not possible to state whether this represents the mean spacing. Based on this analysis, Kipp and Grady (1985) estimated the time to fracture, t_c, and the fragment length ($\sim 2s(t_c)$) in terms of the yield strength, fracture energy and strain rate:

$$t_c = \left(\frac{9\rho G_c^2}{\sigma_Y^3 \dot{\varepsilon}} \right)^{1/3}, \; l_{KG} = \left(\frac{24 G_c}{\rho \dot{\varepsilon}^2} \right)^{1/3} \tag{7}$$

There is a numerical factor of two difference between the expression given by Grady (2006) and the above expression for the time to fracture; this is a result of assuming that $c(t_c) = \delta_c / 2$, with a symmetric opening on the neighboring fragment. Comparing the above estimate to that of Mott, it is clear that the quantity that is difficult to measure through experiments – the spread in failure strains, $\Delta\varepsilon$ – has been removed from the scaling law and the estimate of the fragment size is in terms of the fracture energy that is more readily measured. On the other hand, the yield strength of the material has been also been removed and thus the dependence of the fragmentation on the plastic properties of the material could not be captured by this model. Estimates of fragment lengths based on this analysis are similar in magnitude to the Mott estimate, but there are differences in the functional forms both in the scaling laws and predictions of fragment sizes as we shall show later.

The Grady model also provides a simple estimate of the nominal fracture strain; this is equal to the strain at the onset of the fracture process, ε_{f0} plus the strain accumulated during further straining at a rate of $\dot{\varepsilon}$ during the failure time, t_c; thus the failure strain is

$$\varepsilon_f = \varepsilon_{f0} + \left(\frac{9\rho G_c^2 \dot{\varepsilon}^2}{\sigma_Y^3} \right)^{1/3} \tag{8}$$

This predicts a $2/3^{rds}$ power scaling with respect to strain rate and suggests that the "ductility" of the material (defined as the strain-to-failure) increases with increasing strain rate. Experimental measurements on fragment size and strain to fracture were obtained by Grady and Benson (1983) and Grady and Olsen (2003) to support this idea; we will review these data in Section 5.

Grady's fragmentation model could also be posed in terms of energy balance. The initial kinetic energy of a fragment of length l_f that was expanding at a strain rate $\dot{\varepsilon}_0$ can be determined easily: $\frac{1}{24}\rho\dot{\varepsilon}_0^2 l_f^3$; note that this is the kinetic energy relative to the center of mass of the fragment. If this is equated to the fracture energy G_c, we get the following estimate of the fragment size:

$$l_f = \left(\frac{24G_c}{\rho\dot{\varepsilon}_0^2}\right)^{1/3} \tag{9}$$

Glenn and Chudnovsky (1986) suggested that the elastic strain energy in the body should also be included in performing the energy balance, particularly at lower strain rates; thus

$$\frac{1}{3}\rho\dot{\varepsilon}_0^2 a^3 + \frac{1}{2}\frac{\sigma_Y^2}{\rho c^2}(2a) - G_c = 0 \tag{10}$$

where c is the elastic wave speed in the specimen and $a = l_{GC}/2$ is the half-fragment length of the Glenn and Chudnovsky model. This is a cubic equation for the fragment length that can be rewritten and solved to yield

$$a^3 + \alpha a - 2\beta = 0,\ \alpha = 3\left(\frac{\sigma_Y}{\rho c\dot{\varepsilon}_0}\right)^2,\ \beta = \left(\frac{3G_c}{2\rho\dot{\varepsilon}^2}\right) = \frac{3}{2}\left(\frac{K_{IC}}{\rho c\dot{\varepsilon}}\right)^2 \tag{11}$$

$$l_{GC} = 4\sqrt{\frac{\alpha}{3}}\sinh\left(\frac{\phi}{3}\right),\ \phi = \sinh^{-1}\left[\beta\left(\frac{3}{\alpha}\right)^{3/2}\right], \tag{12}$$

where K_{IC} is the mode I fracture toughness of the material. The predictions of fragment size from the Mott, Kipp and Grady, and Glenn and Chudnovsky estimates are plotted as a function of the strain rate in Figure 4. The parameters used in obtaining these estimates are as follows: $\sigma_Y = 250\,\text{MPa}$, $\rho = 2700\,\text{kg/m}^3$, $c = 5092\,\text{m/s}$, and $G_c = 30\,\text{kJ/m}^2$; these values are representative of aluminum alloys. For the Mott estimate, we take the standard deviation in the failure strains to be $\Delta\varepsilon = 0.015$. At strain rates in the range of 10^3 – 10^4 s^{-1}, all three estimates provide similar fragment lengths even though the functional form of the scaling with strain rate is quite different; this aspect will be examined later through comparison to experimental results. The estimate of l_{GC} approaches the value given in Eq.(9) for large values of the strain rate, but at smaller strain rates, the estimate of Glenn and Chudnovsky approaches a rate independent quasi-static limit.

4. Nucleation and Growth Models of Fragmentation

Nucleation and growth models for crack growth were considered first by Zhurkov (1965) in relation to modeling thermally activated crack processes such as creep. Curran *et al.*, (1973) applied similar ideas to the stress-induced nucleation and growth processes that appear in the dynamic spalling problem. The models are essentially continuum damage models that can be summarized as follows: first, microcracks are considered to nucleate in a representative volume element (RVE) of the solid with a particular size distribution, and at a rate that is dependent on the stress level beyond a threshold stress. Based on experimental observations, Curran et al., assumed an exponential distribution of initial radii of the nucleated microcracks: $\Delta N(R) = \Delta N_0 \exp[-R/R_1]$, where $\Delta N(R)$ is the number of microcracks per unit volume with radius larger than R that are nucleated in a time interval Δt and R_1 is a parameter in the model. The nucleation rate of microcracks is assumed to be given by $\dot{N} = \dot{N}_0 \exp[(\sigma - \sigma_{n0})/\sigma_1]$ where σ_{n0} is the nucleation threshold, and σ_1 and $\dot{N}_0$ are constants to be determined through calibration experiments. Second, a growth rate is imposed on the microcracks such that $\dot{R}/R = \sigma - \sigma_0(R)/(4\eta)$ where $\sigma_0(R)$ is the critical stress for a penny shaped flaw of radius R to be fracture critical and η is the viscosity; this form was derived by Curran et al., from viscosity limited growth in ductile materials, but was also applied successfully to brittle materials by considering that the growth rate is controlled by a brittle fracture criterion. With this nucleation and growth model, for any load history, the current state of damage can be determined; so, in the third step, this damage is then used to degrade the material properties within this RVE. Finally, fragmentation is considered to occur when the volume of cracks in the RVE reaches a critical value. This continuum damage model can then be incorporated into numerical simulations of the stress field in the specimen. In contrast to the Mott and Grady models, this model requires calibration of the nucleation, growth and coalescence processes through numerous experiments and simple scaling laws cannot be written in terms of macroscopic material parameters. The main focus of these nucleation and growth based models is on material degradation; since the early work of Curran et al, other nucleation and growth models have been developed to capture the failure of ductile materials. These models are motivated by micromechanics where the details of void growth and coalescence are analyzed in detail through an elastic-plastic model of the material behavior; the Gurson-Tvergaard-Needleman (GTN) (Tvergaard and Needleman, 1984) and the Rousselier (Rousselier, 1987) models are perhaps most commonly used for simulations of fracture. In these models, the yield function describing the plastic constitutive model is modified to include softening due to void nucleation and growth all the way to complete failure. These models also require extensive calibration of the many model parameters; the extent of strain-rate sensitivity is not fully known, but such models have been used to examine fragmentation. The work of Becker (2002) who used the GTN model to simulate fragmentation will be reviewed later.

5. Experimental Investigations of Fragmentation

Mott relied on examining recovered fragments from explosion of cylindrical shells in order to arrive at the underpinnings of his model. He was guided by experimental results that indicated an exponential distribution of the mass of the fragments. Since that time, significant experimental evidence has been collected by a number of investigators as

discussed below. These investigations relied on different loading and diagnostic methods in order to understand the underlying proecsses leading to fragmentation.

5.1. Expanding Ring Experiment of Niordson

Direct experimental investigation of tensile fracture and fragmentation response at high strain rates was pioneered by Niordson (1965); he designed an electromagnetic loading scheme that was able to expand a thin ring specimen at strain rates in the range of 10^4 s^{-1}. The principle of electromagnetic loading for the expanding ring experiment is quite simple: the specimen is in the form of a thin circular ring of radius r_0 and cross sectional dimensions t and h, with t typically being significantly small in comparison to r_0. The axial length h dictates whether this is a ring or a tube and changes the problem from one to two dimensions; we will examine rings for now. This ring is inserted over a solenoid of n turns wound without pitch on a mandrel. A schematic diagram of such an apparatus is shown in Figure 5a. A close-up photograph of the experimental arrangement is shown in Figure 5b (for the details of construction of the solenoid please see Zhang and Ravi-Chandar, 2006). When a current, I_1, generated by discharging a 20 kV, 25 μF capacitor, is passed through the coil, an induced current, I_2, develops in the specimen; the Lorentz interaction between these conductors generates a repulsive force between the coil and the ring specimen. Since the coil is held fixed, the ring is forced to expand radially to speeds in the range of 80 to 200 m/s. Switching of the high current is accomplished by firing a thyratron-ignitron circuit that also allows for easy synchronization of the loading with recording systems. Since the specimen strains to about 25 to 45% in these experiments, we may neglect the elastic strains and approximate the plastic strain rate as $\dot{\varepsilon}_p = \dot{r}/r$. While Nirodson demonstrated the capability of this scheme, only preliminary observations were reported in his paper. In particular, he showed a beautiful image obtained with illumination from the sparks that appeared at the fracture points due to the induced currents circulating in the specimen ring. Since about nine sparks were recorded along the ring, he suggested that the fractures must have occurred almost simultaneously. He also showed that the fracture occurred after shear localization at an angle to the direction of tension.

5.2. Expanding Cylinder Experiment of Wesenberg and Sagartz

Wesenberg and Sagartz (1977) examined the problem of fragmentation in Al 6061-T6 cylindrical specimens. A modified version of Niordson's apparatus developed by Walling and Forrestal (1973) was used; a schematic diagram of this is shown in Figure 6. In this arrangement, a contoured copper sheet is inserted inside the cylindrical aluminum specimen and a current pulse I_1 is discharged through the copper sheet. Lorentz interaction between this current and the current I_2 induced in the aluminum specimen occurs as in the expanding ring arrangement of Niordson, resulting in an expansion of the cylindrical aluminum alloy specimen at high strain rates. Wesenberg and Sagartz (1977) used Al 6061-T6 cylinders 102 mm long, 127 mm in outer diameter and 1.27 mm wall thickness; the strain rates were in the range of 10^4 s^{-1}. A high speed framing camera was used to capture the fragmentation process. The strain just prior to the appearance of fractures was determined to be about 30%. Strain localization in the form of narrow

bands oriented at about 30° with respect to the axis of the cylinder were also observed. Furthermore, arcing was observed across the fractures as in Niordson's experiments. Wesenberg and Sagartz collected the fragments and determined the fragment size distribution; their results are shown in Figure 2. They also solved the Mott equations that incorporate the statistics of failure strain and the release wave propagation through a numerical algorithm. Two material parameters – the yield strength and the standard deviation in the fracture strain – were used in generating the Mott model estimate of the fragment size distribution. The close correlation between the experiments and analysis implies that these two parameters are sufficient to fit the Mott model to the experimental observations. This experiment represents the first direct confirmation of the validity of the two main concepts introduced by Mott in his fragmentation model.

5.3. Experiments of Grady and Benson

The capability of the expanding ring method was exploited by Grady and Benson (1983) who performed numerous experiments on OFHC copper and 1100-O aluminum; their measurements appear to have been the most extensive quantitative data set on fragmentation for a long time and hence most analysts have used these results for comparison with predictions. Grady and Benson used a streak camera to capture the time history of motion of a single point in the ring and thus were able to correlate the measured strain evolution in the expanding ring with lengths of the fragments collected after the test. The radial expansion speed of the ring was in the range of 18 to 220 m/s for the aluminum rings and 6 to 138 m/s for the copper rings; the corresponding strain rates were in the range of 10^2 to 10^4 s^{-1}. Two sets of experimental observations were gathered from their expanding ring tests and a number of conclusions were drawn from these results. First, Grady and Benson (1983) noted that the recovered fragments contained remnant necks that had not completely fractured. Therefore, they tabulated the number of arrested necks and successful fractures that were recovered; their results are reproduced here in Figure 7 where the number of fragments is plotted as a function of the ring expansion velocity (note that the strain rate is proportional to this velocity). The Grady model predicts the strain rate dependence to follow the $2/3^{rd}$ power law in Eq.(7); the data on the other hand, for both the OFHC Cu and the Al 1100 show that the dependence is linear, more in keeping with the Mott scaling indicated in Eq.(3). These results are a clear indication that the Mott theory is the governing theory in these ductile materials; we will reinforce this with new experimental results obtained by Zhang and Ravi-Chandar (2006,2008). Second, Grady and Benson (1983) plotted the mass distribution of the fragments and compared it with the analysis of Mott; this suggested that while the release wave idea was in reasonable agreement with the experimental observations, there were a significant number of fragments outside the Mott estimate. Finally, Grady and Benson used the total length of all the collected fragments to obtain a measure of the strain at fracture, after cautiously warning the reader that any such definition "of a dynamic fracture strain is somewhat nebulous." Their *ad hoc* dynamic fracture strain increased as a function of the expansion speed of the ring (proportional to the strain rate) as shown in Figure 8 – from 0.222 to 0.45 for aluminum and 0.47 to 0.65 for copper; in contrast, the quasi-static strain to failure (unspecified gage length) was 0.075 and 0.40 for the aluminum and copper respectively. Fitting a power-law dependence to the data, Grady suggested that the scaling indicated in Eq.(8) is indeed observed in the experiments.

However, since the fragments in ductile materials have numerous partially-developed neck regions where the strain is nonuniform, the final length of the fragment cannot provide a good estimate of the strain to fracture (which is a local property of the material). Unfortunately, many later studies have quoted this result as implying that there is an increase in material ductility with increasing strain rate. As shown by Zhang and Ravi-Chandar (2006), this is not an appropriate measure of "strain-at-fracture" or the ductility of the material.

Altynova et al, (1996), also explored one-dimensional fragmentation problem in ductile metals. Again with the expanding ring experiment, they determined the velocity dependence of the number of fragments in solutionized Al 6061 using the ring expansion experiment; they suggest that the $2/3^{rd}$ power law model is a good fit to the data, even though their plot shows significant deviation from the power-law model; in conjunction with the data of Grady and Benson (1983), we must conclude that the number of fragments is more likely to have a linear increase with strain rate rather than the power law; of course, it must be recognized that these data sets are limited to ductile materials. Altynova et al, (1996) also obtained two measures of ductility; recognizing that the partially-developed neck regions tend to bias the average strain over the ring to large strain values, they made local measurements of the uniform portion between necks to characterize the ductility and used both measures. Surprisingly, they found that the two measures did not differ significantly, even though the average strain is influenced by the numerous partially developed necks; furthermore, as the number of partially developed necks increase, the deviation between the average and local measures of strain must increase, a trend that does not appear in the results of Altynova et al, (1996). Through numerical simulations using a viscoplastic material model, these authors suggest that the primary influence arises from inertia.

5.4. Experiments of Zhang and Ravi-Chandar

Zhang and Ravi-Chandar (2006, 2008) repeated the expanding ring experiments of Niordson, Grady and Benson and others on Al 6061-O, Al 1100-H14 and Soft Cu 101, in order to address the issue of fragmentation in ductile materials. The main innovation in the experiments is that a high speed camera with very good spatial and temporal resolution was used to examine the onset and progression of fragmentation in ductile metal rings. This allowed for the determination of the precise sequence of events at different strain rates, strain levels and in different materials. While these results reinforced many of the earlier observations and models, they also provided insight that leads to reconciliation between the Mott and Grady models of fragmentation. All of the rings were of 15.5 mm mean radius and 0.5 mm thickness; the length of the specimen was varied from 1 mm to 5 mm in order to alter the mode of strain localization from diffuse necking in the smaller length specimens to sheet-mode or shear banding localization in the longer specimens. The strain rate in these experiments varied between 5,000 and 15,000 s^{-1}. A composite image from an Al 6061-O ring expanding test is shown in Figure 9. The high speed images from different times are superposed in one image to provide a quick view of the sequence of events in this fragmentation experiment. The expansion speed in this experiment was 200 m/s. The frame numbers are identified along the current lead on the top, with each frame being 11 μs apart. Necks are identified to nucleate after a period of uniform straining; the locations of the necks are

marked by the numbers inside circles, numbering them countercloekwise. In this experiment, 38 necks were nuclcated, nearly simultaneously and independently of each other, within a very short time interval. Of these necks, only 14 necks maturcd fully into fractures; the fracture locations are idcntified in Figure 9 by the numbers placcd insidc squares, numbering them in the time sequenee of their appearancc. This resulted in 14 fragments and 24 arrested necks within the fragments. Numerous experiments of this type were performed on speeimens with different materials and differcnt cross-sectional dimensions. In these experiments, the ring expands at nearly constant speed, resulting in a constant strain rate tensile loading of the specimen. From this collection of experiments (sce Zhang and Ravi-Chandar 2006, 2008 and Zhang et al, 2008 for full details), we idcntify that there are four important aspects to the fragmentation that must be considered in order to dcvelop a complete model.

i. *Uniform deformation*: The specimen expands at a uniform rate, with nearly uniform strain over its entire circumferenee up to a strain level ε_u^R; during this part, a dynamie eontinuum model of that incorporates inertia and continuum plasticity ean be used to determine the deformation response of the expanding ring speeimen. For the aluminum alloy and copper specimens, a strain-rate independent, power-law hardening plasticity model was found to be adequate in deseribing thc deformation of thc specimen. This aspect of the dynamic tensile loading will not bc considered further, but the details may be found in Zhang and Ravi-Chandar (2006).
ii. *Nucleation of strain localization*: At a eritieal strain ε_{cr}, uniform deformation becomes unstable and the deformation localizes into narrow regions. Sueh localization depends not only on the material properties, but also on the specimen geometry and possibly on strain rate and inertia. For example, specimens with cross-sectional aspect ratios less than six exhibit diffuse neeking typc localization while specimens with larger aspeet ratios indicate localization in the sheet-neeking or shear-banding mode. Neither the Mott model, nor the Grady model explieitly aceounts for the onset of strain localization or for its geometry-dependent differenees, but we suggest that this is indeed a crucial aspect of fragmentation in ductile materials. We will elaborate on this in the following.
iii. *Nucleation of cracks*: Eventually, craeks nueleate within the (neck or sheet mode) loealization resulting in a final failure of the specimen. Direet observation indicatcs that multiple fractures occur at different locations within the ring in sueh short timc intervals that even elastie waves are unable to eover the distanee betwecn thc fraetures. The differenees in the time and strain at onset of loealization trigger consequential differences in the onset of crack nuclcation and formation of fragments.
iv. *Mott release wave propagation*: Each fracture generates a Mott release wave that unloads its neighborhood over a distance that depends on the imposed strain rate. When rclease waves from neighboring fraetures run into eaeh other, an unloaded fragment is ereated; this aspect is exactly as observed by Mott.

We now discuss in some detail the role of eaeh of the above eomponents in the fragmentation in duetile materials.

5.4.1. Nucleation and growth of strain localization

For duetile materials, uniform plastie deformation is terminated by the onset of strain localization; this, however, is dependent on the geometry and loading conditions under

consideration. From quasi-static analysis of the uniaxial tensile stress condition, the critical strain for the diffuse necking localization is the Considère strain, $\varepsilon_{cr} = \varepsilon_N^{qs} = n$, where n is the strain hardening coefficient, while for the sheet mode necking under uniaxial tensile stress, $\varepsilon_{cr} = \varepsilon_{SN}^{qs} = 2n$, with the shear band making an angle of 54.74° with respect to the tensile axis. Since the deformation is initially uniform, the sites where localization occurs are typically considered to be defects in material properties. From the high speed images of the expanding ring experiment and from post-mortem measurements of the residual deformation on recovered fragments, Zhang and Ravi-Chandar (2006, 2008) made three main observations:

First, localization appears at numerous sites independently of each other, with a statistical distribution of the distance between such sites. A plot of the number of necks vs the distance between necks is shown in Figure 10 for three different expansion speeds in Al 6061-O specimens; the results are shown as skyline histograms of the experimental data and the best-fit Weibull distribution curves to the measured data. Similar distributions were obtained for other materials and geometries, with a Weibull modulus in the range of 1.7 to 2.7, bracketing a Rayleigh distribution. With increasing strain-rate, the distribution becomes narrower and more peaked; this is easily understood in terms of the release process. Analogous to the Mott release waves from fracture, the onset of localization limits the force carrying capacity of the section which is then communicated to the neighboring regions through release waves. Smaller regions are influenced by localization at higher strain-rates and hence the reduction in spacing between necks. At the highest strain-rates, we expect that all the inherent defects capable of triggering localization would be activated and hence the distribution corresponding to the highest strain rates could be considered to be a sampling of the defect distribution in the material. It is important to note that for a ductile material, eventual fracture can occur only at these sites and hence this distribution is an important attribute of the material, one that can be determined easily from the ring expansion test. From the high speed images, it is also clear that not all the localized necks are at the same stage of development at a given instant in time; this clearly implies that the necks were nucleated at slightly different times or strain levels spread about the critical strain level.

Second, the strain at the onset of localization is influenced by the geometry as indicated above, but also by inertial effects. Zhang and Ravi-Chandar measured the strain at the onset of localization by measuring the uniform strain away from the fractures from recovered fragments; this was accomplished by carefully measuring the width variations along the length of the recovered fragments and then using the fact that plastic deformations are volume preserving in order to extract the peak, local and average tensile strains along the length of the fragments. The variation of the strain at onset of localization, identified as the uniform strain in the recovered fragments, is shown in Figure 11. The strain at the onset of diffuse necking was found to be independent of the expanding velocity (or strain rate); however, the localization strain for sheet-mode necking increased with the expanding velocity. Through a detailed numerical simulation, this was attributed to inertial effects – specifically, the time taken for the localization to propagate across the dominant cross-sectional dimension (Zhang and Ravi-Chandar, 2008).

Third, strains measured in the expanding ring experiment – whether they are the residual uniform strains within the fragment, the average strains in the fragment or the

peak strains within the necked regions – are not appropriate measures of the strain-to-fracture. Strains within the necked regions can be as large as unity, without any indication of failure; therefore, the only meaningful strain measure that can be obtained from these experiments is the strain at the onset of localization, but as noted above, this is not a material property.

5.4.2. Nucleation of cracks

Further deformation continues to occur outside the regions of deformation localization at the uniform imposed rates, possibly moderated by the propagation of Mott-type release waves that communicate the effect of the reduction in the force carrying capacity. But, inside the localized region, the rate of straining is enhanced significantly and cracks nucleate rather quickly; the time between the onset of localization and onset of fracture of the section is typically in the range of 5 to 10 μs; we remark in passing that this is the timescale of importance in the Grady model. The fractures are indeed found to be independent nucleation of cracks within the respective localization sites. For example, for the test shown in Figure 9, the time between the first and second fractures was 0.74 μs but the sites are about 13.6 mm apart; the time between the first and third fractures was 1.3 μs and the distance is about 46 mm. Clearly, even elastic disturbances that travel at 5 mm/ μs could not have communicated between these nucleation sites. As a result the statistical distribution in the strain level at the onset of localization, strongly influences the strain level at which cracks are nucleated, and therefore the eventual fragment size distribution.

5.4.3. Mott release wave propagation and fragment size

The release wave propagation from each fracture unloads its neighboring regions as discussed earlier. Zhang and Ravi-Chandar (2006, 2008) examined this through an elastic-plastic finite element analysis. This is really an implementation of the Grady type model, but allowing the material to exhibit elastic-plastic properties. The geometry considered in the simulation is an axisymmetric rod (see Figure 12a); in the first loading step, one end of the rod is held fixed at $x_2 = 0$ and extended with a speed that varies spatially as $v(x_2,t) = \pi v_0 x_2$; this results in constant strain rate expansion of the rod that corresponds to a ring expanding radially at a speed v_0. When the strain in the bar reaches the Considère strain, ε_N^{qs}, the fixed end constraint is released for the second step in the simulation. Now, particle velocities are no longer imposed externally, but are determined by the kinetic energy at the break point and the continued plastic straining. This is very close to the experimental situation where the occurrence of the fracture terminates the current in the specimen and hence there is no further loading imposed on the specimen. The release of the constraint mimics the necking and fragmentation in the expanding ring and hence a "Mott release wave" travels down the length of the rod. The load steps are shown schematically in Figure 12a. In order to simulate possible time scales associated with the necking and fracture process, the end constraint was relaxed linearly over time τ as indicated in Figure 12b. The results of this simulation provide the time scale for the diffusion of momentum. The constitutive behavior of rod is modeled by an elastic-plastic power-law hardening model ($\sigma = k\varepsilon^n$); the finite element simulation was performed in ABAQUS Explicit Version 6.4. The length to diameter ratio of the simulation was 200

and the diameter was taken to be 0.5 mm. The variation of stress with position and time is shown in Figure 12c, corresponding to a release time $\tau = 5$ μs. The diffusion-like propagation of the Mott release process is clearly visible in this figure. The position of the release front with time is shown in Figure 12d for four different values of τ; the differences in the propagation distance at about 10 μs is on the order of a few millimeters and this is the extent of influence of the time to fracture on the fragment size.

The variation of the number of fragments with expanding velocity of the ring is shown in Figure 13a for three different materials: Al 6061-O, Al 1100-H14 and Soft Cu 101, with specimen cross-sectional aspect ratio of 2. Similar to the data of Grady and Benson shown in Figure 6, we see a linear relationship between the fragment size and the expanding velocity or strain rate. The variation of the fragment size with the expanding velocity of the ring for specimens of different cross-sectional aspect ratio is shown in Figure 13b. The fact that the $2/3^{rds}$ power relationship of Eq.(7) is not observed in all these data sets indicates that the Grady model, based on the timescale of occurrence of the fracture process, is not applicable to fragmentation in ductile materials. Specimens with larger cross-sectional area or larger aspect ratio exhibit larger absolute fragment size; we attribute this to the fact that the strain level associated with the onset of localization in these specimens is significantly higher and hence the particle velocities associated with this are higher. This implies that the propagation of the unloading diffusion process will be slower still, resulting in larger fragments for the same imposed strain-rate. This was demonstrated through numerical simulations of the localization problem by Zhang and Ravi-Chandar (2008). It can also be estimated by a very simple rescaling of Mott's estimate in Eq.(3). For the expanding ring, $\dot{\varepsilon} = v/r$; writing $\ln(r_{cr}/r_0) = \varepsilon_{cr}$, we arrive at the dependence of the Mott fragment length in terms of the strain at the onset of localization: $l_{MOTT} = 2r_0 e^{\varepsilon_{cr}} \left(2\sigma_Y \Delta\varepsilon/\rho\right)^{1/2}/v$. Finally, the fragment size distribution is shown in Figure 14 for three different materials and three different aspect ratios; these lengths are normalized by the Mott fragmentation length given above with $\Delta\varepsilon = 0.03$. Numerical estimates of Mott's statistical model and a best-fit Weibull curve are also shown in this figure.

In summary, the preponderance of experimental data on the fragmentation of ductile materials suggests that there is a statistically influenced nucleation of strain localization that precedes fracture and therefore dominates the fragmentation process. Models must account both for localization and for statistical variations in such localization before fragmentation statistics can be captured appropriately.

6. Direct Numerical Simulations of Fragmentation

The Grady model has been used by a number of investigators to model and evaluate experimental observations of fragmentation (see for example, Miller et al, 1999, Drugan, 2001, Shenoy and Kim, 2003, Zhou et al, 2006). These investigators consider the bulk material to be elastic (possibly with evolving damage) and to be connected by a network of cohesive elements that facilitate numerical representation of fragmentation; by choice of bulk properties of the material, these models are applicable only to the fragmentation of brittle materials. Specifically, *the release wave will travel at the elastic wave speed and therefore the release process is quite different from the fragmentation of ductile materials.* Miller et al, (1999) considered an elastic material (with properties of either

alumina or oil shale), with a network of cohesive zones embedded in the material to simulate the Grady model of fragmentation; furthermore, they used an exponential form of the cohesive model rather than the linear model shown in Eq.(5) and performed numerical simulations to explore fragmentation in brittle materials. First, they examined whether the simulations would be sensitive to the spacing between cohesive surfaces by performing two simulations with different mesh size. Their results indicate that with a coarse mesh, when the number of potential fracture sites (cohesive surfaces) was small, nearly every cohesive site was fractured, suggesting that the unloading wave had little effect in dictating the fragment size. On the other hand with a much more refined mesh (with about four times more cohesive surfaces), a little over 40% of the cohesive surfaces were fractured; however, the strain rates considered were quite low and it is not clear whether convergence was attained. Their simulations also indicated that the energy based estimates of the fragmentation size were about one order of magnitude higher than the fragments obtained in the simulations; they found that the distribution of fragment size was very narrow. Based on these results, they decided that a better model that incorporated microcracking-based damage within the brittle material rather than the Grady model would be more appropriate. In this simulation the velocity at the ends of the 2 mm long specimen was specified and therefore the cohesive surfaces get strained sequentially as a result of the wave propagation. In fact, Figure 4 of Miller et al (1999) shows that fragmentation occurred at about 0.3 μs, which corresponds roughly to one and a half times the transit time for elastic waves, but over an extremely short duration. This method of loading is quite different from the considerations of the Mott or Grady fragmentation models where the specimen is considered to be straining uniformly at a constant rate prior to fragmentation. Therefore one expects that the dependence of the fragment size on the strain rate and the statistical aspects of the fragmentation would be quite different. Drugan (2001) followed up on the study by Miller et al (1999) with an analytical solution of the Grady model, with an exponential cohesive model and worked out a fully dynamic solution of the problem; initial flaws are idealized in this model by considering each prospective fragment to be further decomposed into elastic and cohesive elements. Drugan's estimate of the fragment size variation with strain rate is just slightly below that of the Glenn and Chudnovsky estimate.

Shenoy and Kim (2003) extended the Miller et al, (1999) model by considering statistical variations in the cohesive model. They first decompose the total stress into a mean and fluctuating part, assume that each cohesive zone responds to the mean field, and impose the equation of compatibility that the overall strain rate is given by the sum of the mean strain in the elastic and cohesive parts. These mean fields are calculated by the method of characteristics which takes into account the full interaction between all elastic and cohesive zones. They consider a uniform probability distribution of width $2\Delta\sigma^0$ for the cohesive strength and calculate the fragment size and distribution as a function of the strain rate. They conclude that at large strain rates, the fragment size is equal to the flaw spacing and that the fragment size increases with increasing width of the probability distribution. Both of these are extremely important results that can be understood easily in terms of the Mott release process, but more importantly, used in determining statistical variability of either the strength or the strain to failure. At extremely large strain rates, the unloading wave does not travel far enough to relieve the neighboring flaws of their continued straining and hence all flaws are activated; but with a large width of

distribution of strengths, the weakest flaws will dominate, unloading the remaining segments and result in an increase in fragment size. The experimental results shown in Figure 10 regarding the distance between necks follows this same trend, even though the phenomenon is localization and not fracture.

Using an approach that is quite similar to the study of Shenoy and Kim (2003), Zhou et al, (2006) also evaluated the Grady model. These authors considered a ring with properties typical of a ceramic, modeled it as an assembly of uniformly spaced elastic and cohesive elements, and subjected it to a uniform radial velocity. In the numerical implantation, each grid point could possibly be decomposed into a double node in order to accommodate the cohesive model if the stress at that node reached the cohesive strength. The maximum cohesive stress and the fracture energy were both taken to have a random uniform distribution as in the study of Shenoy and Kim (2003). Fragmentation occurs over an extremely short duration as in the simulation of Miller et al, (1999); this is simply a result of the fast propagation speed of the unloading elastic wave. At the highest strain rates, nearly all the nodal points nucleate cohesive damage, reinforcing the conclusions of Shenoy and Kim, but at the lower loading rates, fewer fragments with spacing that is independent of mesh discretization are obtained. Furthermore, the strain-rate dependence of the fragment size is parallel to the Grady estimate at the high strain rates and is close to the Glenn and Chudnovsky estimate at low strain rates. One key result of these simulations is the extraction of the fragment size distribution and its dependence on the strain rate; this result is reproduced in Figure 15. This corresponds to material parameters: $\sigma_Y = 300\,\text{MPa}$, $\rho = 2750\,\text{kg/m}^3$, $c = 10^4\,\text{m/s}$, and $G_c = 100\,\text{J/m}^2$; these results clearly indicate that the mean fragment spacing and the width of the fragment size distribution both decrease with increasing strain rate. The fragment size distribution was shown to be well described by a Rayleigh distribution function. The similarities to the rate dependent distribution of localization sites shown in Figure 10 is striking.

We note that all of the above numerical simulations considered the Grady model in the sense that the time to develop the fracture was incorporated through a cohesive zone type representation; however, all of these models imposed an elastic response for the bulk material and hence are applicable, in principle, only to fragmentation in brittle materials. However, there are very few direct measurements on the fragmentation characteristics of brittle materials and hence no direct comparison of the predictions of these models to brittle fragmentation could be accomplished. On the other hand, many authors have addressed simulation of the expanding ring failure problem directly to explore both the onset of the necking and the evolution of fracture; we examine the main results of these simulations.

Han and Tvergaard (1994) performed a finite element analysis of the ring expansion experiment with a piecewise power law function describing the strain hardening plastic behavior of the material. Their main focus was on the onset of dynamic strain localization and hence they demonstrated multiple neck generation successfully in these simulations; small initial imperfections were found to grow into necks. Furthermore, the imperfections introduced in the simulations were shown to significantly influence the number and position of the necks. However, they did not endow the model with a capability to generate fracture and hence did not explore the fragmentation of the ring. Pandolfi et al. (1999) performed a similar numerical simulation, but now with a strain-hardening, strain-

rate dependent material model that ineluded thermal softening that is expeeted to arise from the adiabatie nature of the expanding ring test; in addition, fraeture was simulated with a cohesive surfaee model. A full three-dimensional mesh with tetrahedral elements was used, with eohesive elements at all element surfaces; this mesh breaks the symmetry of the problem and provides nuclei for the onset of neeking. These simulations mimie nearly all features observed in the expanding ring experiment, with the nuelcation of neeks, followed by evolution of the craeks along some of the eohesive surfaees and unloading or rclcase of their neighborhood. Pandolfi et al (1999) show a eomparison of the predieted number of neeks and fragments with the observations of Grady and Benson (1983) and the results appear to be in good eorrelation. These simulations are able to replieate nearly all the features observed in the experiments of Grady and Benson (1983), but it is not elear whieh aspeets of the model are essential and how this simulation ean be simplified. In partieular, how does one eontrast the role of the elastie-plastie release wave that is essential to the Mott model against the time-to-fraeture of the eohesive zone that is essential to the Grady model. Also, with inereasing strain rate, do all the eohesive zones fail as in the Miller et al (1999) simulations? Sueh a response would indieate mesh dependenee of the results and needs to be explored further.

Becker (2002) simulated the expanding ring experiment numerieally; in partieular, he was eoneerned with the experiments of Grady and Olsen (2003). In this simulation, the bulk material was eharaeterized by an elastie-plastie or a viseoplastie eonstitutive model; possible damage evolution was eaptured in the simulations through the Gurson-Tvergaard-Needleman model. Failure was modeled not through the attainment of a eritical void fraetion as is typieally done in the GTN model, but through two different eriteria, one based on material stability in the sense of Drueker, and the othcr by the appearanee of a bifureation in the form of a plane of loealized deformation in the sense of Riee (1976). We note that both these eriteria imply initiation of loealization and not neeessarily eomplete failure of the speeimen; therefore, aspeets of the time-to-fracture that are the essenee of the Grady model are not really available in this model. Thc Mott release wave, however, will travel through the speeimen from eaeh fraeture. Their results suggest that the Drucker postulate of stability is adequate for the predietion of fraeture in the expanding ring experiment. While a number of neeks and fraetures were observed in their simulations, no detailed statistieal analysis of fragment size distribution was provided.

Based on the results of their experimental observations, Zhang and Ravi-Chandar (2006) developed a very simple model for simulation of the expanding ring experiment. The model resembles the geometry of ring speeimens (r_i=15.25 mm, r_i=15.75 mm, and $w=\alpha(r_o-r_i)$) used in the experiments and ineludes randomly distributed material defeets inside. For simplieity, only a quarter segment of the ring is eonsidered with symmetry boundary eonditions imposed at planes $\theta=0$ and $\theta=\pi/2$. The material was taken exhibit an elastie-power-law-hardening plastie response. It might be useful to provide a statistieal distribution for the defeet material properties sinee this might add more realistie features to the simulation, but this was not eonsidered. The volume fraetion of the defeet region is taken arbitrarily to be 0.1% of the total volume in the model and the defeets are distributed at random. Figure 16 shows the quarter-ring models with aspeet ratio 2 and 10, where the elements with defeet are identified by the dots. The

details of the simulation can be found in Zhang and Ravi-Chandar (2008). A pulse pressure loading on the inner surface of the specimen is used to simulate the electro-magnetic driving force experienced by the ring specimens in our experiments. In response, the ring expands rapidly at a nearly constant speed. Contours of constant effective plastic strain from these simulations are displayed in Figure 17. For early times, in both simulations the plastic strain evolves nearly uniformly over the entire ring; while there are minor perturbations in the uniformity in the vicinity of the defects, the strains do not grow significantly more rapidly than the average strain rate even in the vicinity of the defects. For $\alpha = 2$, localized necking emerges at sometime between 30 and 40 about μs; the uniform strain level corresponding to this time is ~ 0.2, close to the Considère strain. For $\alpha = 10$, the localization is clearly in the form of shear bands, developing between 60 and 70 μs and oriented at an angle of $\alpha_{SN} = 35.26^{\circ}$. The uniform strain in the specimen is now around ~ 0.6, approaching the levels measured in the experiment. The nucleation of multiple necks, and the unloading engendered by the necks can be seen from the results displayed in Figure 17.

In order to continue the simulation properly beyond this level, one must impose a suitable failure criterion for the material located within the neck/localization; for simplicity, we adopted a critical strain based criterion and element deletion technique to simulate the fragmentation. The element deletion feature in ABAQUS was used to remove elements with an effective plastic strain larger than one. The main purpose of this exercise is not the simulate the fracture completely, but to evaluate its effects on neck growth and additional fracture generation. The results displayed in Figure 17 show that the necks that developed the earliest were the ones to fracture first; they also show that unloading from such fracture prevents other neighboring necks from growing further. However, if the objective is to be able to perform quantitative predictions of the fragment distribution, it is necessary to generate better models of the process of ductile failure that occurs within the necked (or shear localized) regions. This simulation indicates that direct simulation with a very simple constitutive model for the material and a simple distribution of material defects in the specimen is adequate to capture the onset of localization, and the propagation of release waves, reaffirming the applicability of Mott's ideas to the problem of fragmentation in ductile materials.

7. Conclusion

The problem of fragmentation of ductile materials has been reviewed in this paper. The pioneering models of Mott (1947) and Grady (2006) are described and contrasted. Comparing the prediction of the two models with available experimental results, we conclude that the Mott model, with suitable modifications to account for the onset of strain localization and development of fracture, is appropriate for the interpretation of fragmentation in ductile materials. In addition, the distribution of strain levels at which both strain localization and fracture occur, as determined through experiments, suggests that statistical analysis of the onset of localization, fracture and the propagation of release waves is essential in obtaining appropriate measures of the fragment size distribution. On the other hand, the Grady model, in the absence of plastic strains within the fragments, is perhaps more suitable for brittle materials. While there are numerous simulations of this model, experimental data on fragmentation of brittle materials – with the sequence of events is clearly delineated through real-time observations – is rather scarce.

Finite element methods, with a suitable model for the material constitutive behavior, are capable of modeling the response of materials to high strain rate tensile loading from small strain levels through the onset of localization and somewhat beyond. The biggest weakness in simulations lies in the inability to model the onset of fracture appropriately, whether through continuum damage models or the cohesive zone models; both of these fracture models remain promising candidates, but require detailed calibration to specific materials. However, in dynamic fragmentation problems, when the timescale of the fracture is short, even simple fracture models appear to capture the essential details of the release wave propagation appropriately.

Finally, we note that there are some very interesting experiments and models that delve into fragmentation problems in two and three dimensions, but due to space limitations, we have not explored these problems in this review.

Acknowledgement

This work was performed under a program entitled "Characterization of Nonlinear Viscoelastic and Adhesive Properties of Polyurea and Characterization of Polyurea-clad Metallic Structures" sponsored by the Office of Naval Research (ONR Grant Number N00014-06-1-0644, Program Manager: Dr. Roshdy Barsoum); this support is gratefully acknowledged.

References:

Altynova M, Hu X, and Daehn GS, (1996), Inereasecl ductility in high velocity clectromagnetie ring expansion, *Metallurgical and Materials Transactions A*, **27A**, 1837-1844.

Beeker R, (2002), Ring fragmcntation predictions using the Gurson modcl with material stability conditions as failure critcria, *International Journal of Solids and Structures*, **39**, 3555-3580.

Curran DR, Shockey DA, and Seaman L, (1973), Dynamic fracture criteria for a polycarbonate, *Journal of Applied Physics*, **44**, p.4025.

Drugan W, (2001), Dynamic fragmcntation of brittle materials: analytical meehanics-based modcls, *Journal of the Mechanics and Physics of Solids*, **49**, 1181-1208.

Glenn LA and Chudnovsky A, (1986), Strain-energy effects on dynamic fragmentation, *Journal of Applied Physics*, **59**, 1379-1380.

Grady DE, (1981), Fragmentation of solids under impulsive stress loading, *Journal of Geophysical Research*, **86**, 1047-1054.

Grady DE, (2006), **Fragmentation of Rings and Shells, The Legacy of N.F. Mott**, Springer-Verlag, Berlin-Heidelberg.

Grady DE and Bensen DA, (1983), Fragmentation of metal rings by eleetromagnetic loading, *Experimental Mechanics*, **12**, 393-400.

Grady DE and Olsen ML, (2003), A statistics and encrgy based thcory of dynamic fragmentation, *International Journal of Impact Engineering*, **29**, 293-306.

Han JB, and Tvergaard V, (1994), Effects of inertia on the necking bchavior of ring spccimcns undcr rapid radial expansion, *European Journal of Mechanics A/Solids*, **14**, 287-307

Kipp ME and Grady DE, (1985), Dynamie fraeture growth and interaetions in one dimension, *Journal of the Mechanics and Physics of Solids*, **33**, 399-415.

Lee EH, (1967), The continuum mcchanics aspects of material propcrties determination, Energeties III, (eds.) W. Mueller and M. Shaw, 85-122, Gordon and Breaeh, New York.

Miller O, Freund LB, and Needleman A, (1999), Modeling and simulation of dynamie fragmentation in brittle materials, *International Journal of Fracture*, **96**, 101-125.

Mott NF, (1947), Fragmentation of shell eases, *Proceedings of the Royal Society of London, Series A*, **189**, 300-308.

Niordson FI, (1965), A unit for testing materials at high strain rates, *Experimental Mechanics*, **5**, 23-32.

Pandolfi A, Krysl P, and Ortiz M, (1999), Finite element simulation of ring expansion and fragmentation: The capturing of length and time scales through cohesive models of fracture, *International Journal of Fracture*, **95**, 279-297.

Rice JR, (1976), The localization of plastic deformation, in Proceedings of the 14th International Congress on Theoretical and Applied Mechanics, North-Holland Publishing Company, Amsterdam, 207-220.

Rousselier G, (1987), Ductile fracture models and their potential in local approach of fracture, *Nuclear Engineering Design*, **105**, 97-111.

Shenoy V, Kim KS, (2003), Disorder effects in dynamic fragmentation of brittle materials, *Journal of the Mechanics and Physics of Solids*, **51**, 2023-2035.

Tvergaard V and Needleman A, (1984), An analysis of the cup-cone fracture in a round tensile bar, *Acta Metallurgica*, **32**, 157-167.

Walling HC, and Forrestal MJ, (1973), Elastic-plastic expansion of 6061-T6 aluminum rings, *AIAA Journal*, **11**, 1196-1197.

Wesenberg DL and Sagartz MJ, (1977) Dynamic fracture of 6061-T6 aluminum cylinders, *Journal of Applied Mechanics*, **44**, 643-646.

Zhang H and Ravi-Chandar K (2006) On the dynamics of necking and fragmentation: I. Real-time and post-mortem observations in Al 6061-O, *Int J Fracture*, **142**:183-217.

Zhang H and Ravi-Chandar K (2008) On the dynamics of necking and fragmentation: II. Effect of material properties, geometrical constraints and absolute size, *Int J Fracture*, **150**: 3-36.

Zhang H, Liechti KM, and Ravi-Chandar K (2008) On the dynamics of localization and fragmentation: III. Effect of cladding with a polymer, *Int J Fracture*, **155**:101-118.

Zhou F, Molinari JF and Ramesh KT, (2006), Analysis of the brittle fragmentation of an expanding ring, *Computational Materials Science*, **37**, 74-85.

Zhurkov SN, (1965), Kinetic concept of strength of solids. *International Journal of Fracture*, **1**, 311-323.

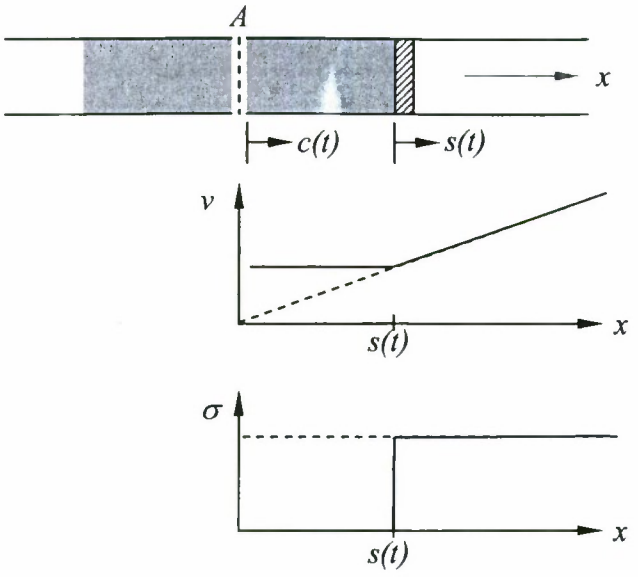

Figure 1. Mott's Fragmentation Model

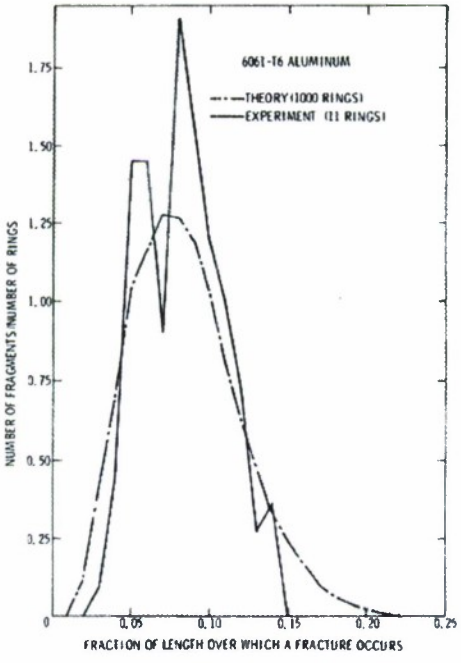

Figure 2. Mott distribution of fragment size; calculations and data from (reproduced from Wesenberg and Sagartz, 1977)

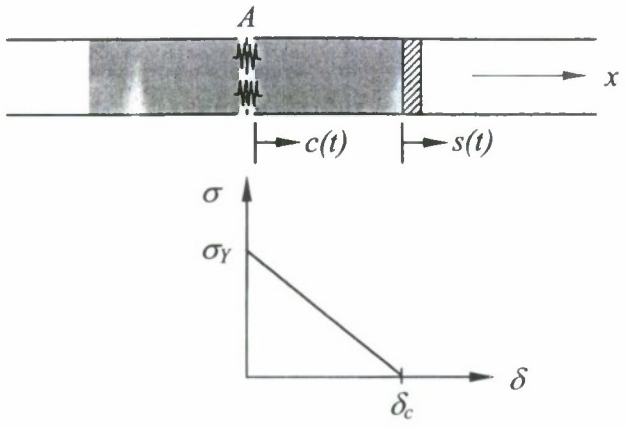

Figure 3. Grady's fragmentation model

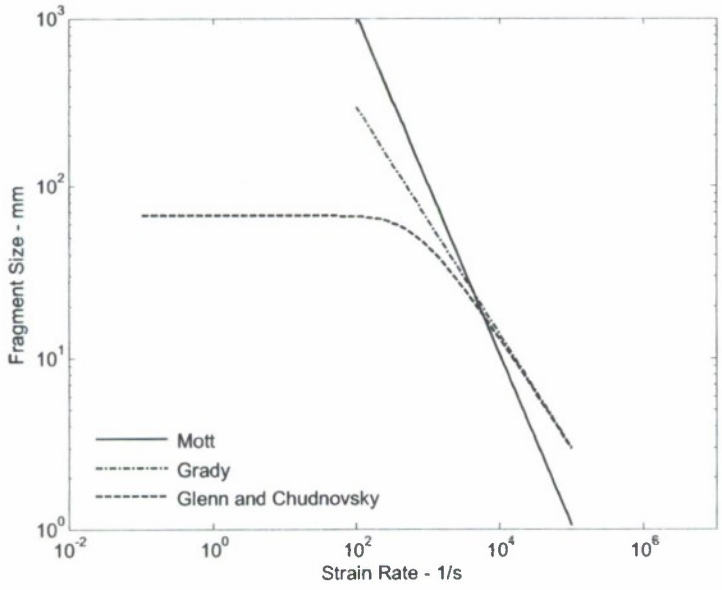

Figure 4. Dependence of the fragmentation size on the strain rate; predictions from the Mott, Grady, and Glenn and Chudnovsky models are shown.

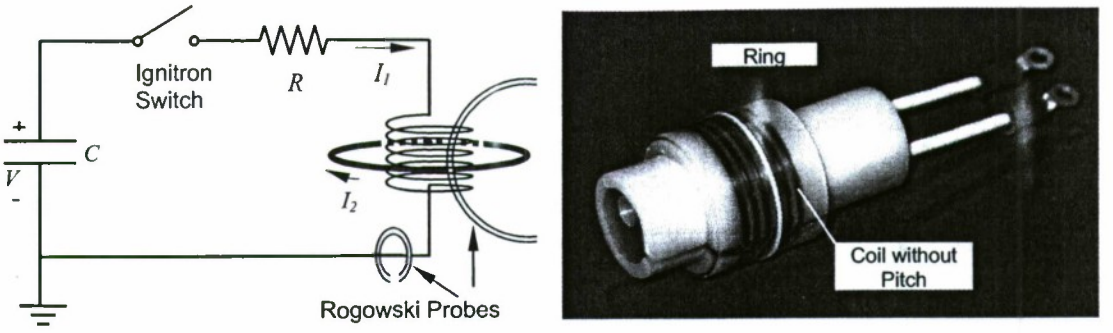

Figure 5. (a) Schcmatic diagram of the expanding ring expcriment; (b) Photograph of coil and ring spccimcn uscd by Zhang and Ravi-Chandar, 2006.

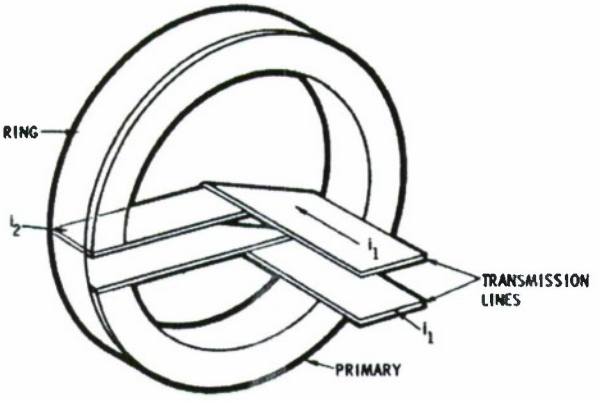

Figure 6. Schematic diagram of the electromagnetic tubc expansion arrangcment (Reproduced from Walling and Forrestal, 1973).

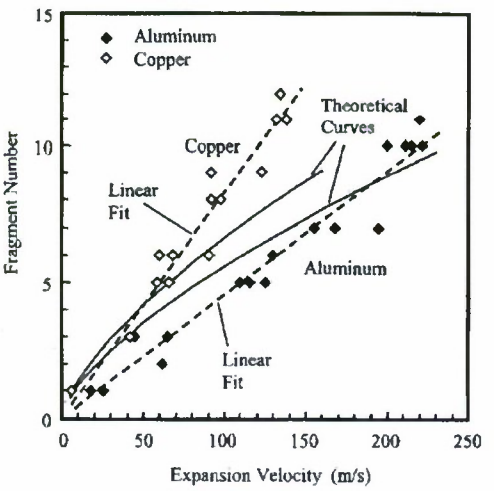

Figure 7. Variation of the number of fragments with ring expansion velocity (reproduced from Grady, 2006)

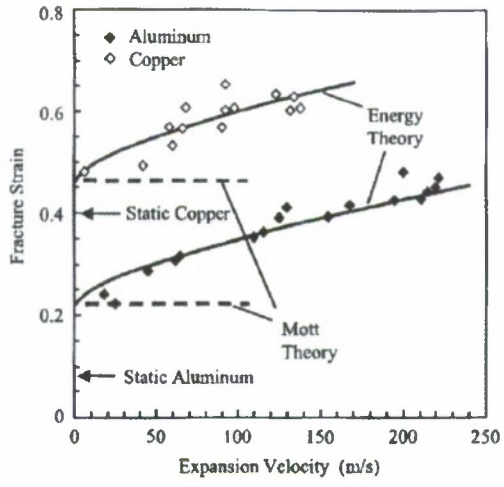

Figure 8. Variation of the fracture strain with ring expansion velocity (reproduced from Grady, 2006)

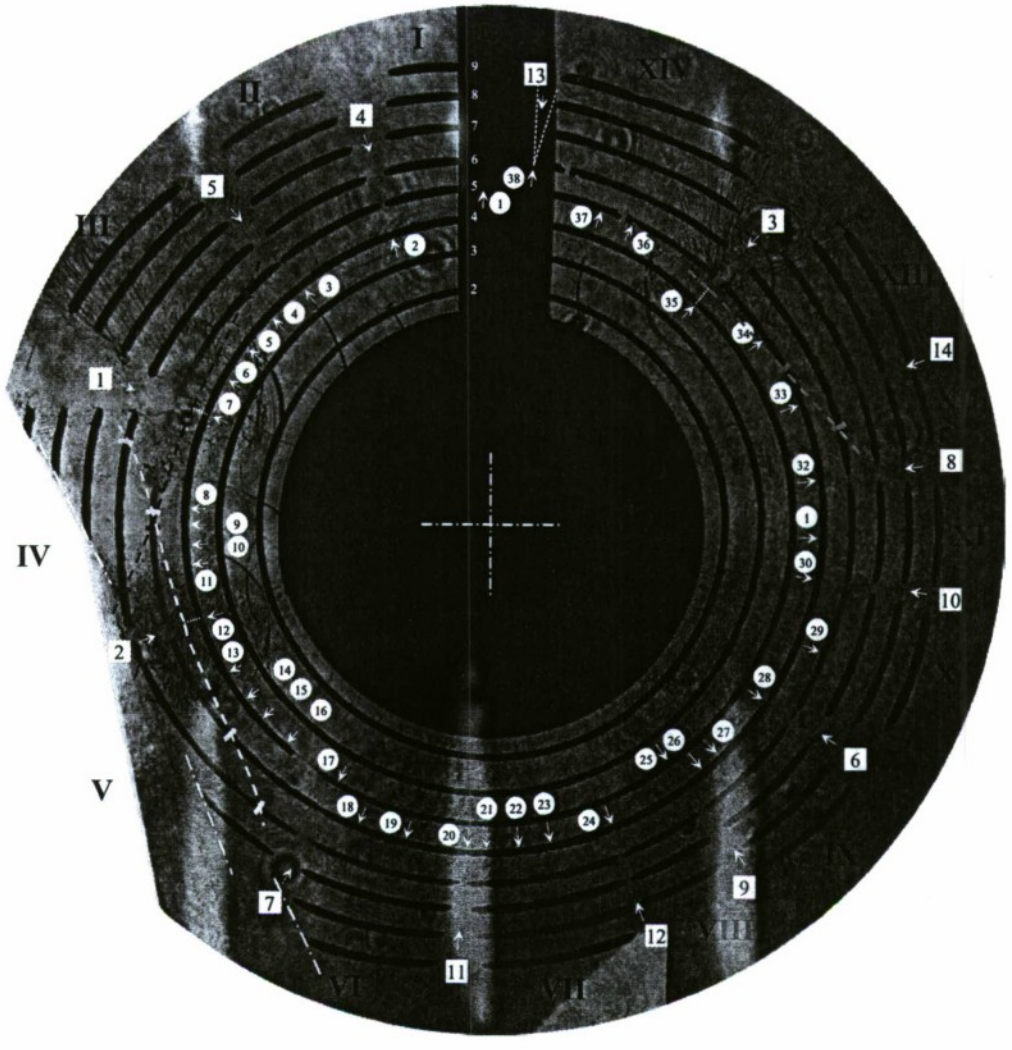

Figure 9. Composite image illustrating the sequence of events in an expanding ring experiment. The locations of necks are indicated by the numbers inside circles. The positions of the fractures are indicated in order of appearance by the numbers inside the white squares. The dotted lines (red, green and yellow) indicate the Mott release waves from the first three fractures (reproduced from Zhang and Ravi-Chandar, 2006)

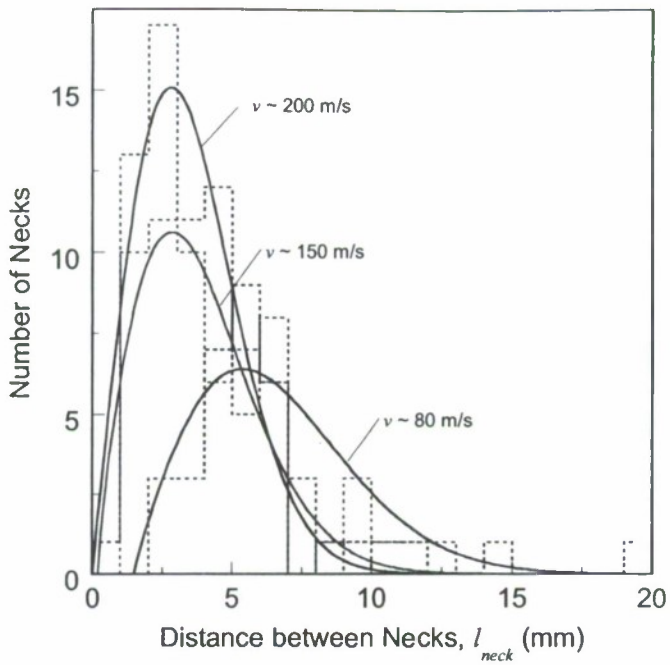

Figure 10. Distribution of distance between necks corresponding to different strain rates.

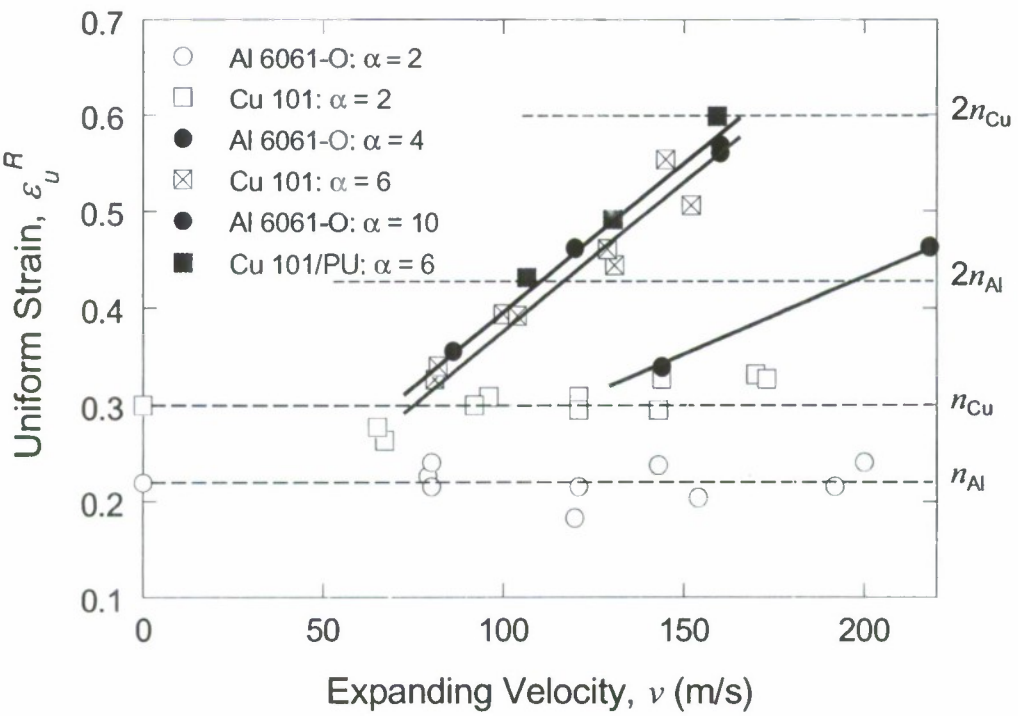

Figure 11. Dependence of the strain at onset of localization for different materials, geometries and aspect ratios.

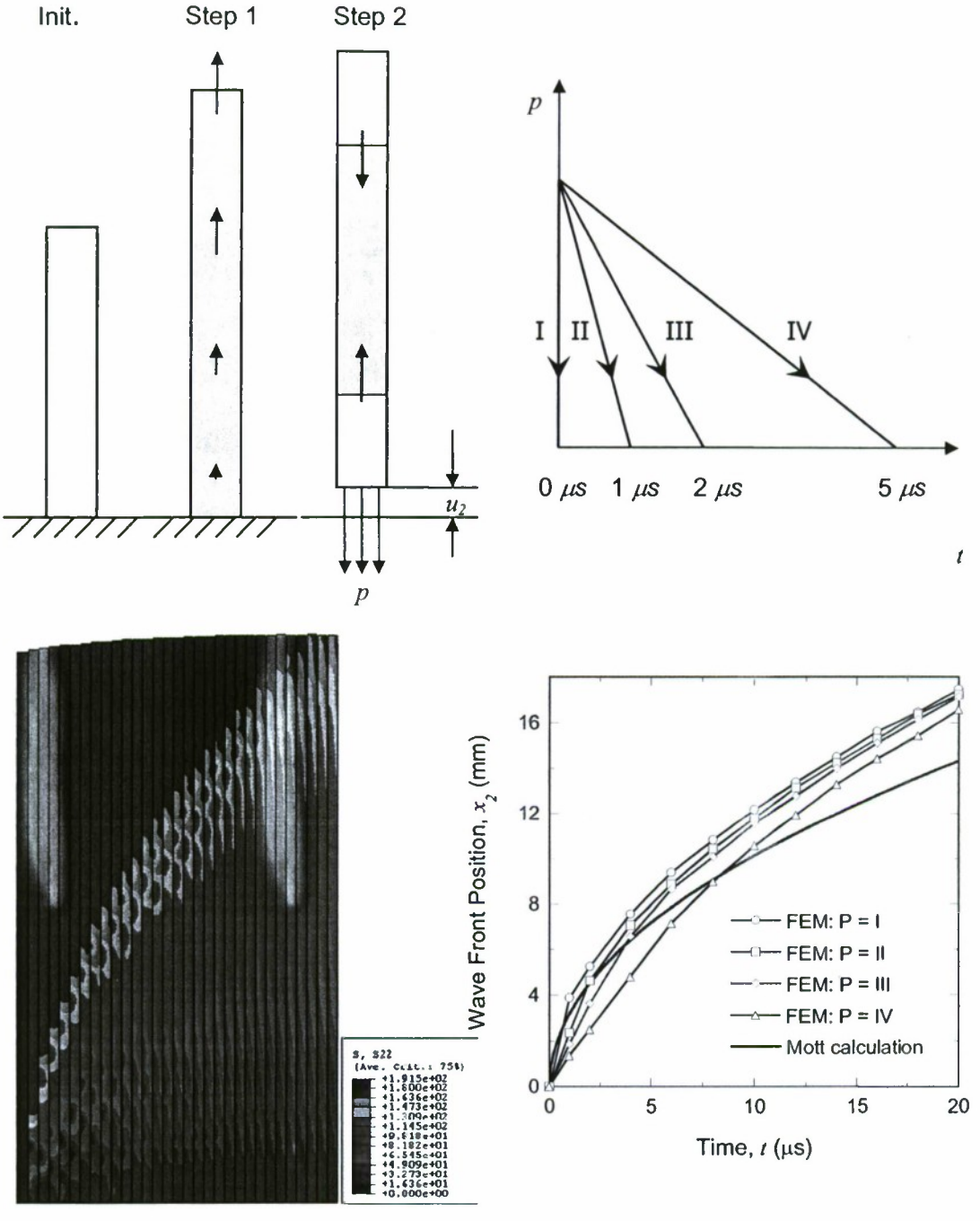

Figure 12. Elastic-plastic model of the Mott release process

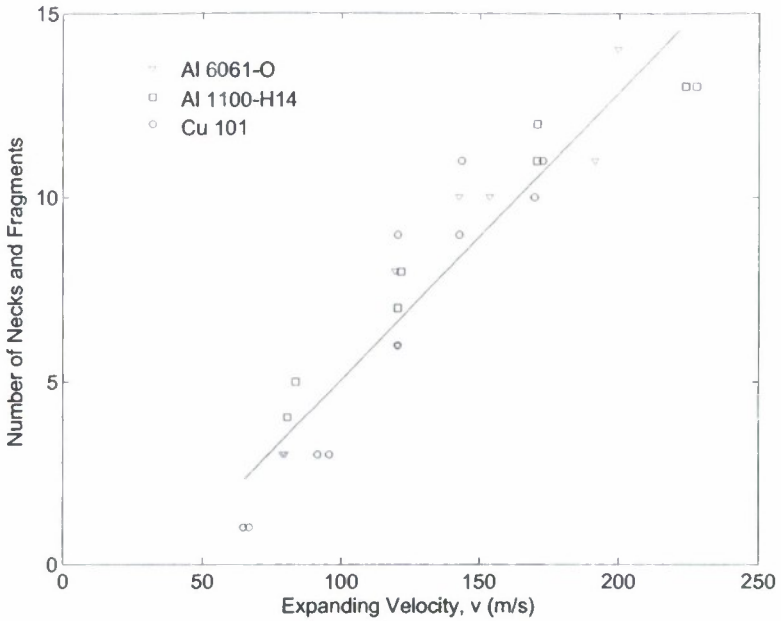

(a)

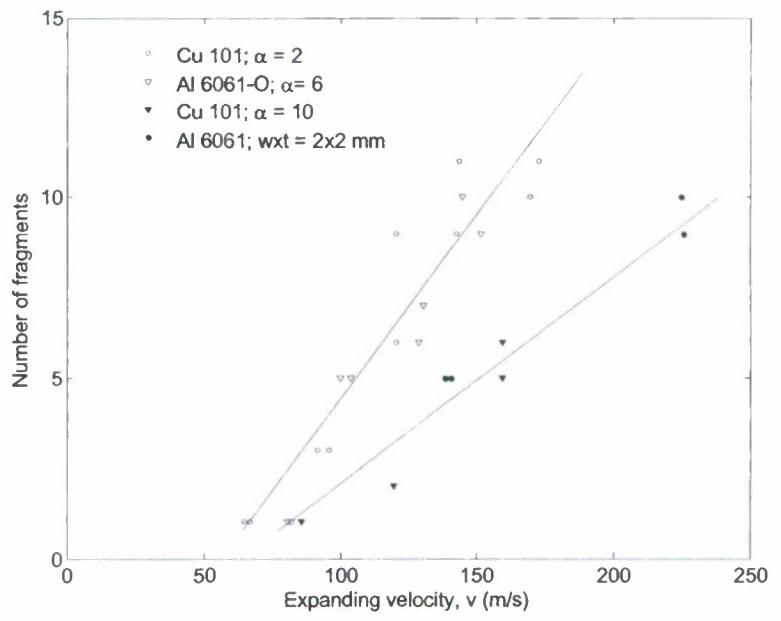

(b)

Figure 13. Variation of the number of fragments with expanding velocity for (a) three different materials with identical dimensions and (b) for specimens with different dimensions and aspect ratios.

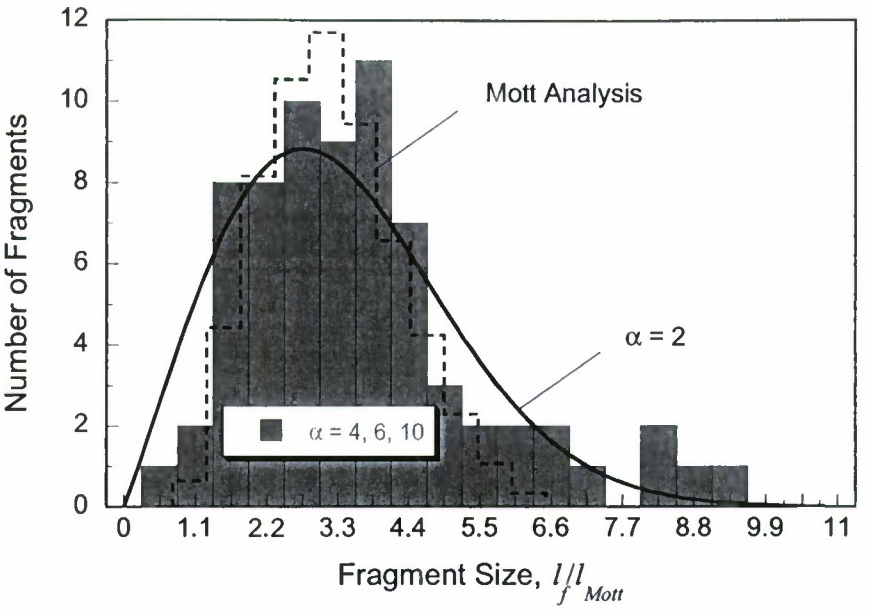

Figure 14. Distribution of the fragment size normalized by the Mott scaling length l_{Mott}, defined in Eq.**Error! Reference source not found.** for Cu 101 with $\alpha = 6$, and Al 6061-O with $\alpha = 4$ and $\alpha = 10$. The solid line is a Rayleigh distribution fit and the dashed line is the Mott statistical estimate.

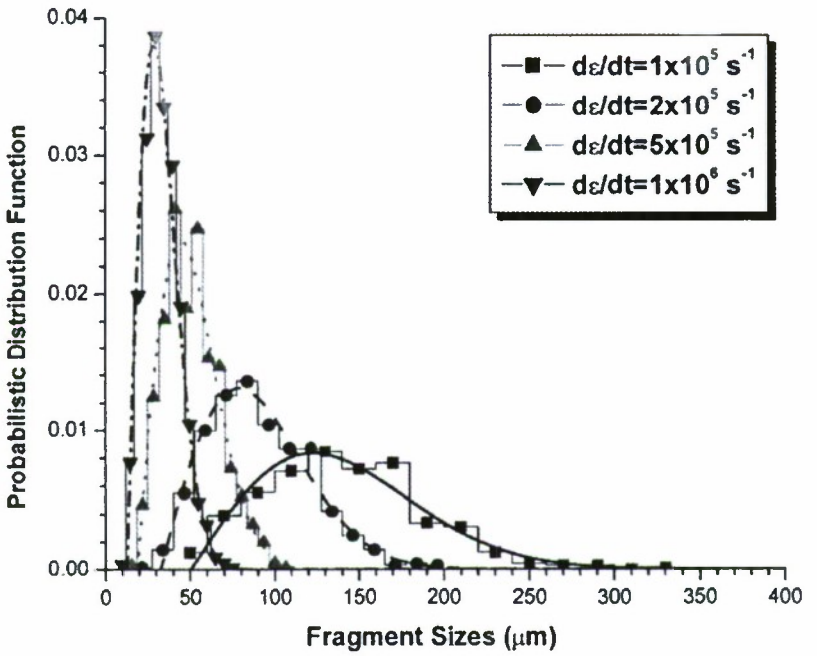

Figure 15. Probability distribution function for fragment sizes at different expansion rates (reproduced from Zhou et al, 2006).

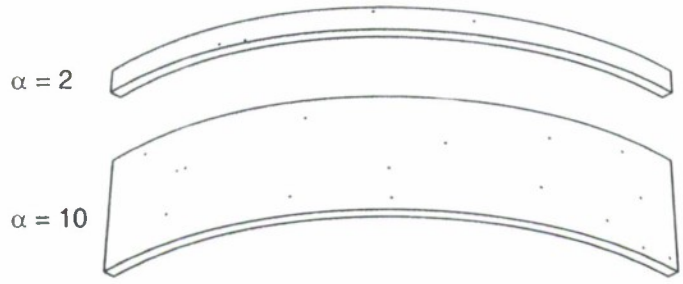

Figure 16. Quarter ring models of aspect ratio: 2 and 5, with material defects randomly distributed in the model (indicated by the red dots).

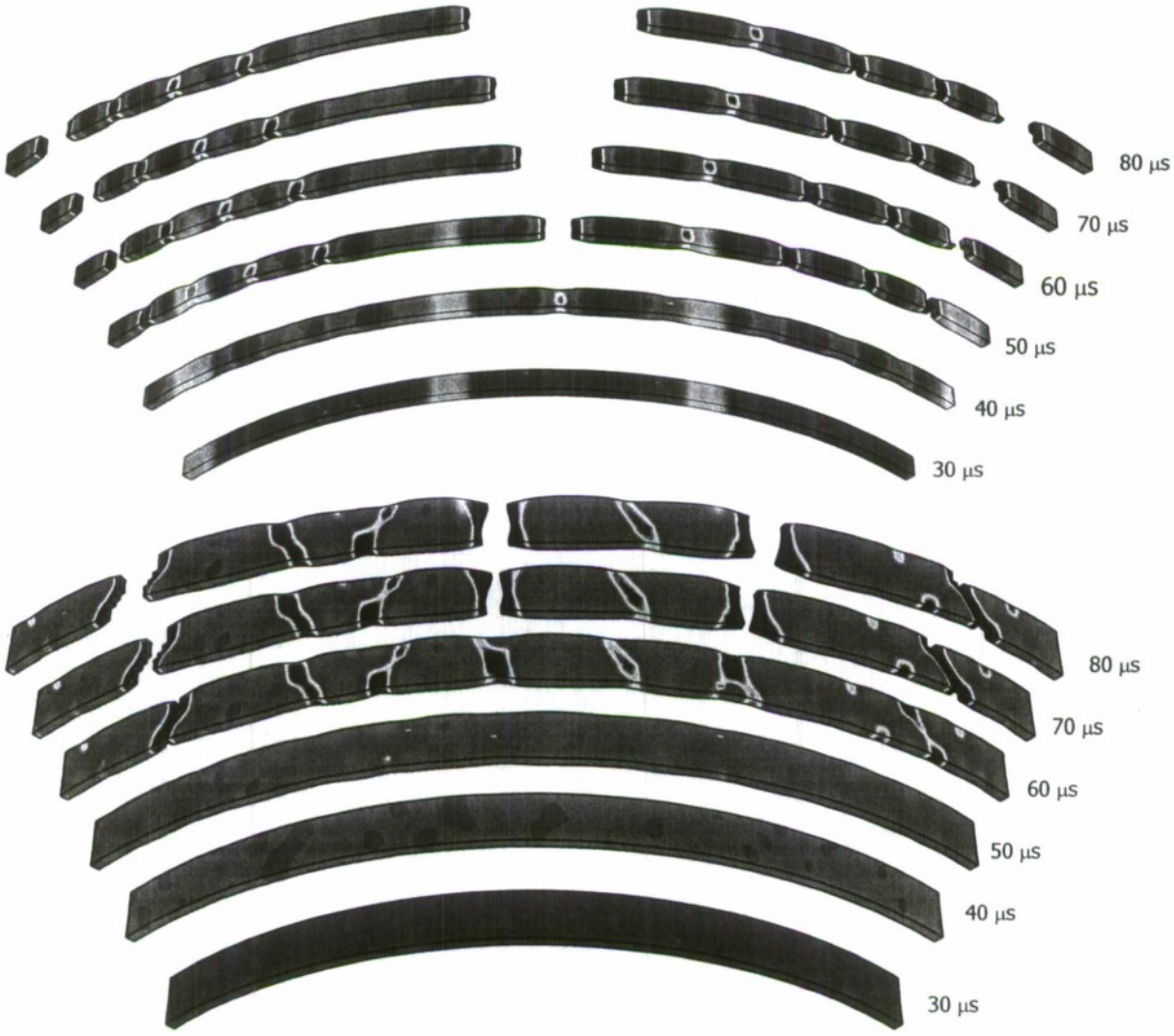

Figure 17. Emergence of necking and fragmentation of rings with aspect ratio 2 and 5. Defects were distributed randomly, with a concentration of 0.01% by volume; the defects have a reduced yield strength of 20 MPa and do not exhibit strain hardening.

APPENDIX D

Direct extraction of rate-dependent traction-separation laws for polyurea/steel interfaces

Yong Zhu, Kenneth M. Liechti, K. Ravi-Chandar

International Journal of Solids and Structures, **46**, 31-51.

International Journal of Solids and Structures 46 (2009) 31–51

Contents lists available at ScienceDirect

International Journal of Solids and Structures

journal homepage: www.elsevier.com/locate/ijsolstr

Direct extraction of rate-dependent traction–separation laws for polyurea/steel interfaces

Yong Zhu [a], Kenneth M. Liechti [b,*], K. Ravi-Chandar [b]

[a] Department of Mechanical and Aerospace Engineering, North Carolina State University, Raleigh, NC 27695, USA
[b] Research Center for the Mechanics of Solids, Structures and Materials, Aerospace Engineering and Engineering Mechanics, The University of Texas, Austin, TX 78712, USA

ARTICLE INFO

Article history:
Received 19 November 2007
Received in revised form 12 July 2008
Available online 28 August 2008

Keywords:
Polyurea
Adhesion
Interfacial fracture
Cohesive zone model
Traction–separation law

ABSTRACT

Polyurea coatings on steel form tough, flexible and chemically resistant surfaces, making them ideal for a variety of applications. An important issue for polyurea coatings in some cases is their adhesion to steel under various loading conditions in aggressive environments. In this paper, adhesion was examined using steel/polyurea/steel sandwich specimens and interfacial fracture mechanics. The mode 1 and mode 2 interfacial fracture behaviors were characterized by two independent traction–separation laws. The traction–separation laws were measured directly by recording the *J*-integral and the end-opening displacement in the directions normal and tangential to the steel/polyurea interface. In each case, the traction was initially nonzero, increased with increasing separation, reached its peak value and then decreased with further increasing opening. Strong rate-dependent effects were found for both modes of fracture and were attributed to the interfacial behavior. Porosity introduced during the processing of the polyurea affected the traction–separation laws and associated fracture mechanisms.

1. Introduction

Polyurea-based coatings are usually two-component systems that are made up of an isocyanate and a resin blend consisting of only amine terminated components. Polyurea coatings offer unique advantages in both manufacturing (they can be sprayed on and cure rapidly even at freezing temperatures) and properties (high deformability, high abrasive resistance, insensitivity to solvents, and low or zero volatile organic compounds) (Takas, 2004). These features are superior to most, if not all the other coatings currently available, which has allowed polyurea coatings to grow rapidly in a variety of applications. A critical issue for the reliability of polyurea coatings is their adhesion to substrates. However, to the best of our knowledge, very little, if any, data have been obtained for the adhesion of polyurea coatings, particularly in the form of traction–separation laws.

A practical approach for characterizing the adhesion of polymer coatings to metal substrates is to use sandwich specimens, which can be analyzed using interfacial linear elastic fracture mechanics (LEFM) concepts (Hutchinson and Suo, 1992). However, there can be limitations to the use of LEFM in sandwich structures. The first is that the assumed stress fields are not rigorously correct, for example, in the case of large-scale plasticity or in the case of very thin layers where the *K*-dominant field cannot develop (Wang, 1983). The second is that some joints may not have macroscopic defects large enough to be considered cracks for the purpose of fracture mechanics (Li et al., 2005b). These issues can compromise the utility of LEFM and alternative approaches must be sought. Cohesive zone modeling is one such approach. The key concept of cohesive zone

* Corresponding author. Fax: +1 512 471 5500.
E-mail address: kml@mail.utexas.edu (K.M. Liechti).

0020-7683/$ - see front matter © 2008 Elsevier Ltd. All rights reserved.
doi:10.1016/j.ijsolstr.2008.08.019

modeling is that the failure process zone can be described by a traction–separation law; more specifically, the cohesive traction, $\sigma(\delta)$, can vary along the failure process zone, but only depends on the local opening, δ.

Cohesive zone models are built upon the concepts first discussed by Dugdale (1960) and Barenblatt (1962). The key is the introduction of a second fracture parameter, e.g., the cohesive strength, in addition to the fracture toughness. This cohesive strength relates the toughness to the critical crack-tip opening required for crack propagation. Recently cohesive zone modeling has been applied to solve interfacial fracture problems. Needleman (1987) and Needleman (1990) proposed a cohesive zone model for analyzing void nucleation, growth and coalescence. In this model, the plane of the crack is held by a spring-like entity possessing a built-in traction–separation law. Extension of this model to analyzing interface debonding under mixed-mode conditions was provided by Tvergaard and Hutchinson (1993, 1994). In their analyses, fracture occurs when the normal and the tangential displacement at the tip of the cohesive zone fulfill a critical vectorial crack opening displacement (Liechti and Knauss, 1982). More recently, Yang and Thouless (2001) proposed a modified criterion for mixed-mode interfacial fracture, in which fracture occurs when the mode 1 and mode 2 energy release rates for the cohesive zone reach a critical value. Nevertheless, in both criteria, with independently characterized mode 1 and mode 2 traction–separation laws available, mixed-mode problems with a range of fracture mode-mixes can be fully solved.

Cohesive zone modeling has been used to examine a wide spectrum of interface problems, such as glass/epoxy interfacial fracture and adhesion (Swadener and Liechti, 1998), delamination in stitched composites (Massabo et al., 1998), plastic dissipation in thin debonding films (Shirani and Liechti, 1998), crack nucleation at bi-material corners (Mohammed and Liechti, 2000) and peeling (Kim and Aravas, 1988; Yang et al., 2000; Kinloch et al., 1994; Wei and Hutchinson, 1998). However, these models did not consider rate dependence in interface properties. Recently, rate-dependent traction–separation laws were measured for quasi-static debonding at polyurethane/steel (Sorensen, 2002) and rubber/steel (Liechti and Wu, 2001) interfaces. In addition, rate-dependent traction–separation laws have been determined for homogeneous polymeric materials (Ivankovic et al., 2004; Landis et al., 2000) considering the time-dependence of the damage growth processes and the nonlinear viscoelastic response of ligaments in the fracture process zone.

Most approaches for measuring traction–separation laws rely on iterative comparisons between measured properties [e.g., an R-curve (Flinn et al., 1993), a crack opening profile (Cox and Marshall, 1991; Mello and Liechti, 2006) or a load–displacement curve (Li et al., 2005a)] with predictions based on assumed traction–separation laws. Two methods that yield the traction–separation law directly from experiments without such comparison are available. One is through direct tension or shear experiments (Cotterell and Mai, 1996; Pandya and Williams, 2000). However, in these experiments, the damage evolution across the width of the specimen must be uniform, which is usually difficult to achieve. In the second approach, the cohesive law is derived from simultaneous measurements of the J-integral and the end-opening (both normal and shear) of the cohesive zone. This has been successfully employed in the extraction of traction–separation laws for cementitious components (Li et al., 1987), adhesive bonds (Sorensen, 2002) and fiber-reinforced composites (Sorensen and Jacobsen, 2003). Both direct methods will be employed in the present work, although the focus is on the second one.

The main objective of the present paper is to obtain the traction–separation laws of a polyurea/steel interface in mode 1 and mode 2 directly from experiments using sandwich specimens. We begin by describing the experimental methods that were used for characterizing the mechanical behavior of polyurea and fracture at polyurea/steel interfaces. Next, we report on the tensile and shear behaviors of bulk polyurea prior to the experimental identification of mode 1 and mode 2 traction–separation laws for polyurea/steel interfaces at different loading rates. The paper closes with a discussion of the rate dependence of polyurea/steel interfaces and the effects of the manufacturing process on the interfacial failure mechanisms.

2. Experimental

The uniaxial tension and shear properties of bulk polyurea were measured in unconfined and sandwich configurations. The latter were also used in the fracture experiments in modes 1 and 2 for determining the traction–separation laws for the polyurea/steel interface. In this section, specimens and experimental procedures for all these experiments are described.

2.1. Specimen preparation

The specimens for measuring the unconfined tensile behavior of the polyurea were obtained from thin films. In this case, the polyurea fluid was sprayed on top of a Teflon block to form a thin film with thickness of 0.7 ± 0.1 mm. After the film was peeled from the Teflon block, tensile coupons were cut from the film using a stamp that produced the geometry shown in Fig. 1(a) with $l = 50.4$ mm and $w = 2.1$ mm.

The specimens for unconfined shear testing of the polyurea were cut from a thick block. The polyurea block was sprayed in a mold with Teflon bottom and sidewalls. The butterfly-shaped specimens were loaded using the Arcan apparatus (Popelar and Liechti, 1997; Arcan et al., 1978), as shown in Fig. 1(b). The gauge length l, width w and thickness B of the specimens were 16.1, 10.2, and 2.5 mm, respectively.

Steel/polyurea/steel sandwiches were used for examining the confined stress–strain response in tension and shear and determining the mode 1 and 2 traction–separation laws. The specimens were processed as follows: cold rolled steel adherends (Westbrook Metals, Austin, TX) were sandblasted and degreased with acetone prior to spraying. The polyurea formulation was developed by Texas Research International, Inc. (Austin, TX). The polyurea fluid, coming from two separate

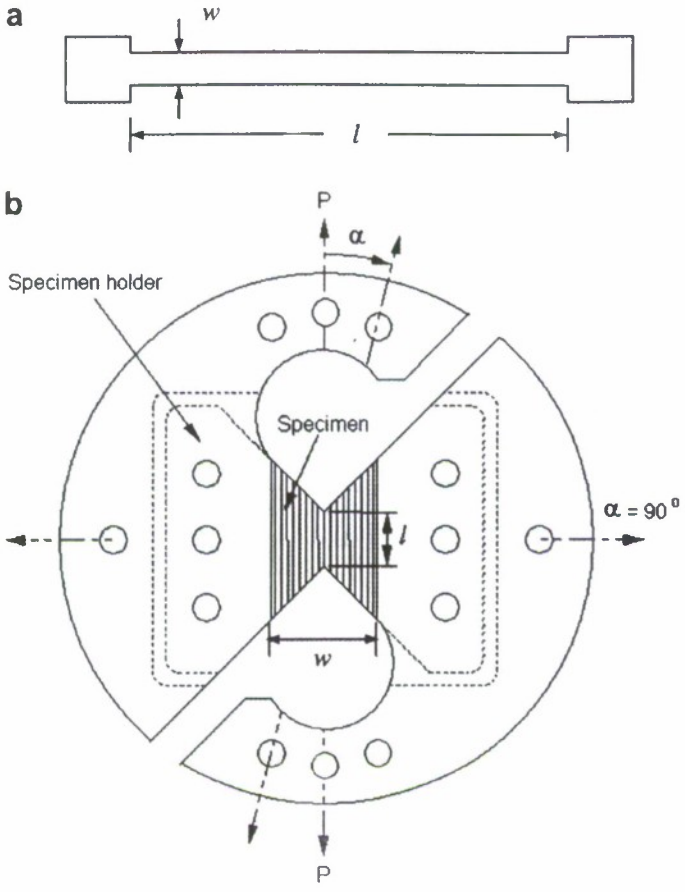

Fig. 1. (a) Tensile coupon for bulk polyurea, with a length of 50.8 mm, a width of 2.1 mm and a thickness of 0.7 mm. (b) Butterfly-shaped shear specimens for bulk polyurea, with a gauge length of 16.1 mm, a width of 10.2 mm and a thickness of 2.5 mm loaded in an Arcan apparatus.

reservoirs of resin and hardener, were combined in a single jet and sprayed on top of two steel plates that were 150 mm square by 4.76 mm thick. Immediately after the spraying was completed, the plates were joined and held together by four strong clamps at the corners. This process had to be accomplished within 10 s, the approximate reaction time. The adhesive thickness was basically controlled by the clamp pressure which gave rise to a uniform polyurea thickness of 0.7 ± 0.05 mm throughout the entire sandwich. The sandwich plates were left for at least 10 days for hardening at room temperature in an ambient environment before being subsequently machined into specimens.

2.2. Test methods

The test method for the uniaxial tension experiments was quite standard. Details of the apparatus and experimental procedures for Arcan testing in unconfined shear using the butterfly specimens have been given elsewhere (Popelar and Liechti, 1997; Arcan et al., 1978).

The double cantilever beam (DCB) configuration was used to determine the mode 1 traction–separation laws. The specimen geometry and the loading are shown in Fig. 2(a). A preexisting crack in the middle of the polyurea layer was cut using a sharp razor blade. It turned out that the fracture process zone in these experiments was large (Parmigiani and Thouless, 2007). Consequently, it was necessary to include (Högberg et al., 2007) the contribution of the rotation near the crack front to the J-integral through

$$J = 12\frac{(Pa)^2}{Eh^3} + P(w_1' - w_2'). \tag{1}$$

where P is the applied load per unit width, a is the crack length, h is the adherend thickness, and E is the elastic modulus of the steel adherends, and w_1' and w_2' are, respectively, the rotations of the upper and lower adherends at the crack tip.

The J-integral approach can be applied if the materials possess an elastic stress–strain behavior. This was the case for steel adherends which were loaded below their yield strength (~500 MPa). The polyurea is an elastomer, which was considered to be a nonlinear elastic material. Evaluating J-integral along a path just outside of the failure process zone yields

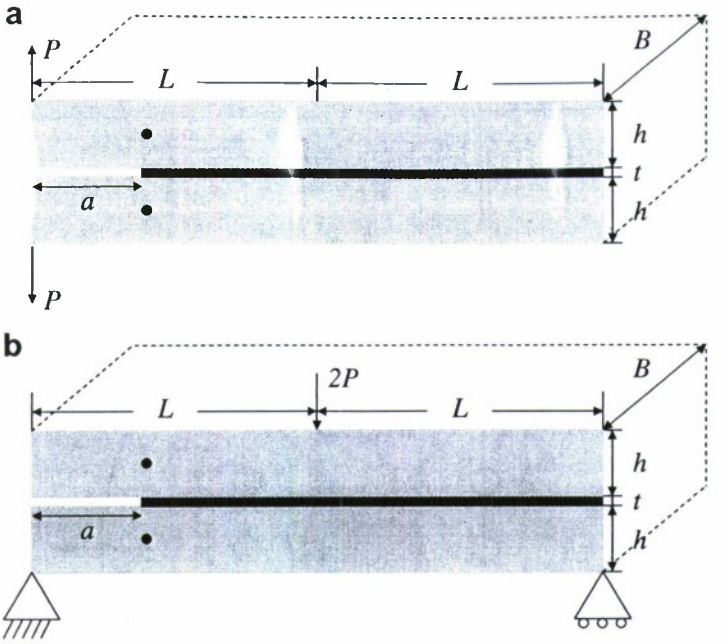

Fig. 2. Schematics of (a) the DCB test configuration and specimen (L = 75 mm, B = 10 mm, and a ranges from 25 to 70 mm) and (b) the ENF test configuration and specimen (L = 75 mm, B = 10 mm, and a ranges from 15 to 30 mm). For both configurations h = 4.76 mm and t = 0.7 mm.

$$J = \int_0^{\tilde{\delta}_n} \sigma(\delta_n) \mathrm{d}\delta_n, \tag{2}$$

where δ_n and $\tilde{\delta}_n$ are the normal opening and the normal end-opening of the cohesive zone, respectively, and σ is the normal traction. J reaches a steady-state value, J_{SS}, when $\tilde{\delta}_n$ attains δ_{nc}, the critical normal end-opening. The entire failure process zone is described by the cohesive law. Due to its path independence, the J-integral in Eq. (2) is equal to that obtained by Eq. (1). The normal end-opening $\tilde{\delta}_n$ can be recorded in digital images, thus differentiation of Eq. (2) with respect to $\tilde{\delta}_n$ gives

$$\sigma(\tilde{\delta}_n) = \frac{\partial J}{\partial \tilde{\delta}_n}. \tag{3}$$

Thus, the mode 1 traction–separation law can be obtained by simultaneously measuring the J-integral and the normal end-opening $\tilde{\delta}_n$.

For mode 2 fracture, two configurations were considered: end-notched flexure (ENF) and modified Arcan. The ENF experiments were performed in a three-point bending configuration. The specimen geometry and the load introduction for ENF are shown in Fig. 2(b). The J-integral is given by Leffler et al. (2007)

$$J \approx \frac{9}{16}\frac{(Pa)^2}{Eh^3} + \frac{3}{8}\frac{Pv_0}{h}, \tag{4}$$

where P is the applied load per unit width, a is the crack length, h is the adherend thickness, and E is the elastic modulus of the steel adherends, and v_0 is the shear displacement between the top and bottom adherend/polyurea interfaces at the crack tip. Similar to mode 1 fracture, evaluating J-integral along a path just outside of the failure process zone yields

$$J = \int_0^{\tilde{\delta}_t} \tau(\delta_t) \mathrm{d}\delta_t, \tag{5}$$

where δ_t and $\tilde{\delta}_t$ are the tangential opening and the tangential end-opening of the cohesive zone, respectively, and τ is the tangential traction. Differentiation of Eq. (5) with respect to $\tilde{\delta}_t$ gives

$$\tau(\tilde{\delta}_t) = \frac{\partial J}{\partial \tilde{\delta}_t}. \tag{6}$$

However, the ENF configuration can sometimes cause compression of and friction on the crack faces (Carlsson et al., 1986). This problem was quite severe for our case, as will be shown in detail later. Although some methods to reduce the frictional effects have been proposed, such as incorporation of a small steel wire as a spacer between the adherends (Li et al., 2006), the improvement remains unclear. As a result, a modified Arcan shear mode testing technique (Banks-Sills and Sherman, 1991) was considered here as an alternative.

The loading apparatus and the specimen geometry for the modified Arcan are shown in Fig. 3. A circular grip plate with a square window in the center was cut into half along the diameter. A sandwich specimen was screwed into couplings which

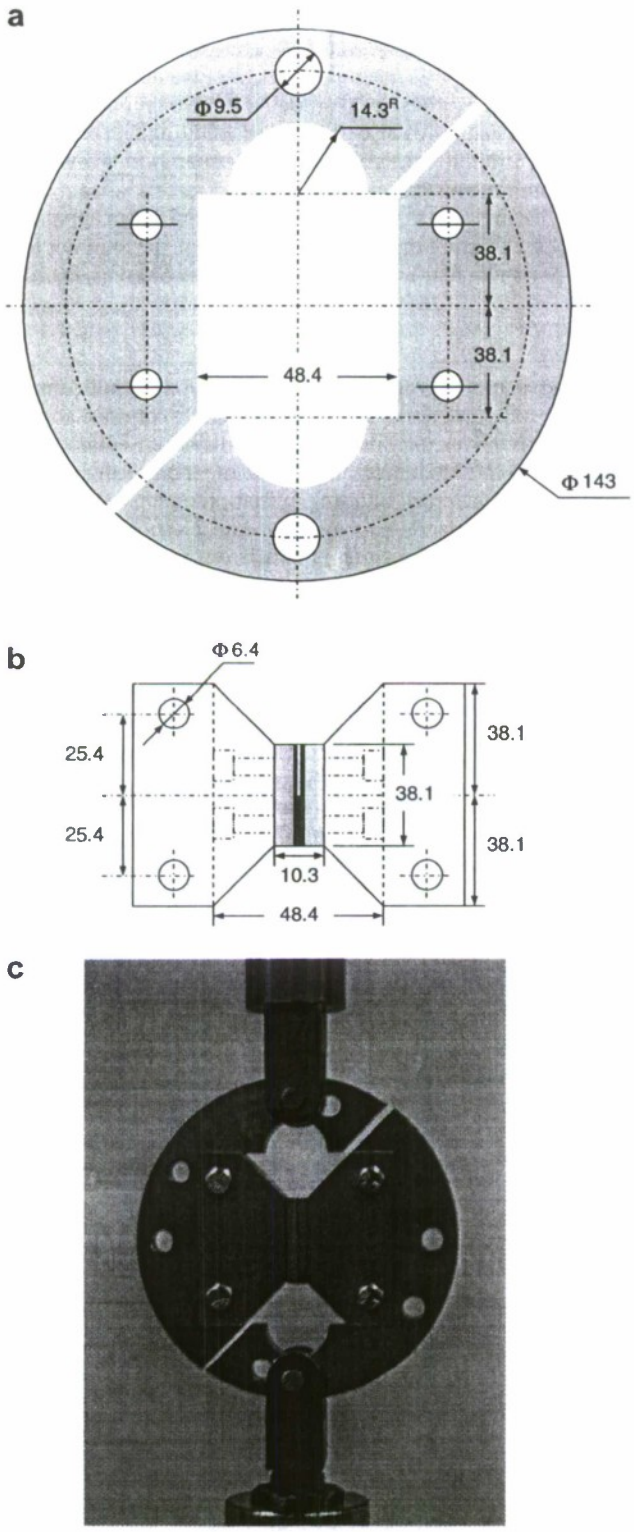

Fig. 3. The grips and specimen for the modified Arcan test for shear fracture, including (a) the circular grips, (b) the couplings with specimen attached, and (c) an optical image of the entire setup. All dimensions are in millimeters.

were attached to the two semi-circular grip plates. Schematics of the circular grip plate and the loading coupling with the specimen, and an optical image of the entire setup are shown in Fig. 3(a), (b), and (c), respectively. The J-integral for the modified Arcan specimen is given (Banks-Sills and Sherman, 1991) by

$$J \approx \eta \frac{A}{Bb}, \tag{7}$$

where η is a constant, A is the area under the load–displacement curve, B is the specimen out-of-plane width, and b is the length of the uncracked ligament. Note that here A is the area under the load–local displacement curve, where the local displacement is the shear displacement across the adhesive layer. Using finite element analysis, it was determined that $\eta = 0.9$ for homogenous aluminum specimens. This value was also used in our study, again considering the path independence of the J-integral for the sandwich configuration. Similarly, the shear traction–separation law was then obtained by recording the J-integral and the shear displacement simultaneously.

The confined tensile and shear experiments also made use of the modified Arcan apparatus just described. The specimens were identical to those used in the mode 2 fracture experiments except that they did not have any cracks. For confined tension, the polyurea/steel interface was perpendicular to the loading direction whereas, for confined shear, the angle was zero.

2.3. Test procedures

All the experiments were conducted at room temperature using a servo hydraulic materials testing system under constant crosshead speed. In all the fracture experiments the end-opening of the cohesive zone was monitored by a CCD camera in real time, which was synchronized with the acquisition of load and displacement data, as shown in Fig. 4. The image resolution is 2 μm (corresponding to half pixel in each image). This real-time monitoring scheme can record the entire time and spatial history of the evolution of fracture, e.g., crack blunting, initiation of separation, and crack propagation. Correlation between the recorded fracture events and the load–displacement data provides a means for quantitative understanding of the fracture process. Another advantage of CCD imaging is that it records the exact end-opening of the cohesive zone. The opening comprises both bulk deformation of the adhesive layer and the separation across the cohesive zone. In other methods where, for example, extensometers are used (Sorensen, 2002), the measured end-opening includes part of the adherend deformation although this deformation is often assumed to be small.

In addition, CCD imaging was required for accurate measurements of displacement and strain in both the original and modified Arcan experiments. The displacement imposed on the specimen is not equal to the crosshead displacement, due to machine and grip compliance. With the CCD imaging, the local displacement and thus strain can be directly obtained. Both the displacements measured from CCD imaging and the crosshead movement are plotted in Fig. 5 for two cases: confined tension and confined shear on the sandwich specimens, respectively. As can be seen, the strain determined from the crosshead displacement is inaccurate especially at the beginning of the experiment when the displacements are small. The differences were particularly noticeable under tensile loading and reliance on crosshead displacements would clearly lead to low measurements of moduli. It should be noted that all the image analyses were conducted after the experiment.

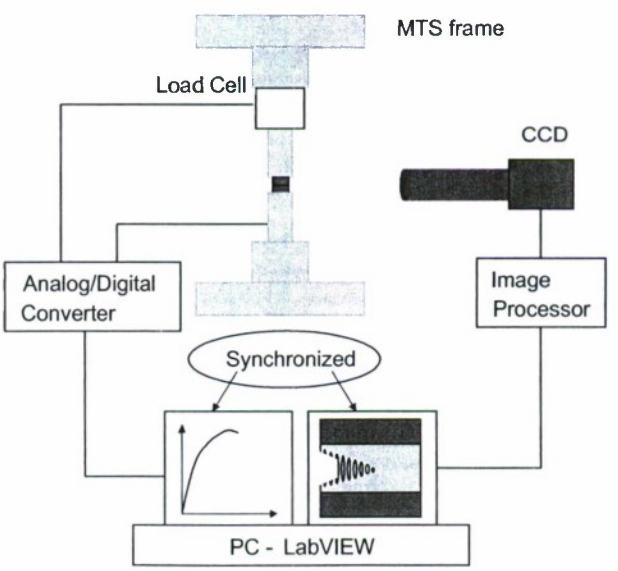

Fig. 4. A schematic of the apparatus shows both data and image acquisition systems.

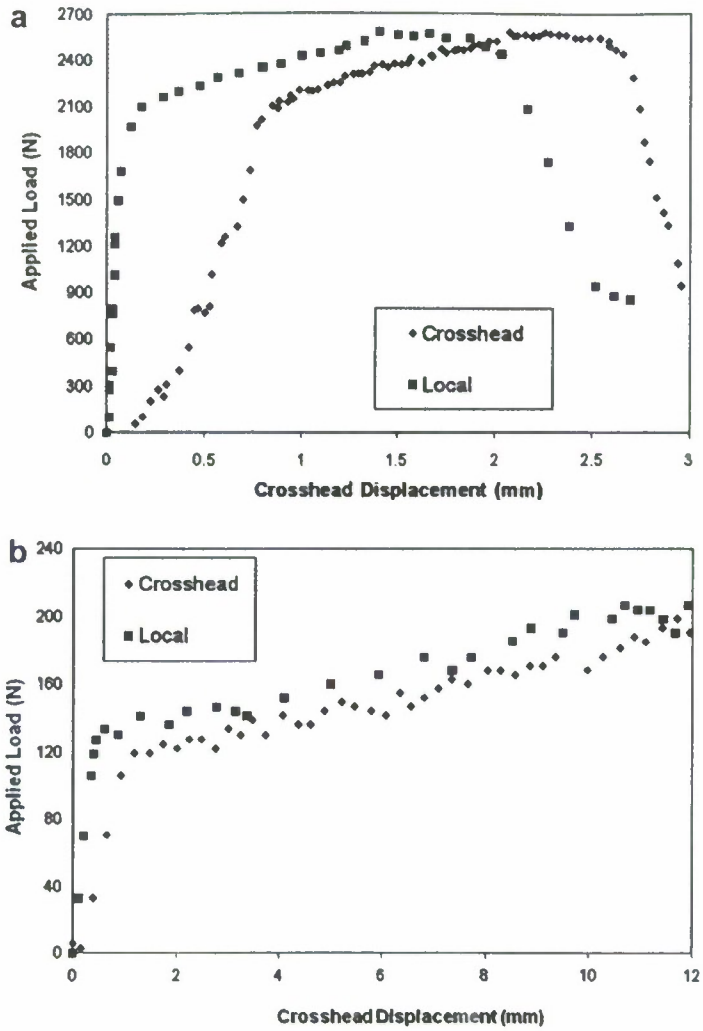

Fig. 5. Displacement measured from CCD images and crosshead displacement for (a) confined tension and (b) confined shear of polyurea/steel sandwiches.

3. Results

3.1. Uniaxial tension and shear behavior of polyurea

Polyurea specimens were characterized in uniaxial tension at three strain rates (0.001, 0.01, and 0.1 s^{-1}). The specimens exhibited (Fig. 6) rate-dependent, nonlinear stress–strain behavior. The initial moduli were slightly dependent on the strain rate; by contrast, the stress level at which softening occurred was quite rate-dependent, increasing with increase in strain rate. The initial modulus of the polyurea was 192 ± 10 MPa.

The nonlinear shear stress–shear strain behavior of polyurea at 0.001, 0.01, and 0.1 s^{-1} is shown in Fig. 7. All the specimens were loaded to failure. Similar to the uniaxial response, the initial shear moduli were slightly dependent on the strain rate; in contrast, the stress level at which softening occurred was quite rate-dependent. The initial shear modulus of the polyurea was 36.5 ± 5 MPa. Note here the shear strain was determined from the CCD imaging. In fact using the crosshead displacement led to an overestimate in the shear strain of 100% and thus a corresponding underestimate in the shear modulus.

3.2. Tension and shear behavior of sandwich specimens

The tension and shear experiments on the sandwich specimens were conducted at nominal strain rates of 0.03 and 3 s^{-1}. In contrast to the monolithic specimens, the initial moduli depended on the loading rates for both tension and shear (Figs. 6 and 7). In tension, the added constraint in the sandwich specimens excites more of a bulk response, which should lessen, rather than increase, the time dependence of the response of a viscoelastic material. However, the bulk polyurea was not

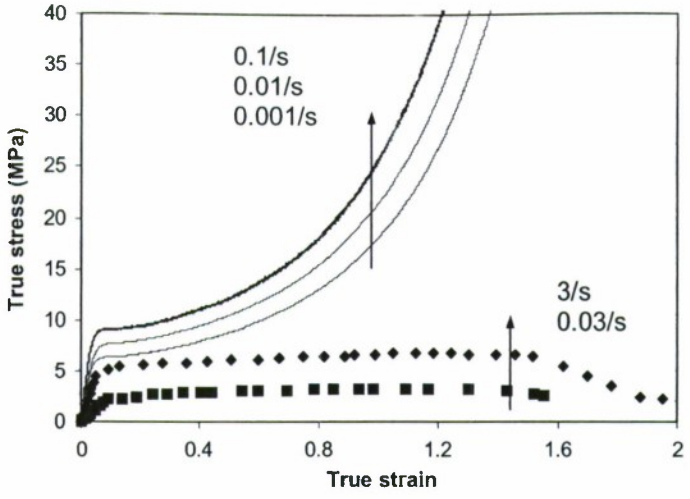

Fig. 6. Stress–strain curves of polyurea under uniaxial tension at different strain rates. The dashed lines are for confined tension of sandwich specimens (0.03 and 3 s^{-1}) and the solid lines are for uniaxial tension (0.001, 0.01, and 0.1 s^{-1}).

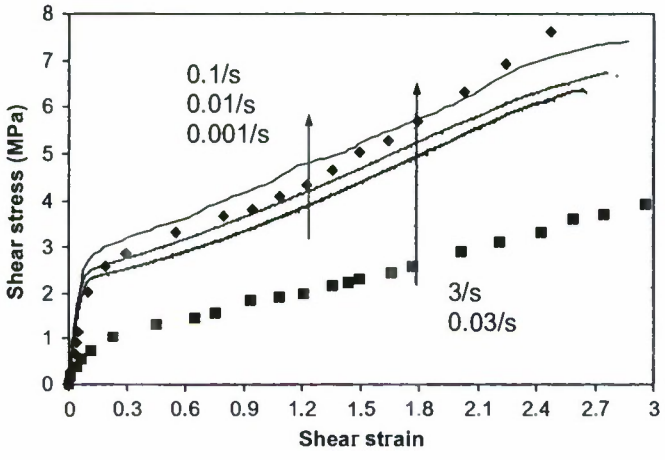

Fig. 7. Stress–strain curves of polyurea under shear at different strain rates. Dashed lines are for shear of sandwich specimens (0.03 and 3 s^{-1}) and solid lines are for shear of butterfly specimens (0.001, 0.01, and 0.1 s^{-1}).

the only possible source of time dependence in the sandwich specimens: the polyurea/steel interface could also have been a contributor, both in tension and shear, through an interphase region.

In the sandwich specimens under tension, the softening stress level occurred at 2 and 5.5 MPa, which was lower than the values for the uniaxial tensile specimens, which ran from 6 to 9 MPa over the strain rates that were imposed. The strain rates in the sandwich specimens ranged from 0.03 to 3 s^{-1}, which means that neither the higher strain rates nor the higher constraint in the sandwich specimens raised the softening stress level. This again suggests that the stress–strain response of the sandwich specimens in Fig. 6 is that of the interface and the lower knee stress levels are an indication of the onset of some form of damage at the interface. This also explains the lower rate of increase in stress levels after the softening stress level compared to the monolithic specimens. At both displacement rates, macroscopic debonding occurred at the maximum stress levels, presumably due to the coalescence of damage.

Under shear, the softening stress levels for the sandwich specimens were lower than had been observed in the monolithic specimens, particularly at the lower rate. This might again be taken as being due to the occurrence of debonding in the sandwich specimens. However, the rate of increase in stress after softening was the same in monolithic and sandwich specimens, which suggests that debonding did not occur prior to the maximum stress.

3.3. Mode 1 fracture

The results of a typical experiment with the DCB specimens are shown in Fig. 8. The variation of the J-integral with the normal end-opening displacement at a loading rate of 0.2 mm/s is shown first (Fig. 8(a)). The J-integral increased with

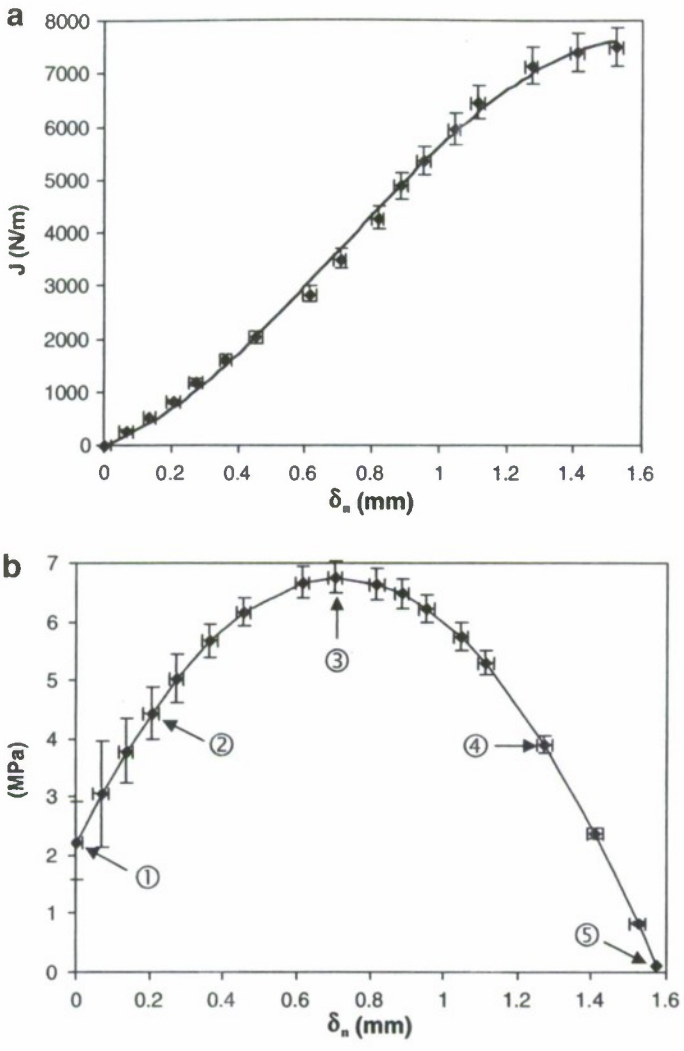

Fig. 8. (a) A typical J–δ_n response and (b) traction–separation law in opening mode fracture. δ_n in both figures is the normal displacement. The strain rate is $0.3\ s^{-1}$.

increasing normal displacement, reaching a steady-state value, J_{SS}. Three methods were employed for numerical differentiation of J with respect to δ_n, including moving average, piecewise fitting and global fitting. They yielded very similar results. Details of these methods are given in Appendix. For convenience of writing the traction–separation laws explicitly, the global fitting method will be used in the rest of the paper. A cubic polynomial fit the J–δ_n response very well and then differentiation with respect to δ_n provided the traction–separation law, as shown in Fig. 8(b). The error bars reflect estimates of the errors involved in determining J, σ and δ_n. The traction–separation laws shown later in the paper were all obtained as averages from 3–4 runs per specimen at different crack lengths.

The entire failure process of the specimen was recorded in accordance with the J-integral measurement. Fig. 9 shows several representative photographs at progressive stages of deformation. Each subfigure corresponds to the stage numbers (?) identified in the traction–separation law (Fig. 8(b)). The initial crack prior to loading ① is shown in Fig. 9(a). The onset of blunting ② can be seen in Fig. 9(b) as the cohesive stress was increasing and small voids could be seen developing in the cohesive zone. Further blunting can be seen (Fig. 9(c)) accompanied by void growth and the initiation of debonding at the upper interface slightly ahead of the pre-crack, corresponding to stage ③. Since this is a nominally mode 1 experiment, interfacial debonding occurs when the stress normal to the interface σ_{22} exceeds the bond strength. The bond strength is equal to the peak cohesive stress σ_0. In Fig. 9(d), the crack blunting was severe. Although the crack opening was more pronounced, it did not propagate. The existing voids grew further and more voids started to appear during stage ④ where the cohesive stress was decreasing. The final stage ⑤ of the separation process corresponds to zero cohesive stress and the growth of the interfacial crack, as shown in Fig. 9(e).

Specimens were tested at four loading rates and, for each rate, there was some specimen-to-specimen variation in the J–δ_n curves, particularly at small and large openings. The variation at small openings might have been due to variations in the

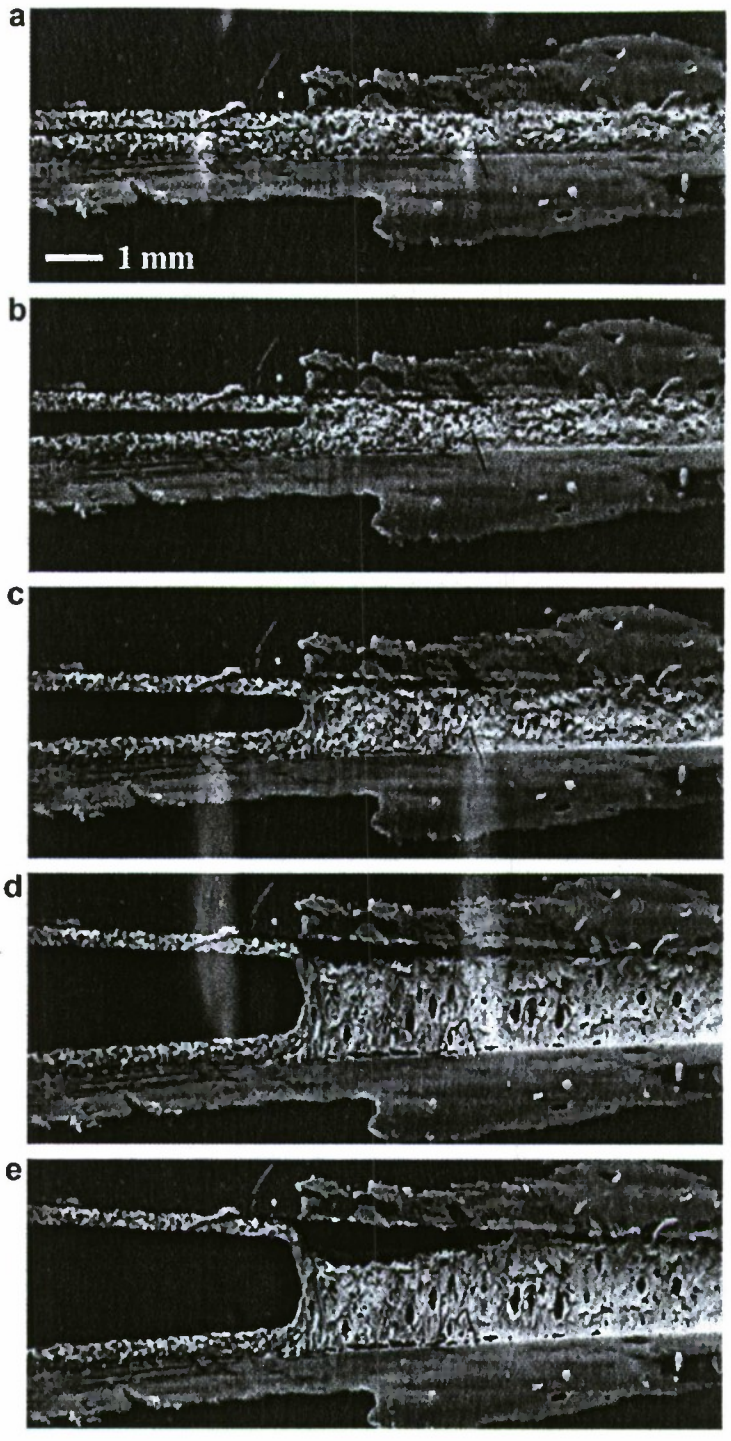

Fig. 9. The entire sequence of the failure process of a polyurea/steel sandwich specimen in opening mode fracture. The images correspond to the different stages in the traction–separation law as shown in Fig. 8b.

initial crack sharpness, or experimental error in displacement measurements. The variation at large opening displacements might have been caused by variations in the failure process zone evolution as described later. Fig. 10(a) plots the average of the fitted cubic polynomials for J–δ_n curves at each loading rate while the corresponding traction–separation laws appear in Fig. 10(b). The effect of loading rate on the traction–separation law was pronounced. The peak cohesive stress was about 1.8 MPa for the slowest loading rate (0.002 mm/s) and about three times higher for the highest loading rate (5 mm/s). In the meantime, δ_{nc} (critical end-opening displacement) decreased from about 2.4 mm to nearly 1 mm. Even though the

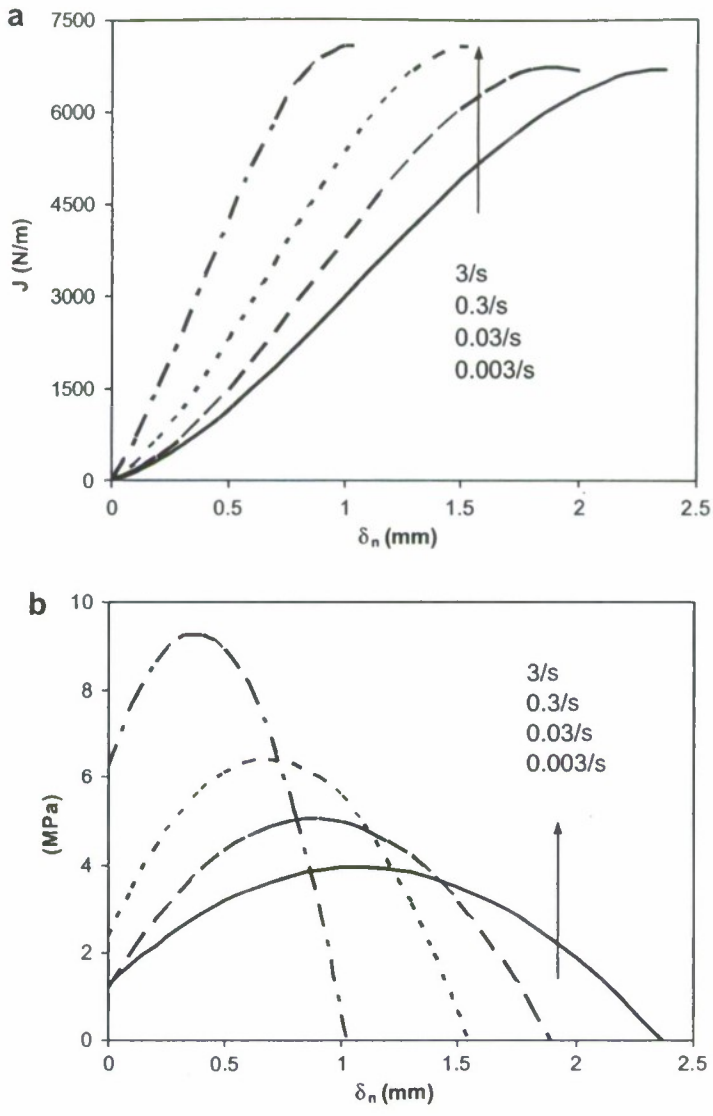

Fig. 10. (a) J–δ_n curves and (b) traction–separation laws for opening mode fracture at different loading rates. δ_n in both figures is the normal displacement.

shapes of all the cohesive laws followed quadratic polynomials, the details were quite different for each loading rate. For the slowest loading rate the cohesive stress rose to its peak at a fairly large crack opening (~1.1 mm); by contrast, for the highest loading rate the cohesive stress rises rapidly to the peak stress.

The cohesive law at each loading rate can be expressed by a quadratic polynomial, similar to the polynomial cohesive law proposed by Needleman (1987). It can be written as

$$\sigma(\delta_n) = -\frac{\sigma_0}{(\delta_{nc} - \delta_{n0})^2}(\delta - \delta_{n0})^2 + \sigma_0, \tag{8}$$

where σ_0 is the peak cohesive stress, δ_{nc} is the critical end-opening displacement, and δ_{n0} is the end-opening displacement at which the cohesive stress reaches σ_0. The values of the parameters σ_0, δ_{n0}, and δ_{nc} for all the loading rates at mode 1 fracture are given in Table 1.

3.4. Mode 2 fracture

The results from the ENF experiments are presented first. Fig. 11(a) is an image of a crack in an ENF specimen. Using digital image correlation (DIC), we found that, behind the crack tip, there was a compressive strain perpendicular to the interface of about 5% (Fig. 11(b)), distributed quite evenly along the crack faces. This resulted in frictional loading of the crack faces (Fig. 11(c)). In addition, the ENF specimen only provides a relatively small shear displacement that was not sufficient

Table 1
Parameters for the quadratic traction–separation law equation (8) as a function of loading rate and mode

Rate (s^{-1})	$\Gamma 1$ (kJ/m^2)	σ_0 (MPa)	δ_{n0} (mm)	δ_{nc} (mm)	$\Gamma 2$ (kJ/m^2)	τ_0 (MPa)	δ_{tc} (mm)
0.003	6.69	3.95 ± 0.06	1.21 ± 0.02	2.36 ± 0.04	–	–	–
0.03	6.68	5.12 ± 0.15	0.92 ± 0.04	1.90 ± 0.08	8.29	2.72 ± 0.12	4.15 ± 0.15
0.3	7.08	6.45 ± 0.35	0.76 ± 0.05	1.56 ± 0.13	11.26	5.45 ± 0.25	3.18 ± 0.20
3.00	7.08	9.25 ± 0.60	0.41 ± 0.02	1.02 ± 0.05	13.44	6.97 ± 0.46	3.02 ± 0.16

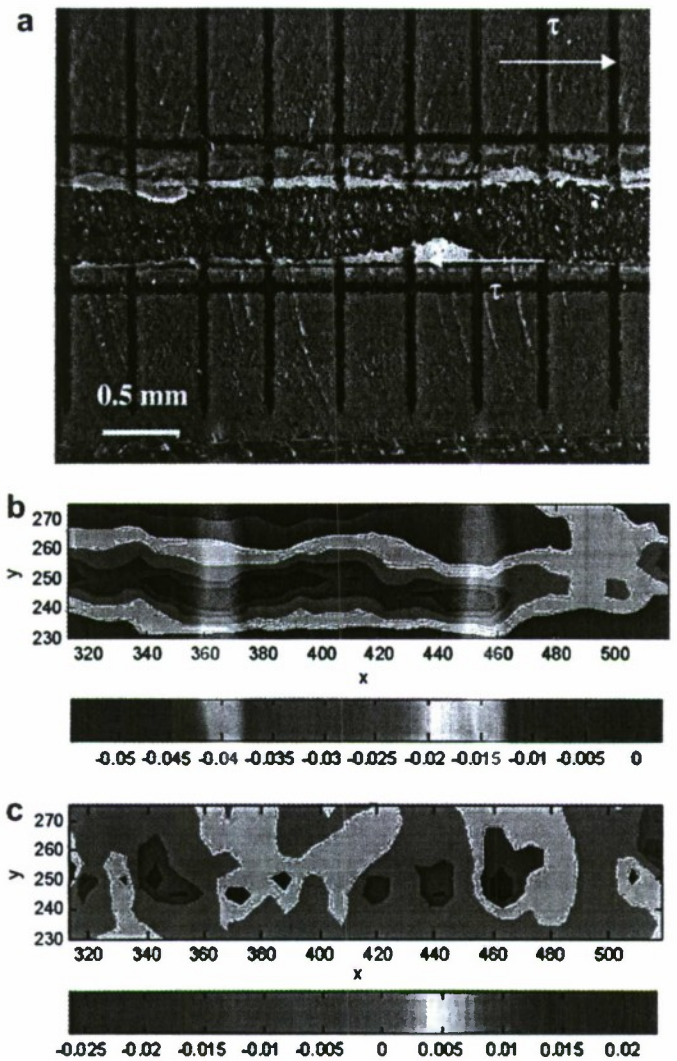

Fig. 11. (a) The crack tip region in an ENF specimen the two red dots define a rectangular area that is analyzed using DIC and plotted in (b) and (c), (b) the through-thickness compressive strain behind the crack front, and (c) the through-thickness frictional loading along the crack faces. The scale bars in (b) and (c) show the strains in vertical and horizontal directions, respectively. (For interpretation of the references to colours in this figure legend, the reader is referred to the web version of this paper).

to heavily deform and damage the highly deformable polyurea. These issues motivated the consideration of the Arcan configuration, which can provide large shear displacements.

A modified version (Popelar and Liechti, 2003) of the original Arcan configuration (Arcan et al., 1978) was considered here. The J–δ_t curves and the shear traction–separation laws at three loading rates, are given in Fig. 12(a) and (b), respectively. Similar to the mode 1 fracture experiments, J increased with increasing δ_t, reaching a steady-state value J_{SS}. Here, the J–δ_t curves could not be fitted well with a polynomial so a piecewise fitting algorithm was employed to obtain the traction–separation law. The entire crack initiation and propagation process was also recorded. Fig. 13 shows representative images of different stages in the deformation of a specimen loaded at a nominal strain rate of 3 s^{-1}. In Fig. 13, stage ① shows

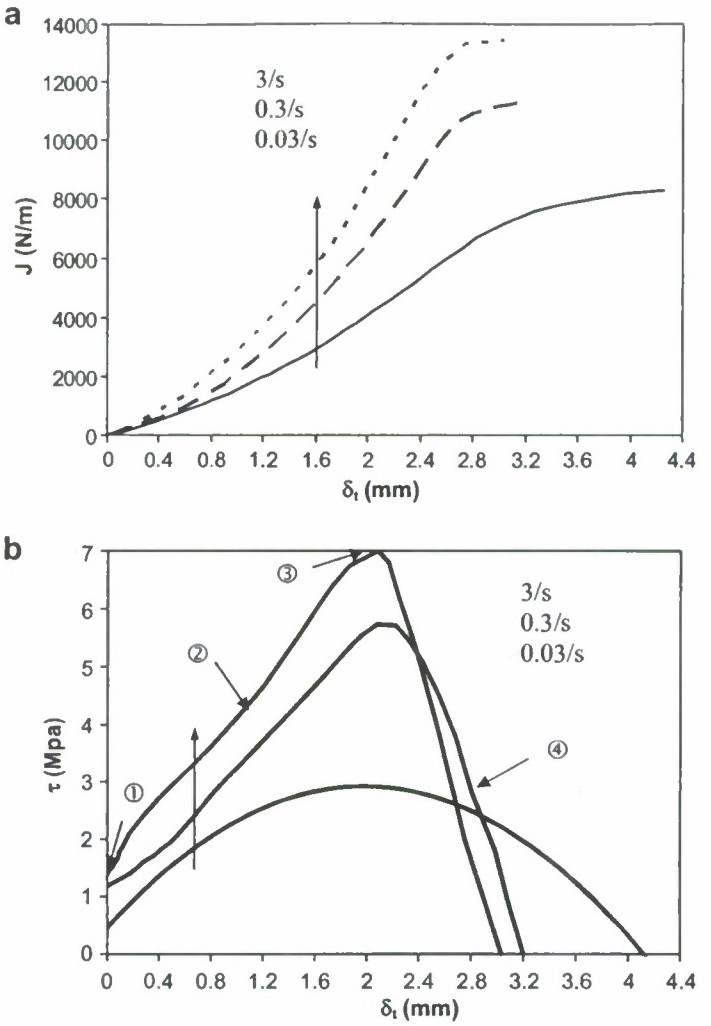

Fig. 12. (a) J–δ_t curves and (b) traction–separation laws for shear fracture at different loading rates. δ_t in both figures is the shear displacement.

the initial crack prior to loading (corresponding to ① in Fig. 12(b)). An intermediate stage ② illustrates the onset of localized stretching from the crack tip to the right interface as the cohesive stress increased. This can be seen as the region with oriented texture emanating from slightly behind and extending ahead of the crack tip. Further stretching ahead of the crack tip appears in stage ③ together with debonding along the interface in front of the crack tip corresponding to the peak cohesive stress. At stage ④, the polyurea around the crack tip was partially retracted due to the onset of the debonding, and the cohesive stress decreased. The interfacial debonding resulted in unloading of the adjacent adhesive layer, and the debonding itself propagated in a catastrophic manner. The peak shear stress τ_0 and the critical shear displacement δ_{tc} for all the loading rates are given in Table 1.

The images in Fig. 13 suggest that the crack did not advance under shear stress; instead the interfacial debonding occurred due to the normal component of the stretching exceeding the bond strength. The local strain field ahead of the crack tip was therefore evaluated using DIC. The shear displacement fields and corresponding strains are presented at several load levels. Fig. 14(a) and (b) provide contours of the displacement component parallel to the interfaces and engineering shear strain, respectively. Concentration of the strain near the crack tip can be clearly identified. The shear strain profiles at three load levels (Fig. 14(c)) along a line starting from the crack tip shows the concentrations near the crack tip and the decay to the nominal values (dashed line) beyond approximately two layer thicknesses. At all load levels, the maximum shear strain appeared to be nearly 1.5 times the uniform strain.

4. Discussion

In this section, we discuss the form and rate dependence of the traction–separation laws and how they may be related to the time dependence of bulk polyurea and porosity.

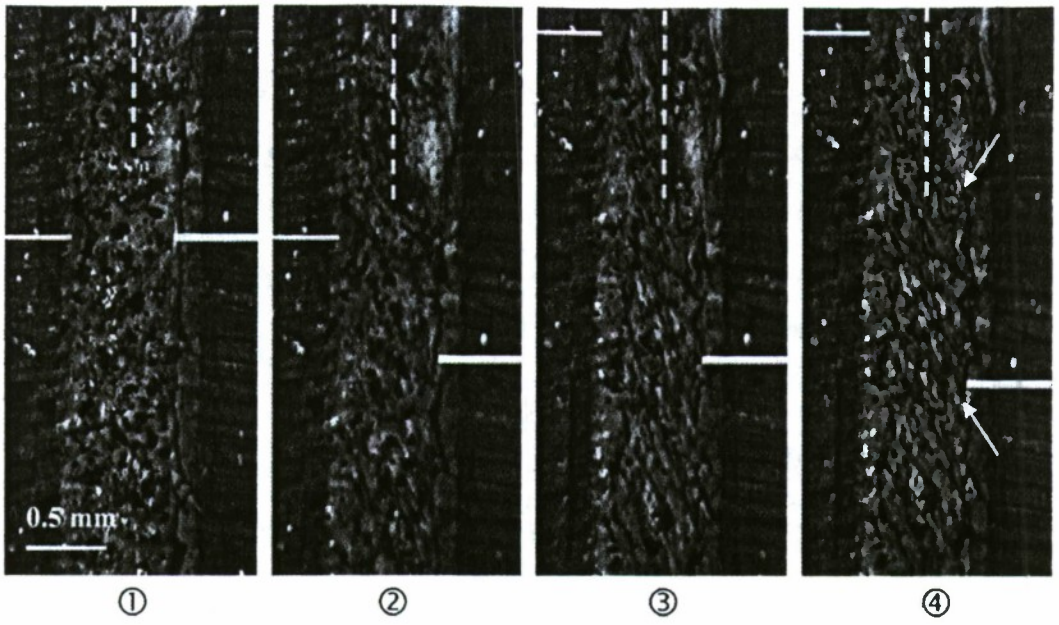

Fig. 13. The entire sequence of crack initiation in a sandwich specimen under shear loading. The images are in accordance with the different stages identified in Fig. 12(b). A dashed vertical line in each subfigure is drawn to highlight evolution of the initial crack. Two solid horizontal lines moving with the two adherends show the relative displacement between the adherends in order to illustrate the shear deformation in the polyurea. In ④, two arrows on the right side of the polyurea/steel interface mark the tips of an interfacial crack.

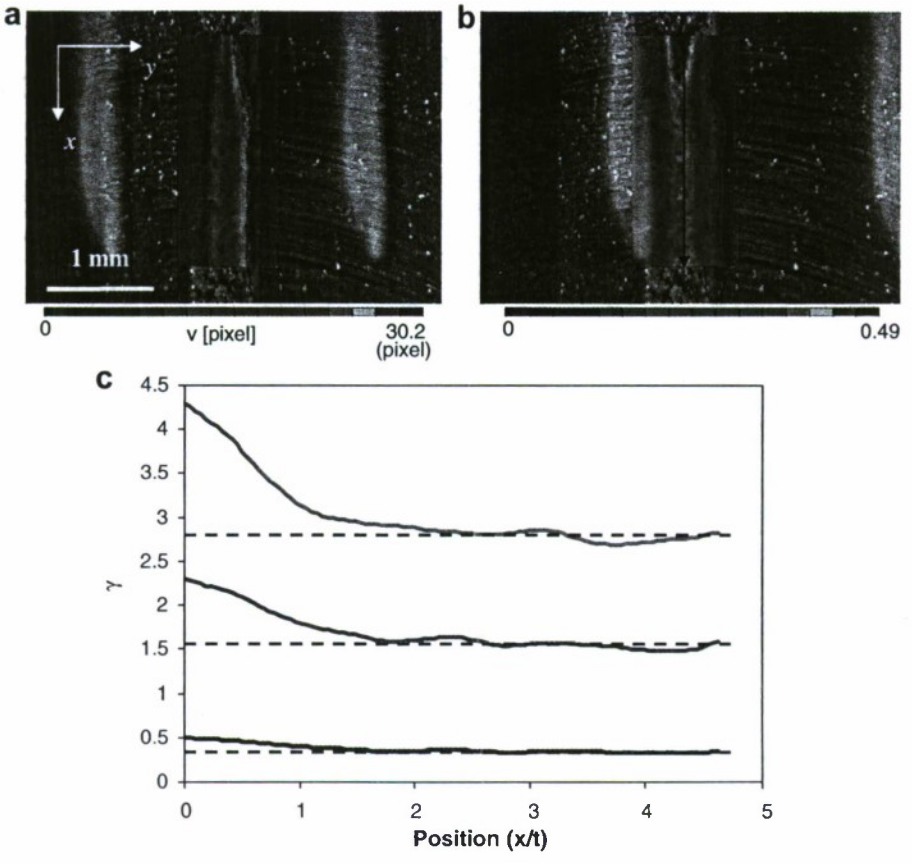

Fig. 14. (a) Shear displacement contours, (b) engineering shear strain contours, and (c) engineering shear strain as a function of distance from the crack tip. Dashed lines are the nominal shear strains. The three strain profiles correspond to images ①, ② and ③ in Fig. 3.

Table 2
Comparison of softening stress with maximum traction levels

Softening stress			Maximum traction			Ratio	
Rate (s^{-1})	Tension σ_s (MPa)	Shear τ_s (MPa)	Rate (s^{-1})	Normal σ_0 (MPa)	Shear τ_0 (MPa)	Normal σ_0/σ_s	Shear τ_0/τ_s
0.001	6.39	2.37	0.003	3.95	2.92	0.62	1.23
0.01	7.69	2.53	0.03	5.12	5.72	0.67	2.26
0.1	9.01	2.86	0.3	6.45	7.01	0.72	2.45
			3.00	9.25			

4.1. Shape

The most striking feature of the traction–separation laws shown in Figs. 10 and 12 is the nonzero stress at zero crack opening. This has been observed before by Sorensen (2002) who used the same method to determine the traction–separation laws associated with adhesive joints consisting of polyurethane and steel. It has also been assumed in traction–separation laws that have been extracted iteratively (Swadener and Liechti, 1998; Shirani and Liechti, 1998; Mello and Liechti, 2006). Jin and Sun (2005) recently provided a theoretical basis for this feature, arguing that it is needed in order to remove the singularity at the crack tip. At the same time, it seems unlikely that a real material would have a step increase in traction near zero displacement, which then relates to questions about the resolution of the technique. The resolution of the displacement technique was 2 μm, two orders of magnitude less than the scale interval in Fig. 8 and one order of magnitude better than is needed for resolving modulus. However, the differentiation process to obtain the tractions can cause significant scatter in data, as is shown in Fig. A1 of Appendix. Consequently, a polynomial fitting to the J-integral was employed, which provided a smooth traction–separation law but might be smearing some details, especially in the initial stages of loading. Nonetheless, all three techniques did point to a sharp increase in stress near zero displacement.

Jin and Sun further suggested that the maximum traction ranges from 1.15 to 2.5 times the yield strength of the material for perfectly plastic to mildly strain hardening materials (hardening exponent of 0.2). For comparison, the ratios of the maximum tractions to the softening stress levels that were obtained in the present study are shown in Table 2. For mode 1 fracture and uniaxial tension, the ratios were less than one. This simply suggests that, in tension, the interface is weaker than the bulk material. Under shear, the ratios ranged from 1.23 to 2.45, which is in the range suggested by Jin and Sun. Interestingly, the shear stress–strain behavior of the bulk polyurea was more like a metal than the tensile stress–strain behavior, which exhibited the usual softening followed by stiffening behavior of polymers. The overall shapes of the traction–separation laws changed with loading rate and fracture mode. Tvergaard and Hutchinson (1993) suggested that effect of the shape on the fracture process was relatively unimportant. However, Gu (1995) found that the shape of bridging laws did affect crack growth calculations in fiber-reinforced ceramics and Jacobsen and Sørensen (2001) made similar observations in mode I intralaminar crack growth in fiber-reinforced polymers. A recent reexamination of this issue (Jin and Sun, 2005) suggests that the shape governs the cohesive zone size and what was termed "the apparent energy release rate of LEFM", a quantity that approaches the cohesive energy density when crack extensions are significantly greater than the cohesive zone size.

4.2. Rate dependence

In Section 3.1, it was noted that, under uniaxial tension and shear, the polyurea exhibited slight rate dependence prior to softening and considerably more thereafter. The response of the sandwich specimens was much more time dependent prior to and following softening, which suggested that the interface was playing a role. The initial portion of the mode 1 and 2 traction–separation laws also exhibited significant levels of rate dependence. In view of the interfacial nature of the crack growth in the specimens, this suggests that the traction separation laws are reflecting the time dependence of the interphase region. In fact, if the tensile and shear response of the sandwich specimens is plotted alongside the corresponding traction–separation law (Fig. 15), there is a remarkable resemblance between them further strengthening the argument that the traction–separation laws determined here represent the behavior of the interphase. In addition, the strain rates are amplified at the interfacial crack fronts, which would bring the response of the polyurea further into the viscoelastic regime.

The area under the traction–separation law or the intrinsic toughness Γ is considered as a function of the nominal strain rate in Fig. 16. The mode 1 toughness values were consistently lower than the mode 2 values and displayed very little dependence. The mode 2 toughness was much more rate dependent; nearly double the mode 1 value at the highest rate. Although mode 2 experiments were not conducted at the lowest rate (0.003 s^{-1}), the trend of the data suggests that the mode 1 and 2 toughness values could be quite similar there. The greater influence of strain rate in shear is not surprising given the dilatational contribution to mode 1 and the shorter viscoelastic spectrum in the bulk relaxation modulus of the polyurea.

4.3. Failure mechanisms

As observed in Fig. 9, the initial cohesive crack did not propagate under mode 1 loading; rather an interfacial debond occurred ahead of it despite the fact that the stress at the crack tip is higher than that at the debonding site. This indicates that the interface was relatively weak compared to the cohesive strength of the polyurea. Similar observations were made for

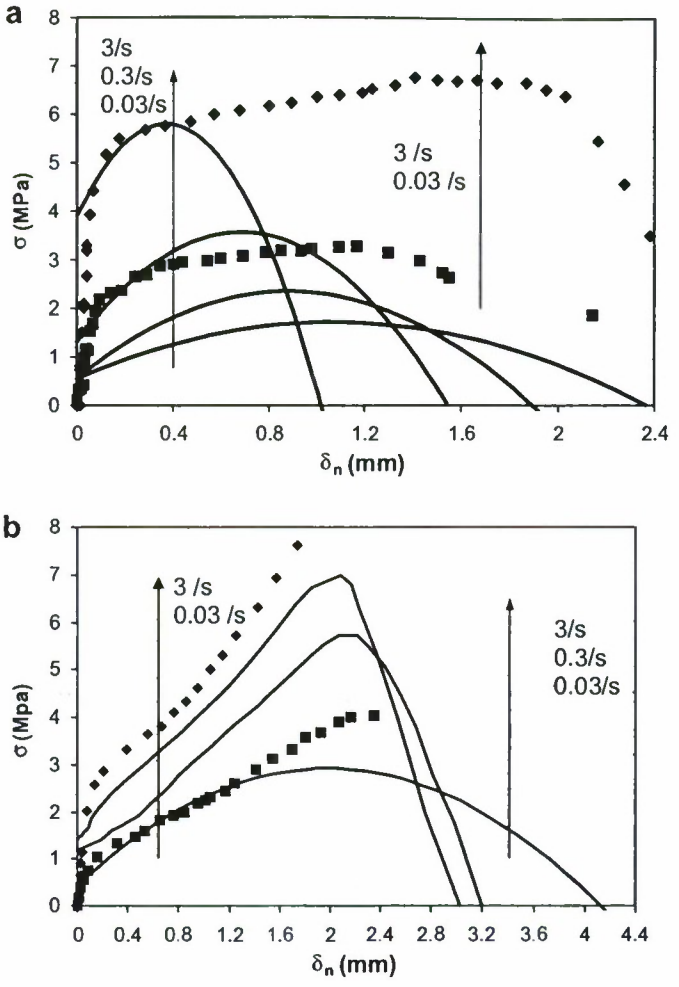

Fig. 15. The response of uncracked sandwich specimens is compared with traction–separation laws obtained under (a) tension and (b) shear. For both tension and shear, the dashed lines are for uncracked sandwich specimens at 0.03 and 3 s^{-1} and the solid lines are for the fracture experiments at 0.03, 0.3, and 3 s^{-1}.

mode 2 fracture (Fig. 13). The initial crack did not propagate perpendicular to the direction of the maximum tangential stress. Instead, the material between the crack tip and both interfaces stretched as can be seen from the texture that developed at roughly 45° to the original direction of the crack. Interfacial debonding occurred at the intersection of the texture and either interface, either ahead of or slightly behind the original crack tip.

This failure mechanism for mode 2 fracture is quite different from observations in the literature (Chai and Chiang, 1996; Shih et al., 1991). For a brittle adhesive, micro cracks opened up ahead of the initial crack and grew in the direction normal to the maximum principal stress direction. For a ductile adhesive, a number of failure modes have been reported. If the initial crack is at an interface: (1) the crack can propagate along the same interface; (2) a micro debond can occur on the other interface ahead of the crack tip; (3) it can kink to the other interface and later form a micro debond on the initial interface or (4) a void can nucleate in the adhesive layer ahead of the crack tip. If the initial crack is in the middle of the adhesive layer: (1) it can kink to one interface and exhibit the behaviors just mentioned or (2) a void is nucleated in front the crack tip. In view of the fact that the polyurea can be stretched for several hundred percent, the failure mechanism for polyurea/steel interface belongs to the category of ductile failure.

For ductile adhesive joints under mode 1 loading, there are four fracture mechanisms: (1) near-tip void growth and coalescence; (2) interfacial debonding near the crack tip; (3) cavitation induced by high triaxiality ahead of the crack tip; and (4) interfacial debonding ahead of the crack tip. Schematics of these four mechanisms are sketched in Fig. 17. Fracture mechanism 1 is commonly observed in the ductile fracture of homogeneous materials. When the crack tip blunts to an opening of the order of the mean spacing between voids, the voids are wholly within the finite strain zone so that void-crack coalescence is imminent. Fracture mechanism 2 occurs when the near-tip stress normal to the interface σ_{22} exceeds the bond strength of the weak interface. Fracture mechanism 3 is due to cavitation at a distance of several adhesive layer thicknesses ahead of the crack tip. The remote triaxiality develops when the interfacial bond is sufficiently strong to allow the ductile

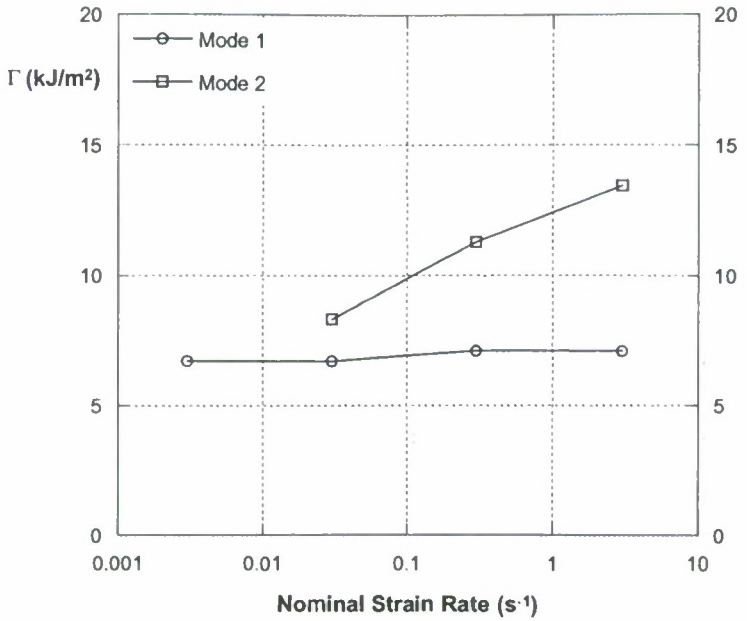

Fig. 16. The intrinsic toughness in mode 1 and mode 2 as a function of the nominal strain rate.

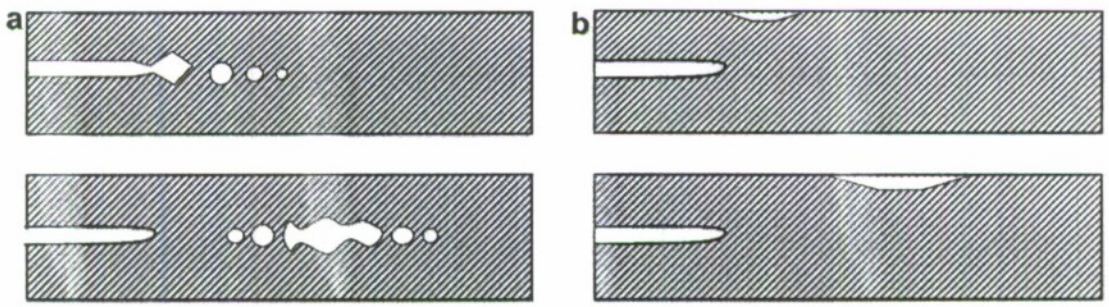

Fig. 17. Four typical fracture mechanisms in a ductile adhesive joint. (a) Near-tip void growth and coalescence; (b) interface debonding near the crack tip; (c) high triaxiality cavitation ahead of the crack tip and subsequent coalescence; and (d) interface debonding ahead of the crack tip.

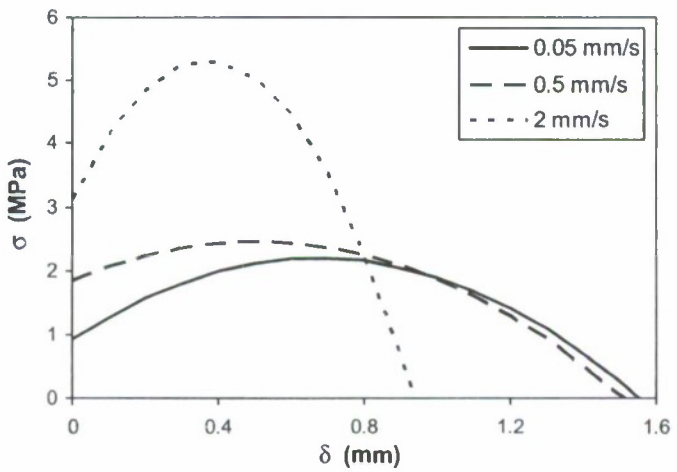

Fig. 18. Traction–separation laws for opening mode fracture of the second batch (porous polyurea) at different loading rates. δ_t is the shear displacement.

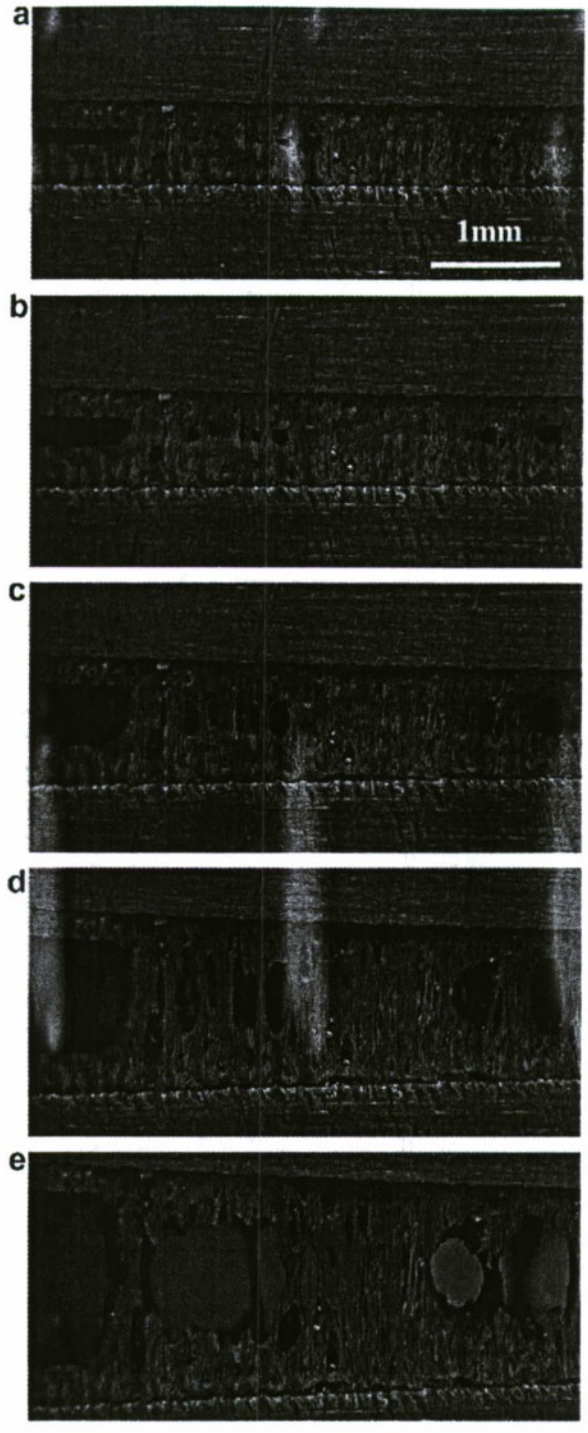

Fig. 19. Entire sequence of the failure process of a porous adhesive joint in opening mode fracture. The images are in accordance with the different stages in the traction separation law as shown in Fig. 17 (loading rate 0.2 mm/s).

layer to undergo substantial plastic deformation. Detailed analyses and comparison with experiments for each fracture mechanism are beyond the scope of this paper. Interested readers can refer to the analyses for similar sandwiched systems provided in Shih et al. (1991) for mechanism 2 and in Choi et al. (2001) and Varias et al. (1991) for the other three mechanisms. Mechanism 2 is the one that was observed in our experiments here. Our experimental results for mode 1 fracture can be categorized as the second fracture mechanism. However, if significant levels of porosity are introduced in the adhesive layer, the failure mechanism may be different, as is now discussed in the following section.

4.4. Effects of the polymer porosity

The spray process that was used in forming the polyurea layer introduced a large number of voids (pores) in the material. The volume fraction of the porosity and the distribution of pore sizes depend on the exact chemical formulation and conditions of the spray process (such as temperature and humidity). In addition, because of the manner in which the sandwich was constructed, there are more pores along the mating surfaces. In order to examine the effect of porosity, we conducted the same fracture tests on another batch of sandwich specimens that consisted of more porous polyurea. We used density as the parameter to characterize the porosity; the densities of the first and second batches were 639 ± 23 and 529 ± 7.9 kg/m^3, respectively.

The entire failure process of the second set of specimens was recorded in accordance with the J-integral procedures described earlier. Fig. 18 shows the traction–separation laws that were obtained from this set of specimens at three different loading rates. For the same loading rates, the cohesive strength was smaller than that of the first batch. Fig. 19 shows several representative photographs at progressive stages of deformation for the loading rate of 0.2 mm/s. Fig. 19(a) corresponds to the initial crack prior to loading ①. Several pores along the mating surface are visible. The onset of blunting ② can be seen in Fig. 19(b) as the cohesive stress was increasing and the pores were developing in the cohesive zone. Further blunting can be seen (Fig. 19(c)) accompanied by pore growth. This stage ③ corresponds to the peak cohesive stress. In Fig. 19(d), the crack blunting was severe. The pores grew further in both directions normal and transverse to the load and the pore coalescence started during stage ④ where the cohesive stress was decreasing. The final stage ⑤ of the pore coalescence process corre-

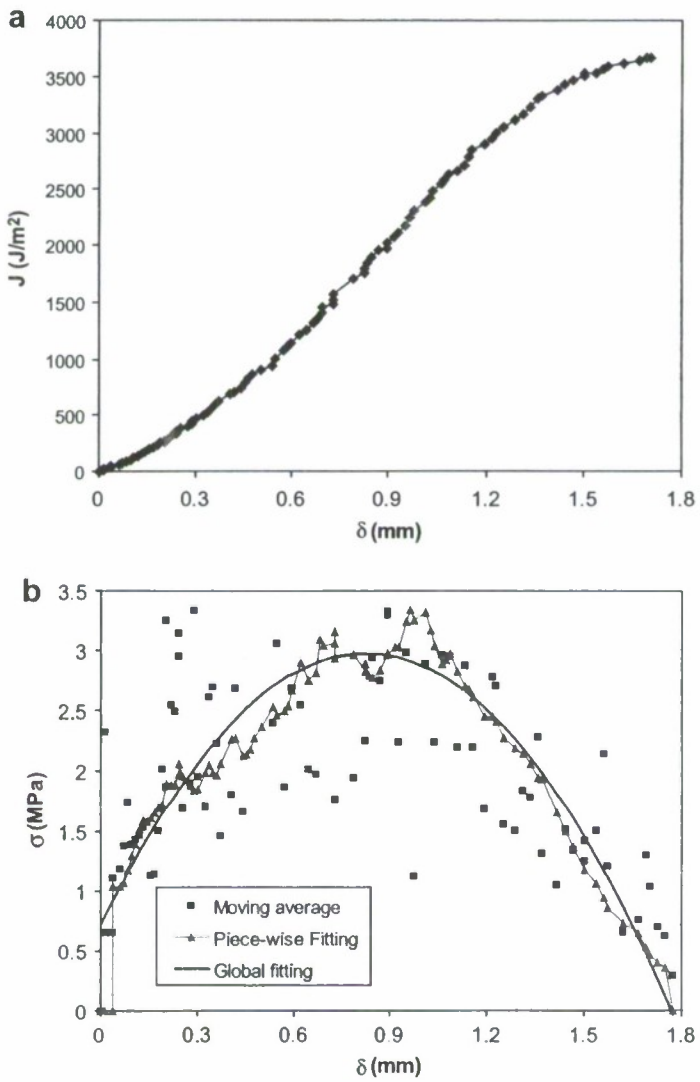

Fig. A1. (a) An example of J–δ curve for a polyurea/steel adhesive joint. (b) The traction–separation laws obtained using three numerical methods for differentiation. δ in both figures is the normal displacement.

sponds to zero cohesive stress and the growth of the interfacial crack, as shown in Fig. 19(e). This failure seems to be a combination of the first and the third mechanisms depending on the stress field ahead of the crack tip and the initial void locations and sizes.

5. Conclusions

Mode 1 and mode 2 traction–separation laws have been obtained for polyurea/steel sandwich specimens. The cohesive laws were obtained directly from experiments by differentiation of simultaneously measured data (the J-integral and the end-opening displacement). Several important observations of the traction–separation laws and the associated interfacial fracture features are summarized in the following.

(1) The traction–separation laws are highly nonlinear. In fact the mode 1 traction–separation law can be fitted well with a quadratic polynomial.
(2) Both mode 1 and mode 2 traction–separation laws exhibited pronounced rate dependence. In both cases, the fracture toughness and the peak cohesive stress increased with loading rate, while the critical opening displacement decreased with loading rate.
(3) Both loading modes gave rise to interfacial debonding near the original cohesive crack-tip.
(4) The traction–separation laws obtained here represented the behavior of the interphase.
(5) Another batch of sandwich specimens consisting of polyurea with a higher degree of porosity was tested. The specimens failed by near-tip void growth/coalescence and/or high triaxiality induced cavitation ahead of the crack tip.

Now that we have both mode 1 and mode 2 traction–separation laws, we can incorporate them into mixed-mode cohesive models (Tvergaard and Hutchinson, 1993; Yang and Thouless, 2001) to predict the mixed-mode behavior of structures involving polyurea/steel interfaces at different loading rates. However, it should be borne in mind that the nominal strain rates across the adhesive layer examined in this paper only ranged from 0.003 to 3 s^{-1}. The determination of traction–separation laws at higher loading rates, where inertia effects must be taken into account is currently underway.

Acknowledgements

This work was supported by the Office of Naval Research with Dr. Roshdy Barsoum as program manager. The insightful comments of both reviewers were very helpful in preparing the final version of this paper.

Appendix. The accuracy of the direct approach relies on the numerical differentiation of the J-integral with respect to the end-opening displacement. Moving average, piecewise fitting and global fitting were considered and are briefly described below. Fig. A1(a) shows a typical J integral vs. end-opening displacement response that served as the basis for the examination.

A moving average filter smoothes data by replacing each data point with the average of the neighboring data points defined within a given span. This process is equivalent to low-pass filtering with the response of the smoothing given by the difference equation

$$y_s(i) = \frac{1}{2n+1}[y(i-n) + y(i-n+1) + \cdots + y(i+n)],$$

where $y_s(i)$ is the smoothed value for the ith data point, n is the number of neighboring data points on either side of $y(i)$, and $2n + 1$ is the span. The end points are not smoothed because a span cannot be defined. After the J-integral data are smoothed, direct differentiation is performed with respect to the end-opening displacement using a central difference scheme.

For piecewise fitting, consider a large number of sets of data for the J-integral and end-opening displacement. For data set number i, a quadratic polynomial is fitted to the data sets ranging from $(i - n)$ to $(i - n)$, where n is as defined above. The slope of the polynomial is the stress corresponding to the ith value of end-opening displacement. Since the first and last several data points cannot be fitted with polynomial equations, stress values for these points are omitted.

The last method to be considered was global fitting. One cubic polynomial equation was able to fit the J–δ data very well. The slope of this polynomial equation yields the stress value for each end opening displacement. This method yielded the most reasonable traction–separation law and was therefore adopted throughout the study.

References

Arcan, M., Hashin, Z., Voloshin, A., 1978. Method to produce uniform plane-stress states with applications to fiber-reinforced materials. Experimental Mechanics 18 (4), 141–146.
Banks-Sills, L., Sherman, D., 1991. JII fracture testing of a plastically deforming material. International Journal of Fracture 50 (1), 15–26.
Barenblatt, G.I., 1962. The mathematical theory of equilibrium cracks in brittle fracture. Advances in Applied Mechanics 7, 55–129.
Carlsson, L.A., Gillespie, J.W., Pipes, R.B., 1986. On the analysis and design of the end notched flexure (ENF) specimen for mode-I testing. Journal of Composite Materials 20 (6), 594–604.

Chai, H., Chiang, M.Y.M., 1996. A crack propagation criterion based on local shear strain in adhesive bonds subjected to shear. Journal of the Mechanics and Physics of Solids 44 (10), 1669–1689.
Choi, S.H., Song, B.G., Kang, K.J., Fleck, N.A., 2001. Fracture of a ductile layer constrained by stiff substrates. Fatigue & Fracture of Engineering Materials & Structures 24 (1), 1–13.
Cotterell, B., Mai, Y.W., 1996. Fracture Mechanics of Cementitious Materials. Blackie, London.
Cox, B.N., Marshall, D.B., 1991. The determination of crack bridging forces. International Journal of Fracture 49 (3), 159–176.
Dugdale, D.S., 1960. Yielding of steel sheets containing slits. Journal of the Mechanics and Physics of Solids 8, 100–104.
Flinn, B.D., Lo, C.S., Zok, F.W., Evans, A.G., 1993. Fracture-resistance characteristics of a metal-toughened ceramic. Journal of the American Ceramic Society 76 (2), 369–375.
Gu, P., 1995. Notch sensitivity of fiber-reinforced ceramics. International Journal of Fracture 70, 253–266.
Högberg, J.L., Sorensen, B.F., Stigh, U., 2007. Constitutive behaviour of mixed mode loaded adhesive layer. International Journal of Solids and Structures 44, 8335–8354.
Hutchinson, J.W., Suo, Z., 1992. Mixed-mode cracking in layered materials. Advances in Applied Mechanics 29, 63–191.
Ivankovic, A., Pandya, K.C., Williams, J.G., 2004. Crack growth predictions in polyethylene using measured traction–separation curves. Engineering Fracture Mechanics 71 (4–6), 657–668.
Jacobsen, T.K., Sørensen, B.F., 2001. Mode I intra-laminar crack growth in composites – modelling of *R*-curves from measured bridging laws. Composites Part A: Applied Science and Manufacturing 32 (1), 1–11.
Jin, Z.H., Sun, C.T., 2005. Cohesive fracture model based on necking. International Journal of Fracture 134 (2), 91–108.
Kim, K.S., Aravas, N., 1988. Elastoplastic analysis of the peel test. International Journal of Solids and Structures 24, 417–435.
Kinloch, A.J., Lau, C.C., Williams, J.G., 1994. The peeling of flexible laminates. International Journal of Fracture 66, 45–70.
Landis, C.M., Pardoen, T., Hutchinson, J.W., 2000. Crack velocity dependent toughness in rate dependent materials. Mechanics of Materials 32 (11), 663–678.
Leffler, K., Alfredsson, K.S., Stigh, U., 2007. Shear behaviour of adhesive layers. International Journal of Solids and Structures 44, 530–545.
Liechti, K.M., Knauss, W.G., 1982. Crack-propagation at material interfaces. 2. Experiments on mode interaction. Experimental Mechanics 22 (10), 383–391.
Liechti, K.M., Wu, J.D., 2001. Mixed-mode, time-dependent rubber/metal debonding. Journal of the Mechanics and Physics of Solids 49 (5), 1039–1072.
Li, V.C., Chan, C.-M., Leung, C.K.Y., 1987. Experimental determination of the tension-softening relations for cementitious composites. Cement and Concrete Research 17, 441–452.
Li, S., Thouless, M.D., Waas, A.M., Schroeder, J.A., Zavattieri, P.D., 2005a. Use of a cohesive-zone model to analyze the fracture of a fiber-reinforced polymer–matrix composite. Composites Science and Technology 65 (3–4), 537–549.
Li, S., Thouless, M.D., Waas, A.M., Schroeder, J.A., Zavattieri, P.D., 2005b. Use of mode-I cohesive-zone models to describe the fracture of an adhesively-bonded polymer–matrix composite. Composites Science and Technology 65 (2), 281–293.
Li, S., Thouless, M.D., Waas, A.M., Schroeder, J.A., Zavattieri, P.D., 2006. Mixed-mode cohesive-zone models for fracture of an adhesively bonded polymer-matrix composite. Engineering Fracture Mechanics 73 (1), 64–78.
Massabo, R., Mumm, D.R., Cox, B.N., 1998. Characterizing mode II delamination cracks in stitched composites. International Journal of Fracture 92 (1), 1–38.
Mello, A.V., Liechti, K.M., 2006. The effect of self-assembled monolayers on interfacial fracture. Journal of Applied Mechanics 73, 860–870.
Mohammed, I., Liechti, K.M., 2000. Cohesive zone modeling of crack nucleation at bimaterial corners. Journal of the Mechanics and Physics of Solids 48 (4), 735–764.
Needleman, A., 1987. A continuum model for void nucleation by inclusion debonding. Journal of Applied Mechanics-Transactions of the Asme 54 (3), 525–531.
Needleman, A., 1990. An analysis of tensile decohesion along an interface. Journal of the Mechanics and Physics of Solids 38 (3), 289–324.
Pandya, K.C., Williams, J.G., 2000. Measurement of cohesive zone parameters in tough polyethylene. Polymer Engineering and Science 40 (8), 1765–1776.
Parmigiani, J.P., Thouless, M.D., 2007. The effects of cohesive strength and toughness on mixed-mode delamination of beam-like geometries. Engineering Fracture Mechanics 74, 2675–2699.
Popelar, C.F., Liechti, K.M., 1997. Multiaxial nonlinear viscoelastic characterization and modeling of a structural adhesive. Journal of Engineering Materials and Technology-Transactions of the Asme 119 (3), 205–210.
Popelar, C.F., Liechti, K.M., 2003. A distortion-modified free volume theory for nonlinear viscoelastic behavior. Mechanics of Time-Dependent Materials 7 (2), 89–141.
Shih, C.F., Asaro, R.J., O'Dowd, N.P., 1991. Elastic–plastic analysis of cracks on bimaterial interfaces. 3. Large-scale yielding. Journal of Applied Mechanics 58 (2), 450–463.
Shirani, A., Liechti, K.M., 1998. A calibrated fracture process zone model for thin film blistering. International Journal of Fracture 93 (1–4), 281–314.
Sorensen, B.F., 2002. Cohesive law and notch sensitivity of adhesive joints. Acta Materialia 50 (5), 1053–1061.
Sorensen, B.F., Jacobsen, T.K., 2003. Determination of cohesive laws by the *J* integral approach. Engineering Fracture Mechanics 70 (14), 1841–1858.
Swadener, J.G., Liechti, K.M., 1998. Asymmetric shielding mechanisms in the mixed-mode fracture of a glass/epoxy interface. Journal of Applied Mechanics 65 (1), 25–29.
Takas, T.P., 2004. 100% solids aliphatic polyurea coatings for direct-metal applications. JCT Coatingstech 1 (5), 40–45.
Tvergaard, V., Hutchinson, J.W., 1993. The influence of plasticity on mixed-mode interface toughness. Journal of the Mechanics and Physics of Solids 41 (6), 1119–1135.
Tvergaard, V., Hutchinson, J.W., 1994. Toughness of an interface along a thin ductile layer joining elastic solids. Philosophical Magazine a-Physics of Condensed Matter Structure Defects and Mechanical Properties 70 (4), 641–656.
Varias, A.G., Suo, Z., Shih, C.F., 1991. Ductile failure of a constrained metal foil. Journal of the Mechanics and Physics of Solids 39 (7), 963–986.
Wang, S.S., 1983. Fracture-mechanics for delamination problems in composite-materials. Journal of Composite Materials 17 (3), 210–223.
Wei, Y., Hutchinson, J.W., 1998. Interface strength, work of adhesion and plasticity in the peel test. International Journal of Fracture 93 (1–4), 315–333.
Yang, Q.D., Thouless, M.D., 2001. Mixed-mode fracture analyses of plastically-deforming adhesive joints. International Journal of Fracture 110 (2), 175–187.
Yang, Q.D., Thouless, M.D., Ward, S.M., 2000. Analysis of the symmetrical 90 degrees-peel test with extensive plastic deformation. Journal of Adhesion 72 (2), 115.